A NUMERICAL STUDY OF JET-TO-JET IMPINGEMENT IN A MIXING HEAD

BY

RONALD W. YEO, M.A.Sc

A Thesis

Submitted to the School of Graduate Studies

in Partial Fulfilment of the Requirements

for the Degree

Doctor of Philosophy

McMaster University

JET-TO-JET IMPINGEMENT IN A MIXING HEAD

DOCTOR OF PHILOSOPHY(1993) McMasterUniversity
(Chemical Engineering) Hamilton, Ontario

TITLE: A Numerical Study of Jet-to-Jet Impingement in a Mixing Head

AUTHOR: Ronald W. Yeo
B.A.Sc. (University of Waterloo, Waterloo, Ontario)
M.A.Sc. (University of Waterloo, Waterloo, Ontario)

SUPERVISORS: Dr. P.E. Wood
Dr. A.N. Hrymak

NUMBER OF PAGES: xiii, 199

Abstract

A numerical method has been developed to model the jet-to-jet impingement in a mixing head. The governing equations are discretized in non-orthogonal curvilinear coordinates and higher-order upwinding methods are used for convection term discretization. Several problems with known solutions are used to test accuracy of the method. The results show that the method can predict the flow fields at moderate and high Reynolds numbers accurately.

The opposed jet flow field is used by the reaction injection moulding mixhead to mix pre-polymers. The steady state flow field exists at Reynolds numbers below 90 and unsteady state exists at Reynolds numbers above 90. The results of numerical simulations show that at the Reynolds number 50, the flow field is symmetrical and rotating ring vortices are formed around the impingement point. Symmetry breaks down as the Reynolds number is raised. Time integration showed that the flow field oscillates at Reynolds numbers above 100 and multiple frequencies exist at the Reynolds number of 125. The results are consistent with experimental results.

In the last chapter, the dynamical system theory is used to examine the opposed jet flow field. The stagnation point is a hyperbolic point of a dynamical system and can promote mixing. The elliptic points which exist at the core of vortices hinder mixing. The $(D:D)^{1/2}$ field was evaluated and confirmed the results of the dynamical system theory. The area surrounding the hyperbolic point had highest $(D:D)^{1/2}$ values indicating that the flow field can stretch more efficiently. A flow pattern which consists of multple hyperbolic points is proposed as an alternate design for the mixhead.

Acknowledgement

I wish to express my sincere gratitude to my supervisors Professor P.E. Wood and Professor A.N. Hrymak for providing valuable guidance and helpful criticisms, and the Department of Chemical Engineering for providing financial support. Also acknowledgements are due to A. Tyagi and D. Johnson for discussions related to the experimental aspects of this work.

Table of Contents

List of Figures

1. Introduction

This thesis presents a numerical study of the flow field created when two cylindrical laminar jets are impinged head-on near the closed end of a cylindrical mixing chamber. The steady state and oscillatory behaviour of the flow field are studied. The steady state exists at low Reynolds numbers. The oscillatory behaviour occurs above a critical Reynolds number.

Jet-to-jet impingement mixing in a confined chamber is used frequently in industry. The RIM(reaction injection moulding) process for making polymer parts uses jet-to-jet impingement mixing to mix two or more pre-polymers[Macosko(1989)]. In commercial RIM applications, mixing occurs in a cylindrical mixing chamber 10-15 mm in diameter, closed at one end by a piston that is driven forward after the operation to clean out the chamber. Two nozzles are positioned so that the jets of reactants leaving them impinge head-on. A similar flow field at higher Reynolds numbers is used by in a side-dump combustor to mix fuel and oxidant[Nossier and Behar(1986)].

To better understand an impingement mixer, it is necessary to understand the flow field created by the jet-to-jet impingement. Two different approaches can be used to study a flow field: experimental and numerical. The experimental approach uses a measuring device such as the LDA (Laser Doppler Anemometer) to obtain quantitative information about the flow field and flow visualization to obtain qualitative information. The numerical method uses a grid to represent the physical domain and computers to solve the discretized equations that are approximations of the continuum equations.

The numerical study of a flow field belongs to the recently emerging discipline called Computational Fluid Dynamics(CFD). The developments in computer hardware have made many important advancements in CFD possible. However, chemical engineers have been slow to adopt CFD techniques to solve problems in process engineering. Traditionally, approaches based on the simplified full transport equations are used to solve problems in chemical engineering. Only recently, CFD techniques that employ full transport equations have been applied to the problems in polymer processing[Vlachopoulos et al.(1984)], and CVD(Chemical Vapor Deposition) problems[Jensen(1991)]. In the design and optimization of reacting processes, a detailed model involving fluid flow and conservation of heat and chemical species are solved. A new term 'micro-reaction engineering', has been coined to describe the analysis based on the computational fluid dynamics technique[Jensen(1991)]

In the first section of this chapter, the fundamental concepts of computational fluid dynamics are introduced. The opposed jet impingement problem is discussed in the second section. In the subsequent chapters the numerical method is developed and steady and unsteady state solutions of opposed jet impingement are given. Some aspects of mixing in the opposed jet configuration are discussed in the last chapter using the velocity field obtained from previous chapters.

1.1 Computational Fluid Dynamics(CFD)

In computational fluid dynamics, the basic equations that govern the fluid flow are solved using computers. CFD does not belong to the category of rigorous theoretical analysis[Roache(1980)]. It is closer to experimental fluid dynamics in that the analyst solves the equations and waits to see what happens, just as the experimentalist observing

physical phenomena changes a set of conditions and waits to observe the effects of the change.

CFD has been used as a serious engineering tool since the 1970's. Early applications of CFD were in the aerospace and nuclear industries[Roach(1980)]. Limited memory and computational speed allowed only two dimensional problems to be solved. By the late 1970's, the falling cost and enhanced capabilities of computers allowed the solution of the Reynolds stress model of turbulence and some three dimensional problems. In the 1960's and 70's, the computing speed grew exponentially[Peyret and Taylor(1983)]. The recent trend is towards a rapid decrease in the cost of computing. Low cost work stations and numerical accelerator boards for PC's have made CFD available to a wide range of users.

The most obvious advantage of CFD compared to an experimental investigation is the turn-around time. Unlike experiments, which require time consuming design and set up, CFD techniques can be applied rapidly and the parameters in the model can be altered freely. Other benefits of CFD are mentioned in the paper by Chapman(1979). These are briefly summarized below;

1) The technique is non-intrusive.

2) CFD is more economical.

3) CFD provides more detailed and comprehensive information, and provides estimates of quantities that are difficult or impossible to measure, e.g., pressure.

4) CFD can simulate extreme conditions impossible using the experimental model.

However, CFD cannot replace physical experimentation. The approximate equations solved in the numerical analysis approach the continuum equations only in the

limiting case, i.e., when the mesh size becomes vanishingly small. In actual physical problems, it is impossible to have a vanishingly small mesh. Another limitation is that the constitutive relationships employed are only approximations[Roache(1982)]. Therefore, experimental data is essential in validating the assumptions used in the numerical model.

1.1.1 Governing Differential Equations

The governing equations express conservation principles for dependent variables. The dependent variables are usually specific properties. These quantities are expressed on a unit mass basis. For example, velocities are expressed as the momentum per unit mass. For a general dependent variable θ, the conservation principle can be stated as

Rate of accumulation of θ= rate of input of θ-rate of output of θ+source or sink of θ

In mathematical form the conservation principle becomes

$$\frac{\partial(\rho\theta)}{\partial t}+\nabla\cdot\vec{J}=S \qquad 1.01$$

where ρ is the density, t is the time, and S is the volumetric generation rate or the source term. $\vec{J}$ stands for the total flux vector(Fig 1.01). The total flux consists of 1) the convective flux due to the bulk motion of the fluid and 2) the diffusive flux caused by the gradient of θ Therefore,

$$\vec{J}=\rho\vec{u}\,\theta-\Gamma\,\nabla\,\theta \qquad 1.02$$

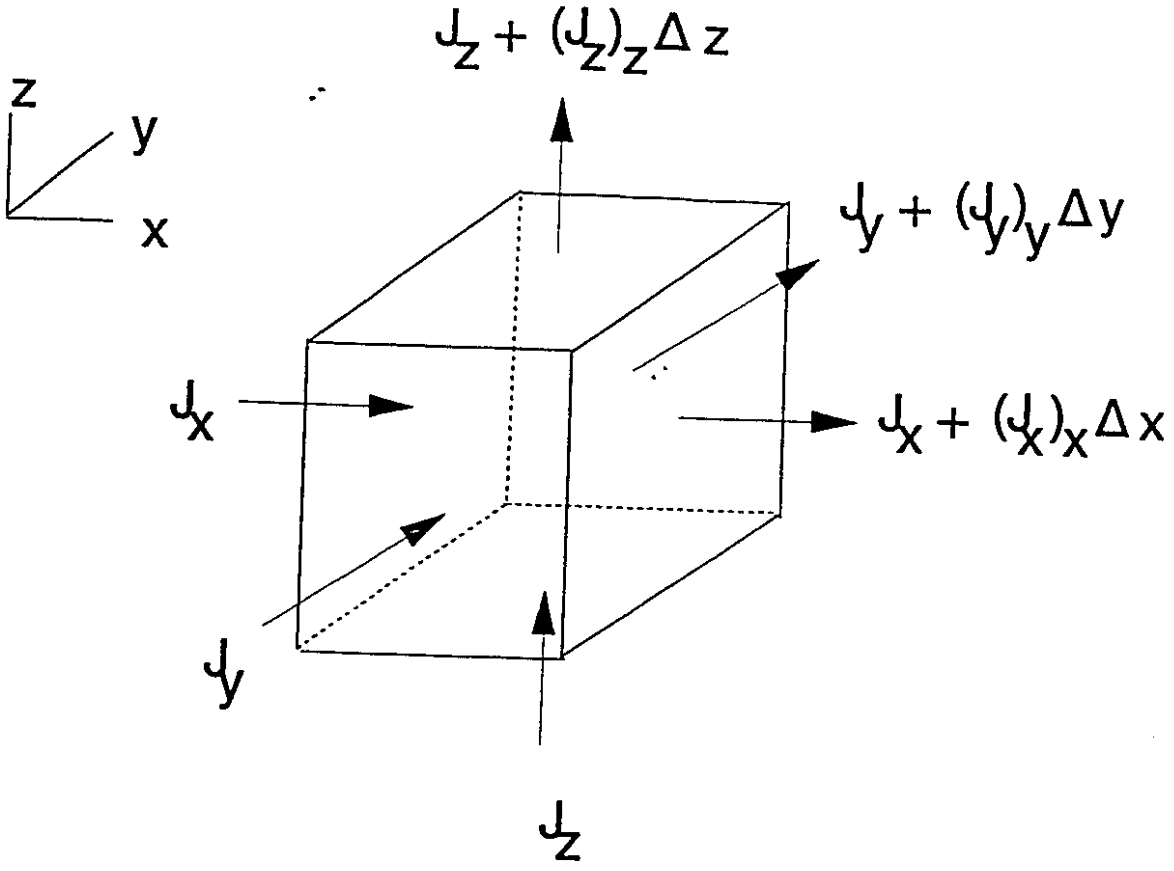

$$(J_i)_i = \frac{\partial J_i}{\partial i} \qquad i = (x, y, z)$$

Fig.1.01 : Conservation principle

where $\vec{u}$ is the velocity in the direction parallel to $\vec{J}$ and Γ is the diffusion coefficient. The transport equation for the generalized variable θ can be written as

$$\frac{\partial(\rho\theta)}{\partial t}+\nabla\cdot(\rho\vec{u}\theta)=\nabla\cdot(\Gamma\nabla\theta)+S \qquad 1.03$$

The mass conservation equation also can be derived from the generalized conservation principle. Since mass is conserved, the source term becomes zero. The mass flux depends upon the convection velocity only; therefore $\theta=1$ and the mass conservation equation can be written as (also known as the continuity equation)

$$\frac{\partial\rho}{\partial t}+\nabla\cdot(\rho\vec{u})=0 \qquad 1.04$$

The transport equations written in the above form are in "conservative" form. The non-conservative form can be obtained by applying the chain rule and with the addition of the continuity equation,(eq 1.04) becomes

$$\rho\frac{D\theta}{Dt}=\nabla\cdot(\Gamma\nabla\theta)+S \qquad 1.05$$

where

$$\frac{D}{Dt}=\frac{\partial}{\partial t}+u\cdot\nabla \qquad 1.06$$

is the material derivative.

The continuity equation also can be put in a non-conservative form

$$\frac{D\rho}{Dt} + \rho \nabla \cdot \vec{u} = 0 \qquad 1.07$$

For constant density flows the familiar $\nabla \cdot \vec{u} = 0$ results

1.1.2 Numerical Methods

The conservation principle given in the previous section can be applied to a physical system to arrive at a mathematical model of the process. Models are in the form of differential equations and auxiliary (boundary) conditions. The next step is the discretization of the governing model equations. In this step exact continuum equations are transformed to a set of approximate algebraic equations. There are four major methods used to discretize governing equations: 1) finite-difference, 2) finite-volume 3) finite-element and 4) spectral. Many factors govern the choice of a method to solve a problem. If the flow is convection dominated and Newtonian, the finite-difference or finite-volume methods may be appropriate[Roache(1980),Gosman et. al(1972), Patankar(1982)]. For creeping flows in which the convection terms can be ignored, the finite-element method may be better, especially if the flow occurs in complex geometries[Vlachopoulos et. al(1984)] or is non-Newtonian. If computational speed is important, the finite-volume or finite-difference method may be a better choice. In the study done by Ramanathan and Kumar(1988), the finite-element method is compared with the finite-volume method for heat conduction problems. The authors concluded that for an identical mesh system, the non-orthogonal, curvilinear, finite-volume method converges to a solution about 10 times faster than the finite-element method. The spectral method is used frequently for small scale flows which require a high degree of temporal and spatial accuracy. The spectral method was used to simulate a turbulent shear layer[Riley and Metcalf(1980)].

After obtaining the discretized model equations, the solution is obtained by applying a solution algorithm to solve the algebraic equations. The final step is the interpretation of the solution. Vector or contour plots may be used to represent the solution graphically. The steps involved in numerical modelling are illustrated schematically in Fig. 1.02. Since the jet-to-jet impingement is Newtonian and convection dominated, the finite volume or finite difference method is probably the best choice.

1.1.2.1 Finite Volume Method

The finite-volume method is closely related to the finite-difference method in that a pointwise approximation of a continuous function is used. However the basic method of discretization is different. In the finite volume method, the starting point is the conservative form of the governing equations. The governing equations are integrated over a fixed interval to construct the integral conservation statement and then the pointwise approximations are substituted for the continuous dependent variables. The method can be interpreted as a class of the weighted residual method[Patankar(1982)]. In the weighted residual method, the governing equations are multiplied by a weighting function W_i and then integrated over a prescribed interval. For the finite volume method the weighting function is 1 and the interval is the control volume. This method is also called the subdomain method[Patankar(1982)].

If the generalized transport equation is integrated over a region **R**, then we obtain

$$\int_R \frac{\partial \rho\theta}{\partial t}\, dR + \int_R \nabla\cdot(\rho\,\vec{u}\theta)\, dR = \int_R \nabla\cdot(\Gamma\nabla\theta)\, dR \qquad 1.08$$

Because t is independent of the space variable the integration can be transposed with the

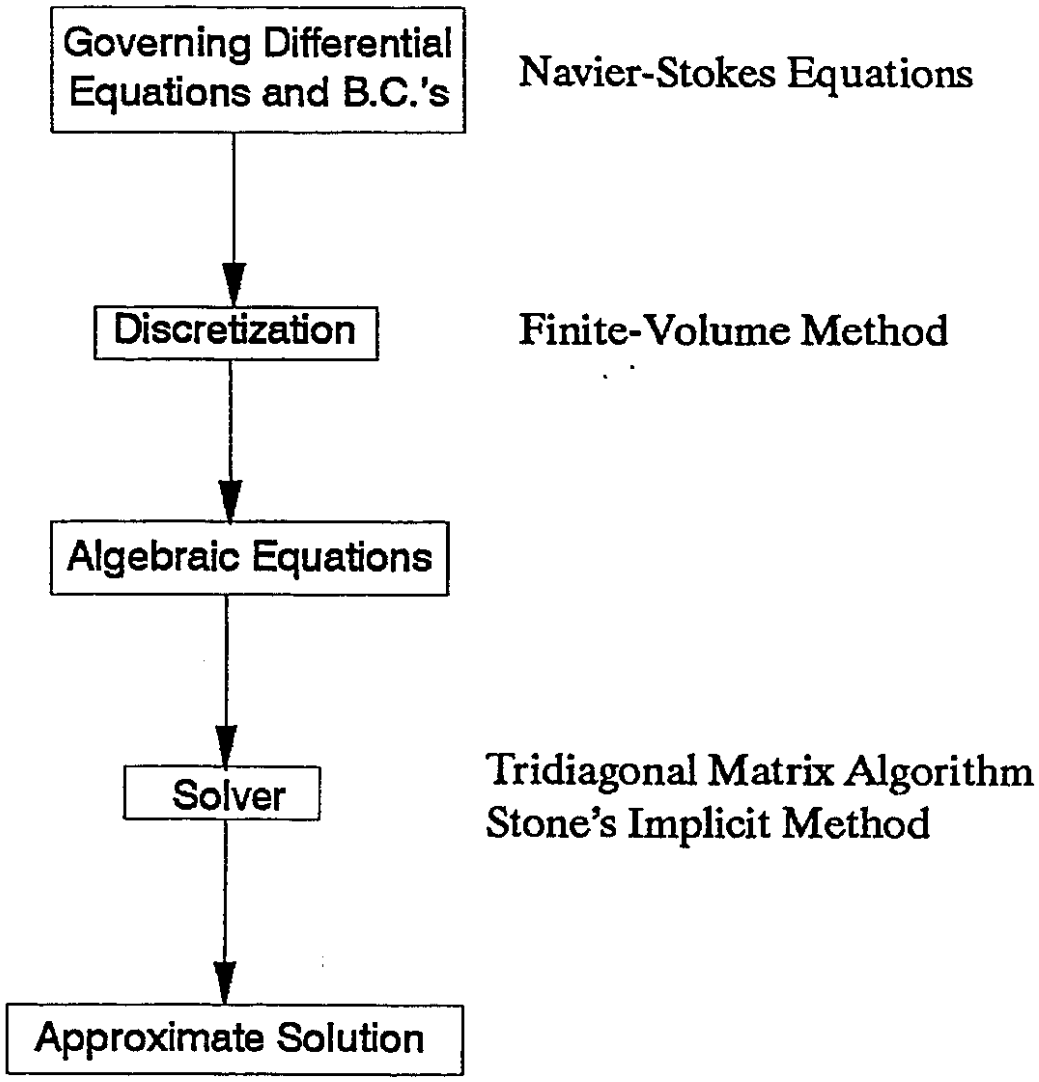

Fig.1.02: Numerical modelling procedure

the differentiation in the first term.

$$\int_R \frac{\partial \rho\theta}{\partial t} dR = \frac{\partial}{\partial t}\int_R \rho\theta dR \qquad 1.09$$

Using the Gauss divergence theorem we have

$$\int_R \nabla\cdot(\rho\vec{u}\theta)\, dR = \int_{\partial R} (\rho\vec{u}\theta)\cdot\vec{n} ds \qquad 1.10$$

and

$$\int_R \nabla\cdot(\Gamma\nabla\theta)\, dR = \int_{\partial R} (\Gamma\nabla\theta)\cdot\vec{n} ds \qquad 1.11$$

where ∂R is the boundary of R Then Eq.1.08 becomes

$$\frac{\partial}{\partial t}\int_R \rho\theta dR = -\int_{\partial R} (\rho\vec{u}\theta)\cdot\vec{n} ds + \int_{\partial R} (\Gamma\nabla\theta)\cdot\vec{n} ds \qquad 1.12$$

For a one dimensional, time dependent, convection diffusion equation the integral conservation statement can be reduced to

$$\int_w^e [\frac{\partial \rho\theta}{\partial t} + (\rho u\theta - (\Gamma\frac{\partial\theta}{\partial x}))]\, dx = 0 \qquad 1.13$$

The centre of the region R is denoted by the letter P and the right and left boundaries are denoted by letters e and w respectively(Fig.1.03). The distance between the intervals are assumed to be equal. Then integration of the above equation yields

$$\frac{\partial \rho\theta}{\partial t}\Delta x+[(\rho u\theta-\Gamma\frac{\partial\theta}{\partial x})_e-(\rho u\theta-\Gamma\frac{\partial\theta}{\partial x})_w=0 \qquad 1.14$$

The density and diffusion coefficient are assumed to be constant. For the convection term the values at the cell faces are assumed to be the average of the grid points. Therefore,

$$\theta_e=0.5\ (\theta_E+\theta_P) \qquad \theta_w=0.5\ (\theta_W+\theta_P) \qquad 1.15$$

For the first-order derivative a central differencing scheme is used

$$(\frac{\partial\theta}{\partial x})_e=\frac{\theta_E-\theta_P}{\Delta x} \qquad (\frac{\partial\theta}{\partial x})_w=\frac{\theta_P-\theta_W}{\Delta x} \qquad 1.16$$

Substituting the above approximations into Eq1.13 yields.

$$\rho\frac{(\theta_P-\theta_P^o)}{\Delta t}\Delta x+\rho u(\frac{\theta_E+\theta_P}{2})-\rho u(\frac{\theta_W+\theta_P}{2})$$

$$-\Gamma\frac{\theta_E-\theta_P}{\Delta x}+\Gamma\frac{\theta_P-\theta_W}{\Delta x}=0 \qquad 1.17$$

The above equation can be rearranged to obtain

$$A_P\theta_P=A_E\theta_E+A_W\theta_W+S \qquad 1.18$$

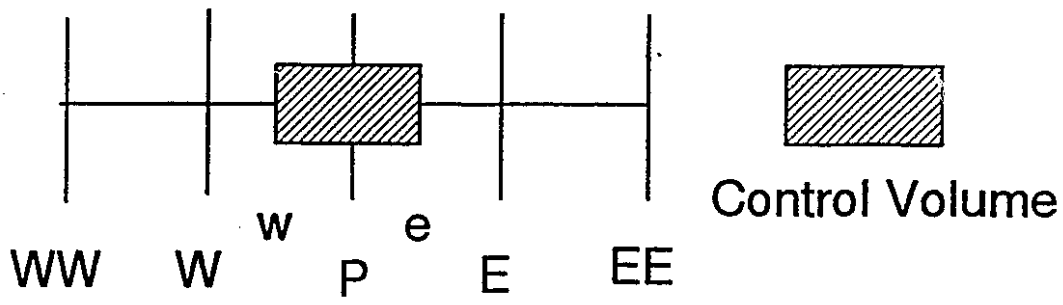

Fig.1.03: 1-D Control volume

where

$$A_E=\frac{\Gamma}{\Delta x^2}-\frac{\rho u}{2} \qquad 1.19$$

$$A_W=\frac{\Gamma}{\Delta x^2}+\frac{\rho u}{2} \qquad 1.20$$

$$A_P=\frac{2\Gamma}{\Delta x}+\frac{\rho u}{2}-\frac{\rho u}{2}+\frac{\rho}{\Delta t}=\frac{2\Gamma}{\Delta x}+\frac{\rho}{\Delta t} \qquad 1.21$$

and

$$S=\frac{\rho}{\Delta t}\theta_P^o \qquad 1.22$$

An identical result would be obtained if the finite difference method is used. For more complex equations, the finite volume method is more versatile. A grid with unequally spaced grid points and anisotropic diffusion coefficients can be handled more easily using the finite-volume method. Another advantage of the finite volume method is that it is based on the macroscopic physical laws, rather than continuum mathematics. Torrance (1968) has shown that the use of the conservative formulation, with only a first-order method is more accurate than the second-order, non-conservative formulation.

1.2 Jet-to-Jet Impingement

Jet-to-jet impingement of two liquids is used in the RIM process to mix the prepolymers. The important geometrical parameters for the RIM flow field are the cylinder and jet diameters and the position of the clean out piston during mixing. In Fig.1.04 a schematic of the RIM mixhead is shown. The mixing chamber diameter is

denoted by **D**, the jet diameter is **d**, and **H** is the distance between the jets centreline axis and the clean out piston head. In industrial practice, the Reynolds number based on the jet diameter and mean velocity,($Re_{jet}=\rho dV/\mu$) is between 100-600.

Previous studies of the RIM flow field used mainly flow visualization techniques. Tucker and Suh(1980), defined four distinct regions of flow based on the flow visualization techniques: (1) laminar flow, (2) small eddies, (3)large eddies and (4) turbulent mixing flow. They concluded that laminar flow occurred at Reynolds numbers below 50 and turbulent mixing flow occurred at Reynolds numbers above 150. A correlation for the striation thickness was derived based on the assumption of isotropic turbulence. Lee et. al(1980) used the slight density difference between the impinging jets to visualize the flow field. They observed formation of two large vortices at low Reynolds numbers and several vortices at higher Reynolds numbers. The study performed by Sandell(1983) presents a different result. Decolorizing dyes were used to visualize the flow field. The zone which was mixed became colourless, and the zone which was not mixed was seen as coloured. Through a video tape of the flow field, Sandell (1983) was able to observe and measure the periodic oscillations in the flow field. The dimensionless frequency of these oscillations increased monotonically at low jet Reynolds numbers and then reached a limit at higher Reynolds numbers before the jets themselves became turbulent. Apparently there was a threshold value of Re_{jet} for the onset of oscillation.

Planar laminar jet-to-jet impingement has been studied using a flow visualization technique[Denschikov et. al(1983)]. The flow developed auto-oscillations as a threshold Reynolds number was reached for a given jet separation distance. They found that the dimensionless frequency of the oscillations could be well correlated with the jet Reynolds

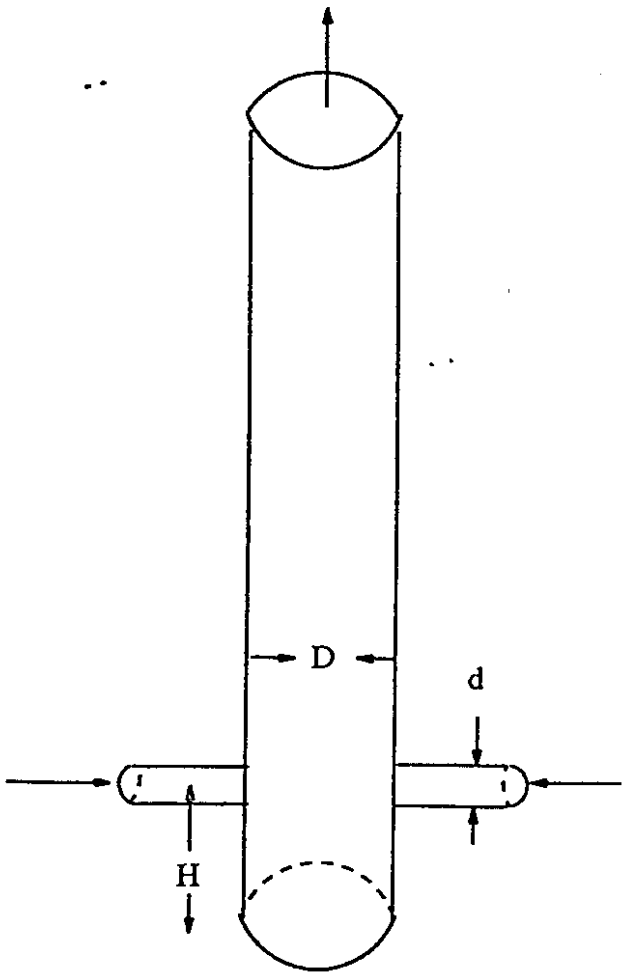

Fig. 1.04: RIM mixhead

number and the distance between the jets.

The previous studies show an unclear picture of the jet-to-jet impingement phenomenon. The work of Hama(1962) pointed out that when the velocity shows a sinusoidal oscillation, the streak lines may show a false impression of vortex role-up. The works of Ottino(1989) and Aref(1983) showed that oscillating laminar flows can induce chaotic particle paths. Therefore, flow visualization studies using dye streak lines and particle paths must be interpreted with care.

In this thesis a computational scheme is developed for solving three dimensional, unsteady laminar flows in irregular geometries. The flow field created by jet-to-jet impingement near the closed end of a cylinder will be the ultimate test of the model. In Chapter 2 the method is developed for two dimensional flows. The development follows that of Patankar(1981 , 1982) but several improvements are made to the algorithm for the convective terms. In Chapter 3 the method is generalized to 3-D non-orthogonal, curvilinear coordinates.

2.0 Two Dimensional Method

The aim of this chapter is to lay the necessary foundation for the next chapter in which a detailed discussion of the 3-D numerical method in complex geometries is presented. The discussion of the numerical method is given for simple 2-D, Navier-Stokes equations written in Cartesian coordinates. The discretization of the governing equations and the solution of the discretization equations are discussed in detail. The algorithms are simpler to illustrate in 2-D and the extension to 3-D is straight forward.

2.1 Governing Equations

For 2-D fluid flows in Cartesian coordinates, the governing equations for the motion of a fluid without body forces are

Continuity

$$\frac{\partial(\rho u)}{\partial x}+\frac{\partial(\rho v)}{\partial y}=0 \qquad 2.01$$

x-momentum

$$\frac{\partial \rho u}{\partial t}+\frac{\partial}{\partial x}\left(\rho uu-\mu\frac{\partial u}{\partial x}\right)+\frac{\partial}{\partial y}\left(\rho vv-\mu\frac{\partial u}{\partial y}\right)=-\frac{\partial p}{\partial x} \qquad 2.02$$

y-momentum

$$\frac{\partial \rho v}{\partial t} + \frac{\partial}{\partial x}\left(\rho vu - \mu \frac{\partial v}{\partial x}\right) + \frac{\partial}{\partial y}\left(\rho vv - \mu \frac{\partial v}{\partial y}\right) = -\frac{\partial p}{\partial y} \qquad 2.03$$

Eq. 2.01 is the statement of the conservation of mass. Eq. 2.02 and Eq. 2.03 express the conservation of momentum in the x and y directions respectively. Since many dependent variables obey the generalized conservation principle, it is more convenient to work with the generalized transport equation. Denoting dependent variables by θ, the transport equations can be generalized in the following form.

$$\frac{\partial \rho \theta}{\partial t} + \nabla \cdot (\rho \underline{u}\, \theta + \underline{J}) = S^{\theta} \qquad 2.04$$

$$\underline{J} = -\Gamma \nabla \theta \qquad 2.05$$

$\rho u \theta$ is the convective flux and J is the diffusive flux. S^{θ} denotes the source term. For the continuity equation $\theta=1$ and $S^{\theta}=0$ while for the momentum equations S^{θ} is the pressure gradient source term. Eq. 2.04 is the mathematical statement of the generalized conservation principle. The transport equations given in the above form are said to be in the conservative form. Integration of the conservative equations over a control volume yields the integral conservation statement.

The non-conservative form can be obtained by applying the chain rule and

substituting the continuity equation. For constant viscosity and density flows

continuity

$$\frac{\partial u}{\partial x}+\frac{\partial v}{\partial y}=0 \qquad 2.06$$

x-momentum

$$\frac{\partial(\rho u)}{\partial t}+\rho\left(u\frac{\partial u}{\partial x}+v\frac{\partial u}{\partial y}\right)=-\frac{\partial p}{\partial x}+\mu\left(\frac{\partial^2 u}{\partial x^2}+\frac{\partial^2 u}{\partial y^2}\right) \qquad 2.07$$

y-momentum

$$\frac{\partial(\rho v)}{\partial t}+\rho\left(u\frac{\partial v}{\partial x}+v\frac{\partial v}{\partial y}\right)=-\frac{\partial p}{\partial y}+\mu\left(\frac{\partial^2 v}{\partial x^2}+\frac{\partial^2 v}{\partial y^2}\right) \qquad 2.08$$

Equations 2.06-2.08 are the familiar Navier-Stokes equations in this limit.

2.2 Discretization

In the numerical method, the differential equations are solved approximately by transforming the differential equations into a set of algebraic equations. This process was illustrated briefly in Chap. 1. The finite-volume method is chosen, since the method is more flexible with discretization and the convection terms can be handled without

difficulty.

The finite-volume method is generally well tested and documented for a wide range of problems. The well known finite-volume code, TEACH(Teaching Elliptic Axisymmetric Characteristics Heuristically) code that was developed at Imperial College, London has been used for more than two decades to simulate high Reynolds number laminar and turbulent flows[Gosman et. al(1972), Patankar and Spalding(1972)]. The development given here follows the TEACH terminology closely.

The steps involved in the finite-volume discretization method can be summarized as follows.

1) Divide the solution domain into a number of control volumes which fill the whole domain.(Grid Generation)

2) Write integral conservation equations for each control volume.

3) Define discrete points, one per volume, and approximate all terms in the integral equations using the discrete point values.(Discretization)

The solution domain in Cartesian coordinates can be divided into a number of rectangular control volumes. The terminology used for the control volumes is given in Fig. 2.01. The capital letters indicate the control volumes centres and the small letters indicate the control volume faces separating the control volumes. The integral conservation statement can be constructed by integrating Eq. 2.04 over the control volume.

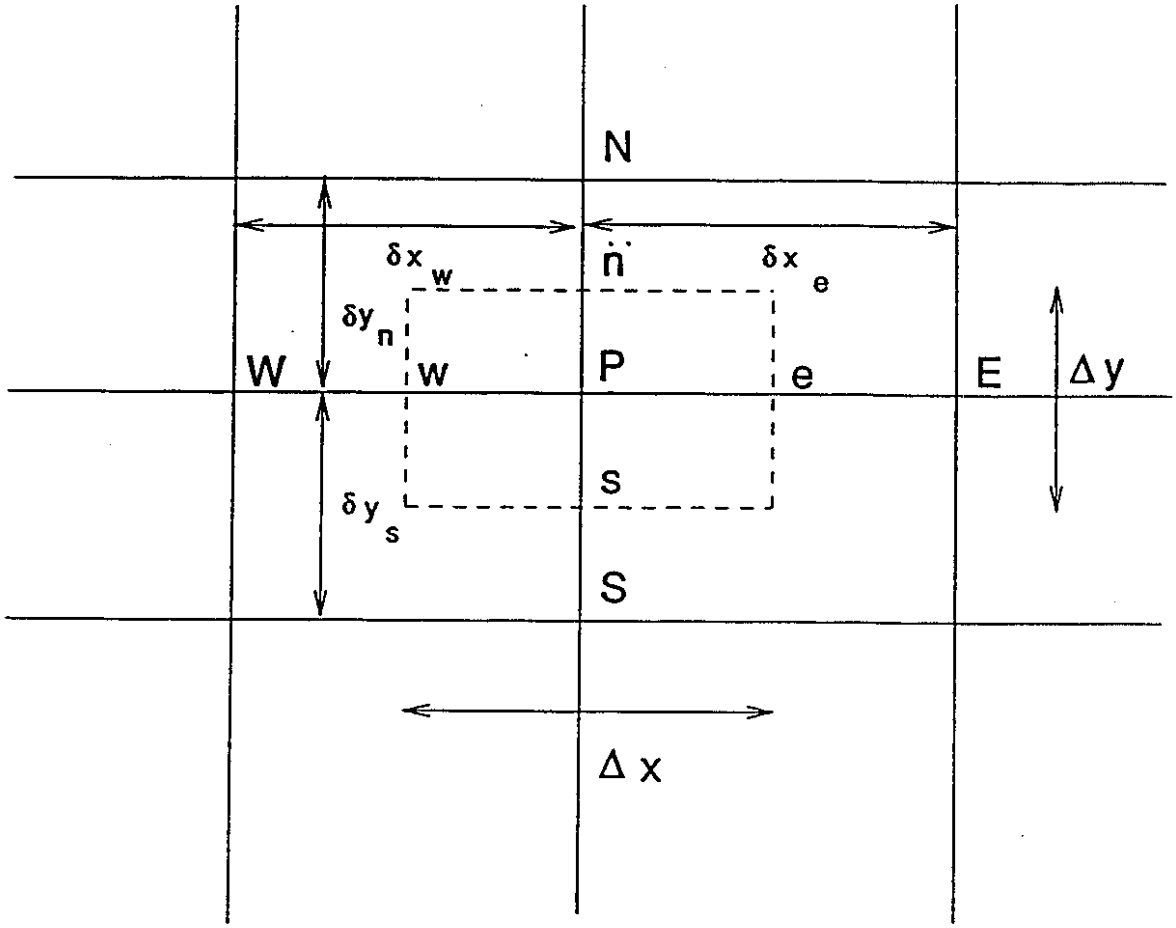

Fig.2.01:2-D Control volume

$$\int_{\Delta V} \frac{\partial(\rho\theta)}{\partial t} dV + \int_{\Delta V} \left[\frac{\partial}{\partial x} \left(\rho u\theta - \Gamma^{\theta} \frac{\partial \theta}{\partial x} \right) + \frac{\partial}{\partial y} \left(\rho v\theta - \Gamma^{\theta} \frac{\partial \theta}{\partial y} \right) \right] dV = \int_{\Delta V} S^{\theta} dV \quad 2.09$$

where

$$\Delta V = dxdy \cdot 1 \quad 2.10$$

The second term in Eq.2.09 is the volume integral of the divergence of the convective and diffusive fluxes. It is transformed into a surface integral by application of the Gauss theorem. If the surface integral is expressed as the sum of four surface integrals over the four control volume faces, the result is

$$\int_{\Delta V} \frac{\partial(\rho\theta)}{\rho t} dV + \int_{s}^{n} \left[\left(\rho u\theta - \Gamma^{\theta} \frac{\partial \theta}{\partial x} \right)_e - \left(\rho u\theta - \Gamma^{\theta} \frac{\partial \theta}{\partial x} \right)_w \right] dy$$

$$+ \int_{w}^{e} \left[\left(\rho v\theta - \Gamma^{\theta} \frac{\partial \theta}{\partial y} \right)_n - \left(\rho v\theta - \Gamma^{\theta} \frac{\partial \theta}{\partial y} \right)_s \right] dx = \int_{\Delta V} S^{\theta} dV \quad 2.11$$

Step 2 of the discretization procedure is now accomplished. The above equation states that the net accumulation rate of θ within a control volume is balanced by the net convective and diffusive fluxes across the control volume faces and the source terms within the control volume. The integral conservation statement is still an exact equation. The conservative finite-volume method requires discretization of the integral conservation

statement rather than the original differential equation.

The third step of the discretization process involves two key assumptions about the terms in the integral equation. The integral terms are approximated using the mean value theorem.

1) The fluxes through the control volume faces are expressed as the product of a mean flux, approximated by the value at the center of the control volume face and the cell face area.

2) The source terms and time derivatives are expressed as the product of a mean value, associated with the cell center, and the cell volume.

Using these assumptions the above equation is integrated to give:

$$\frac{\partial \rho\theta}{\partial t} + [(\rho u\theta - \Gamma^{\theta}\frac{\partial \theta}{\partial x})_e - (\rho u\theta - \Gamma^{\theta}\frac{\partial \theta}{\partial x})_w]\Delta y + [(\rho v\theta - \Gamma^{\theta}\frac{\partial \theta}{\partial y})_n - (\rho v\theta - \Gamma^{\theta}\frac{\partial \theta}{\partial y})_s]\Delta$$

$$= S^{\theta}\Delta V \qquad 2.12$$

For the continuity equation $\theta=1$ and $s^{\theta}=0$. Therefore

$$[(\rho u)_e - (\rho u)_w]\Delta y + [(\rho v)_n - (\rho v)_s]\Delta x = 0 \qquad 2.13$$

The transport equations are generally nonlinear and iteration processes are employed to obtain the solutions to them. In the iteration process, linearized equations are solved at each step. The momentum equations are linearized by assuming that the cell face velocities are known from their values at the previous iteration.

Now the discretization of the individual terms in Eq.2.12 is discussed in the order of appearance in the equation.

2.2.1 Time Integration

A first-order implicit method is used to integrate the time derivative. Therefore,

$$\frac{\partial \rho\theta}{\partial t}\Delta V = \frac{(\rho\theta) - (\rho\theta)^{\circ}}{\Delta t}\Delta V \qquad 2.14$$

$^{\circ}$ denotes values from the previous time step. All the space derivatives and source terms are evaluated at the present time level. This is equivalent to backward-differencing and lacks stability restrictions on the time-step size Δt.

2.2.2 Convection Terms

The convection term discretization requires approximation of the cell face values $\theta_e, \theta_w, \theta_n$ and θ_s. The simplest approach would be to assume a piecewise linear profile(Fig.2.02a) for θ. If the cell faces lie midway between grid points, then for the east and west faces

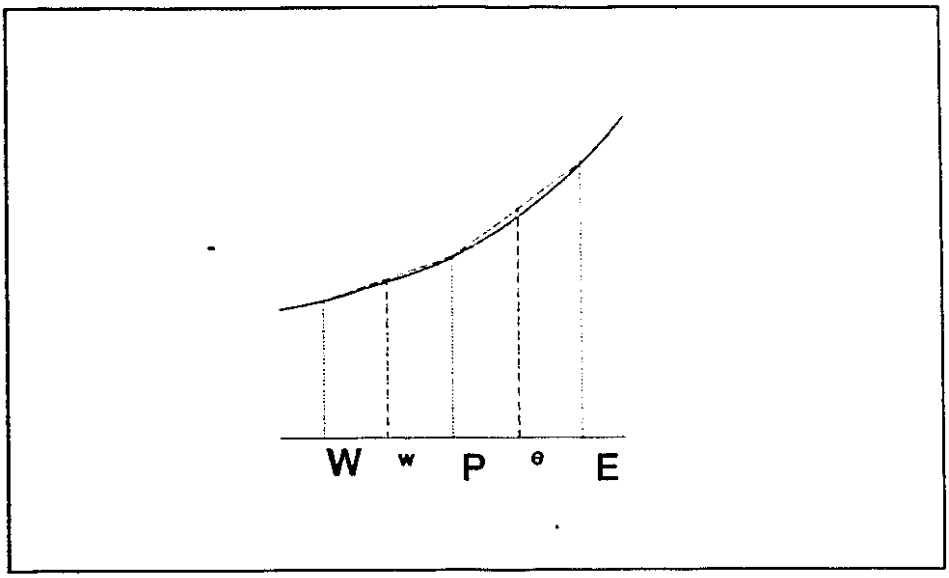

a)Central-differencing

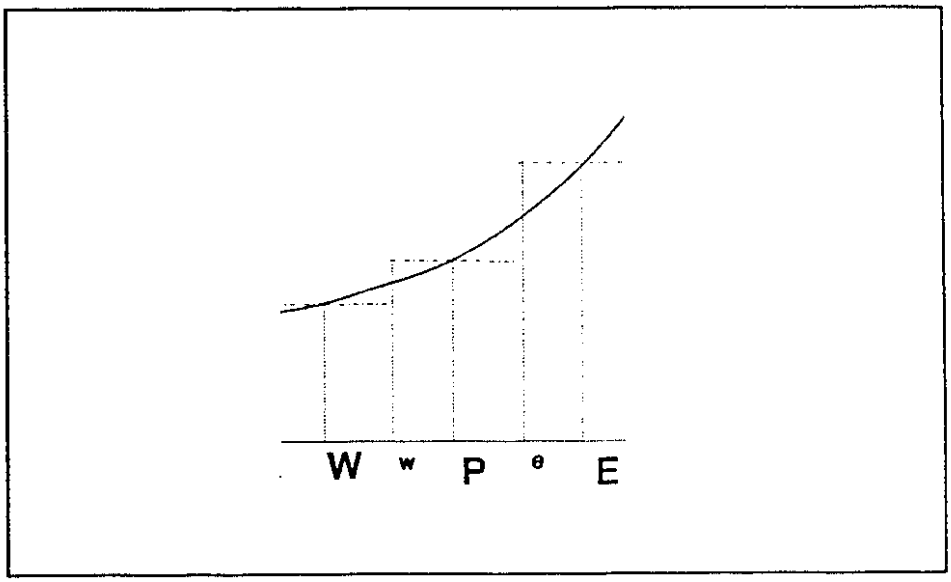

b)First-order upwinding

Fig.2.02:Convection term discretization

$$\theta_e=\frac{1}{2}(\theta_P+\theta_E) \qquad 2.15a$$

$$\theta_w=\frac{1}{2}(\theta_W+\theta_P) \qquad 2.15b$$

This method is equivalent to central differencing in the finite-difference method[Patankar(1981)]. Certain problems are encountered if this method is used with the convection dominated flows. The iteration scheme may diverge, and even when the iteration scheme converges the solution may contain physically unrealistic oscillations. This problem is discussed in detail in Patankar(1981).

The first-order upwinding method illustrated in Fig.2.02b is the simplest stable scheme for the convection terms. The idea behind this scheme is that as the fluid flows from one cell to the next, the value of θ at the upwind cell center is assumed to apply at the cell face. This assumes convection dominates diffusion in this direction. For the east and west faces

$$\theta_w=\begin{cases}\theta_W & u_w>0\\ \theta_P & u_w<0\end{cases} \qquad 2.16a$$

$$\theta_e=\begin{cases}\theta_P & u_e>0\\ \theta_E & u_e<0\end{cases} \qquad 2.16b$$

Therefore the discretization for the convection terms can be written as in compact notation as:

$$(\rho u)_w\theta_w=\max[\ (\rho u)_w, 0]\theta_W-\max[-(\rho u)_w, 0]\theta_P \qquad 2.17a$$

$$(\rho u)_e\theta_e=\max[\ (\rho u)_e, 0]\theta_P-\max[-(\rho u)_e, 0]\theta_E \qquad 2.17b$$

max[ ] denotes the maximum of the values enclosed by the brackets. Equations 2.17a, b, can be shown to be order ΔX($O(\Delta x)$) accurate. That is, when approximating the continuously varying function θ by the discrete function using a Taylor series about the cell face, the largest term neglected is $O(\Delta x)$ [Smith(1978)].

2.2.3 Diffusion Terms

The gradients in the diffusion terms are approximated using the central differencing scheme. For the east and west faces

$$\left(\frac{\partial\theta}{\partial x}\right)_w=\frac{\theta_P-\theta_W}{(\delta x)_w} \qquad 2.18a$$

$$\left(\frac{\partial\theta}{\partial x}\right)_e=\frac{\theta_E-\theta_P}{(\delta x)_e} \qquad 2.18b$$

This discretization is $O(\Delta x^2)$ accurate.

2.2.4 Source Terms

A single source term can be linearized and divided into two parts. One part is

included with the source and the other part which is linear in θ_p has its coefficient summed up with A_p. Therefore,

$$S^{\theta}=S_U+S_P\theta_P \qquad 2.19$$

For stability S_p must be positive[Patankar(1982)].

2.2.5 The Discretization Equation

Substituting the discretization schemes for the individual terms into Eq.2.12 yields

$$A_P\theta_P=\sum_{nb} A_{nb}\theta_{nb}+S_U+\frac{(\rho\theta)^{\bullet}}{\Delta t}\Delta V \qquad 2.20$$

where

$$\sum_{nb} A_{nb}\theta_{nb}=A_E\theta_E+A_W\theta_w+A_N\theta_N+A_S\theta_S \qquad 2.21$$

$$A_P=A_E+A_W+A_N+A_S-S_P+\frac{\rho\theta_P}{\Delta t}\Delta x\Delta y \qquad 2.22$$

and

$$A_E=\Gamma^{\theta}_e\frac{\Delta y}{(\delta x)_e}+\max[0,\ -\rho u_e\Delta y] \qquad 2.23a$$

$$A_W=\Gamma_w^\theta\frac{\Delta y}{(\delta x)_w}+\max[0,\ \rho u_w\Delta y] \qquad 2.23b$$

$$A_N=\Gamma_n^\theta\frac{\Delta x}{(\delta y)_n}+\max[0,\ -\rho v_n\Delta x] \qquad 2.23c$$

$$A_S=\Gamma_s^\theta\frac{\Delta x}{(\delta y)_s}+\max[0,\ \rho v_s\Delta x] \qquad 2.23d$$

2.2.6 Under-relaxation

The linearization of the nonlinear terms is usually not sufficient to obtain convergence in the iteration process. The corrections implied by the method are usually too great and will lead to a divergent solution. The equations need to be under-relaxed, using the under-relaxation factor α. In under-relaxation, new estimates of θ are obtained from previous estimates plus a small part of the computed corrections.

$$\theta^{new}=\alpha\theta+(1-\alpha)\theta^{old} \qquad 2.24$$
$$0<\alpha\leq 1$$

Incorporating under-relaxation, the discretization equation(Eq.2.20) can be rewritten as

$$B_P\theta_P=\sum_{nb}A_{nb}\theta_{nb}+b \qquad 2.25$$

where

$$B_P=(\frac{1}{\alpha})\ A_P \qquad 2.26$$

$$b=\frac{(\rho\ \theta^*)\ \Delta V}{\Delta t}+S_U+\frac{(1-\alpha)}{\alpha}\ \theta^{old}A_P \qquad 2.27$$

2.3 Staggered Grid Method

The discussions to this point have been centered on the discretization of the generalized conservation equation. The method can be applied to the solution of momentum equations which are a particular form of the transport equations. However, a unique problem arises because of the nature of the pressure gradient in the source terms. An explicit equation for the pressure does not exist; therefore, the pressure field is specified indirectly through the continuity equation. When a correct pressure field is obtained, the velocity field satisfies the continuity constraint.

The dependent variables of the transport equations are usually positioned at the center of the control volume. This approach may present problems for the Navier-Stokes equations. If the velocities and pressure are positioned at the control volume center and the convection terms are evaluated using the linear interpolation of the cell grid velocities, only the alternating grid points are coupled[Patankar(1982)]. This leads to unrealistic oscillations in the velocity and pressure field. Several approaches to remedy the problems associated with the oscillatory pressure field are possible. The most widely accepted approach uses a staggered grid and a semi-implicit method to solve for the pressure. A

more recent approach developed by Rhie(1981), uses the traditional cell centered (non-staggered or co-located) arrangement of the variables with a special interpolation scheme for the cell face velocities to prevent an oscillatory pressure field.

In the staggered grid scheme, the velocities are stored at the cell faces as shown in Fig. 2.03. The u-velocity component is located at the center of the west face of the pressure control volume. For u-velocity, the P- grid point for pressure becomes east face center of the control volume and the W- grid point becomes the west face center of the control volume. Therefore, control volumes for the velocities are different from the control volumes for the continuity equation. The cell face velocities(u_w ,v_s) for the continuity control volumes are the cell center velocities(u_P,v_P) for the velocity control volumes. The staggered arrangement ensures a strong coupling between velocities and pressure. The velocities are driven by the adjacent grid pressures. Note that three separate grids are required, one for each equation.

The discretization equations for the staggered grid are

x-momentum

$$B_w^u u_w = \sum_{nb} A_{nb}^u u_{nb} + b^u + (P_W - P_P)\,\Delta y \qquad 2.28$$

y-momentum

$$B_s^v v_s = \sum_{nb} A_{nb}^v v_{nb} + b^v + (P_S - P_P)\,\Delta x \qquad 2.29$$

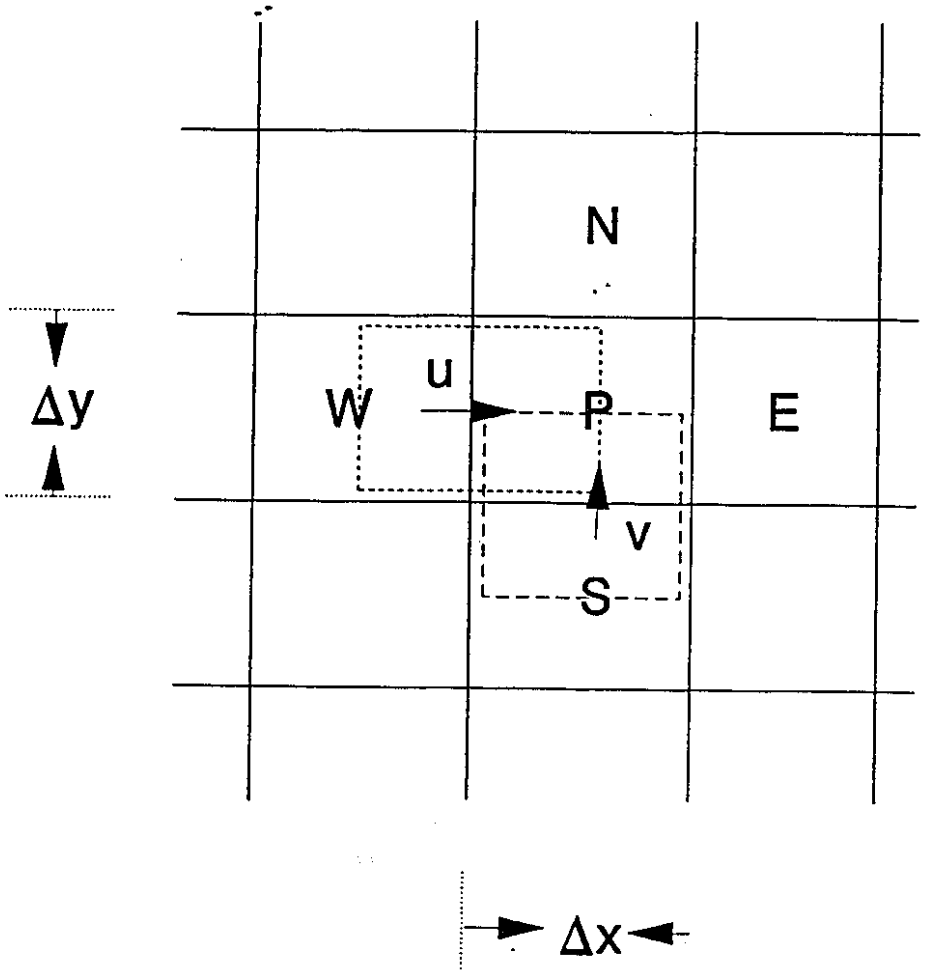

Fig.2.03 : Staggered grid

continuity

$$\rho (u_e - u_w) \Delta y + \rho (v_n - v_s) \Delta x = 0 \qquad 2.30$$

The equations are written with respect to the continuity control volumes.

The solution procedure for the above equations uses a semi-implicit procedure to obtain the solutions. Since the pressure field is indirectly determined by the continuity equation, the momentum equations and the continuity equation can be combined to form the pressure correction equations. This idea was used successfully in the SIMPLE algorithm of Patankar and Spalding(1972). Later several improvements were proposed. SIMPLE and one of the modifications, SIMPLEC [(Van Doormal and Raithby(1987)] are described below.

2.3.1 SIMPLE

SIMPLE is a member of a class of methods classified as segregated methods. In a segregated method the pressure and velocity fields are uncoupled. One first estimates a pressure field and then finds the velocity field that satisfies it. The computed velocity field generally will not satisfy continuity so a new pressure field is estimated. The process is continued until continuity is satisfied.

The solution to the momentum equations initially is obtained using an estimated pressure field p^*.

$$B_w^u u_w^* = \sum_{nb} A_{nb}^u u_{nb}^* + (p_W^* - p_P^*)\,\Delta y + b^u \qquad 2.31$$

$$B_s^v v_s^* = \sum_{nb} A_{nb}^v v_{nb}^* + (p_S^* - p_N^*)\,\Delta x + b^v \qquad 2.32$$

Since p^*, is only an estimate, solutions obtained by solving the momentum equations(Eq.2.31 and Eq.2.32) do not satisfy the continuity constraint. Let p, u and v be the improved estimates of pressure and velocity respectively. Let p', u' and v' be the corresponding corrections such that

$$p = p^* + p' \qquad u = u^* + u' \qquad v = v^* + v' \qquad 2.33a,b,c$$

In terms of the improved estimates the momentum equations(Eg.2.31 and 2.32) can be written as

$$B_w^u (u^* + u')_w = \sum_{nb} A_{nb}^u (u^* + u')_{nb} + \left((p_W^* + p_W') - (p_P^* + p_P') \right) \Delta y + b^u \qquad 2.34$$

$$B_s^v (v^* + v')_s = \sum_{nb} A_{nb}^v (v^* + v')_{nb} + \left((p_S^* + p_S') - (p_N^* + p_N') \right) \Delta x + b^v \qquad 2.35$$

Equations 2.34 and 2.35 are subtracted from Equations 2.31 and 2.32 to obtain

$$B_w^u\ u_w' = \sum_{nb} A_{nb}^u\ u_{nb}' + (p_W' - p_P')\,\Delta y \qquad 2.36$$

$$B_s^v\ v_s' = \sum_{nb} A_{nb}^v v_{nb}' + (p_S' - p_P')\,\Delta x \qquad 2.37$$

Since u' and v' are the velocity corrections which are small in magnitude, it seems reasonable to approximate that

$$\sum_{nb} A_{nb}^{u} u'_{nb}=0 \qquad \sum_{nb} A_{nb}^{v} v'_{nb}=0 \qquad 2.38a,b$$

Therefore combining Equations 2.38a,b with Equations 2.36 and 2.37 gives

$$u_w=u_w^*+d_w(p'_W-p'_P) \qquad 2.39$$

$$v_s=v_s^*+d_s(p'_S-p'_P) \qquad 2.40$$

where

$$d_w=\frac{\Delta y}{B_w^u} \qquad d_s=\frac{\Delta x}{B_s^v} \qquad 2.41a,b$$

The pressure correction equation can be derived by substituting the equations(Equations 2.38a and 2.38b) into the continuity equation(Eq.2.30).

$$A_P^P p'_P=A_E^P\ p'_E+A_W^P\ p'_W+A_N^P\ p'_N+A_S^P\ p'_S+b^P \qquad 2.42$$

Where

$$A_P^P=A_S^P+A_W^P+A_N^P+A_S^P \qquad 2.43$$

$$A_E^P=\rho d_e \Delta y \qquad 2.44a$$

$$A_W^P=\rho d_w \Delta y \qquad 2.44b$$

$$A_N^P=\rho d_n \Delta x \qquad 2.44c$$

$$A_S^P=\rho d_s \Delta x \qquad 2.44d$$

and

$$b^P=\rho\,(u_e^*-u_w^*)\,\Delta y+\rho\,(v_n^*-v_s^*)\,\Delta x \qquad 2.45$$

where b^p is the residual mass source. As the iteration steps proceed to satisfy continuity, this b^p becomes smaller.

The steps in the solution algorithm can be described as follows;

For a given time step.

1) Assemble the coefficients of the momentum equations using the estimated values of the field variables.

2) Solve for the velocities u^*,and v^* using the estimated pressure p^*(Eq.2.31 and Eq.2.32).

3) Assemble the coefficients for the pressure correction equation.

4) Solve for the pressure correction p' using the intermediate velocities u^* and v^* to evaluate the mass source term(Eq's 2.42 to 2.45).

5) Obtain the corrected pressure, p and velocities u and v.

6) Check for convergence either by evaluating the residuals or the maximum change for each variable.

7) If convergence is not reached use the new values p, u, and v as p^* , u^*, and v^* and go back to step 2

One of the drawbacks of the SIMPLE method is that the rate of convergence is rather slow. The approximations in Eq.2.38(a) and (b) are not the optimal ones and the pressure correction must be under-relaxed to obtain convergence.

$$p=p^{*}+\alpha p' \qquad 2.46$$

2.3.2 SIMPLEC

A more consistent pressure correction scheme can be obtained by subtracting the underlined terms from both sides of the correction equations(Eq's 2.36 and 2.37) as shown below.

$$B_w^u u_w' - \underline{\sum_{nb} A_{nb}^u u_w'} = \sum_{nb} A_{nb}^u u_{nb}' - \underline{\sum_{nb} A_{nb}^u u_w'} + (p_W'-p_P')\,\Delta y \qquad 2.47$$

$$B_s^v v_s' - \underline{\sum_{nb} A_{nb}^v v_s'} = \sum_{nb} A_{nb}^v v_{nb}' - \underline{\sum_{nb} A_{nb}^v v_{nb}'} + (p_S'-p_P')\,\Delta x \qquad 2.48$$

In SIMPLEC the following approximations are made[Van Doormaal and Raithby(1987)].

$$\sum_{nb} A_{nb}^u (u_{nb}'-u_w') = 0 \qquad \sum_{nb} A_{nb}^v (v_{nb}'-v_s') = 0 \qquad 2.49a,b$$

The coefficients for the pressure correction equation are given below for the SIMPLEC scheme

$$d_w = \frac{\Delta y}{B_w^u - \sum_{nb} A_{nb}^u} \qquad 2.50$$

$$d_s = \frac{\Delta x}{B_s^v - \sum_{nb} A_{nb}^v} \qquad 2.51$$

The steps in the SIMPLEC algorithm are identical to SIMPLE except the pressure correction is not under-relaxed.

2.4 Non-staggered Grid Method

The benefits of using the non-staggered scheme, in which the velocity and pressure occupy the same location, are many. Only one set of control volumes is required; therefore, the method requires less memory and the code would be simpler than the staggered grid method. In this section the non-staggered method for two dimensions is explained. In the next chapter the method is extended to three dimensions and complex geometries.

The first successful attempt to use the non-staggered grid for fluid flow problems was achieved by Rhie(1981). The method was developed for two-dimensional fluid flow in a complex geometry. Many details on the implementation of the method are omitted from his thesis. The missing details were filled by later researchers. The work by Peric et. al(1988) provides more details on the determination of the cell face velocities. Majumdar(1988) examines the effect of under-relaxation of the cell face velocities on the

accuracy of the solution.

The discretized momentum equations for the cell center velocities during the iteration process can be written as:

$$u_P^* = \frac{\sum_{nb} A_{nb}^u u_{nb}}{B_P^u} + (p_w^* - p_e^*)\,\frac{\Delta y}{B_P^u} + (1-\alpha)\,u_P^{old} \qquad 2.52$$

$$v_P^* = \frac{\sum_{nb} A_{nb}^v v_{nb}}{B_P^v} + (p_s^* - p_n^*)\,\frac{\Delta x}{B_P^v} + (1-\alpha)\,v_P^{old} \qquad 2.53$$

The velocities are located at the cell centers and the cell face pressure differences become the source terms for the momentum equations(Fig.2.04).

There are three parts to the discretized velocities(Eq.2.52 and 2.53). The first part comes from the coefficients . The second part comes from the pressure source term, and the remaining part comes from under-relaxation. To evaluate the coefficients, we require the velocities at the cell faces.

If all three parts are linearly interpolated between grid points, the solution obtained will contain unrealistic oscillations since the velocities and pressures at alternating grids are coupled. Rhie's scheme requires linear interpolation of coefficients, but the pressure source is evaluated using the adjacent cell grid pressures. Majumdar concludes that the linear interpolation of the under-relaxed part leads to the dependence of the solution on the relaxation parameter. To avoid the linear interpolation of grid point velocities, the cell face velocities are stored separately.

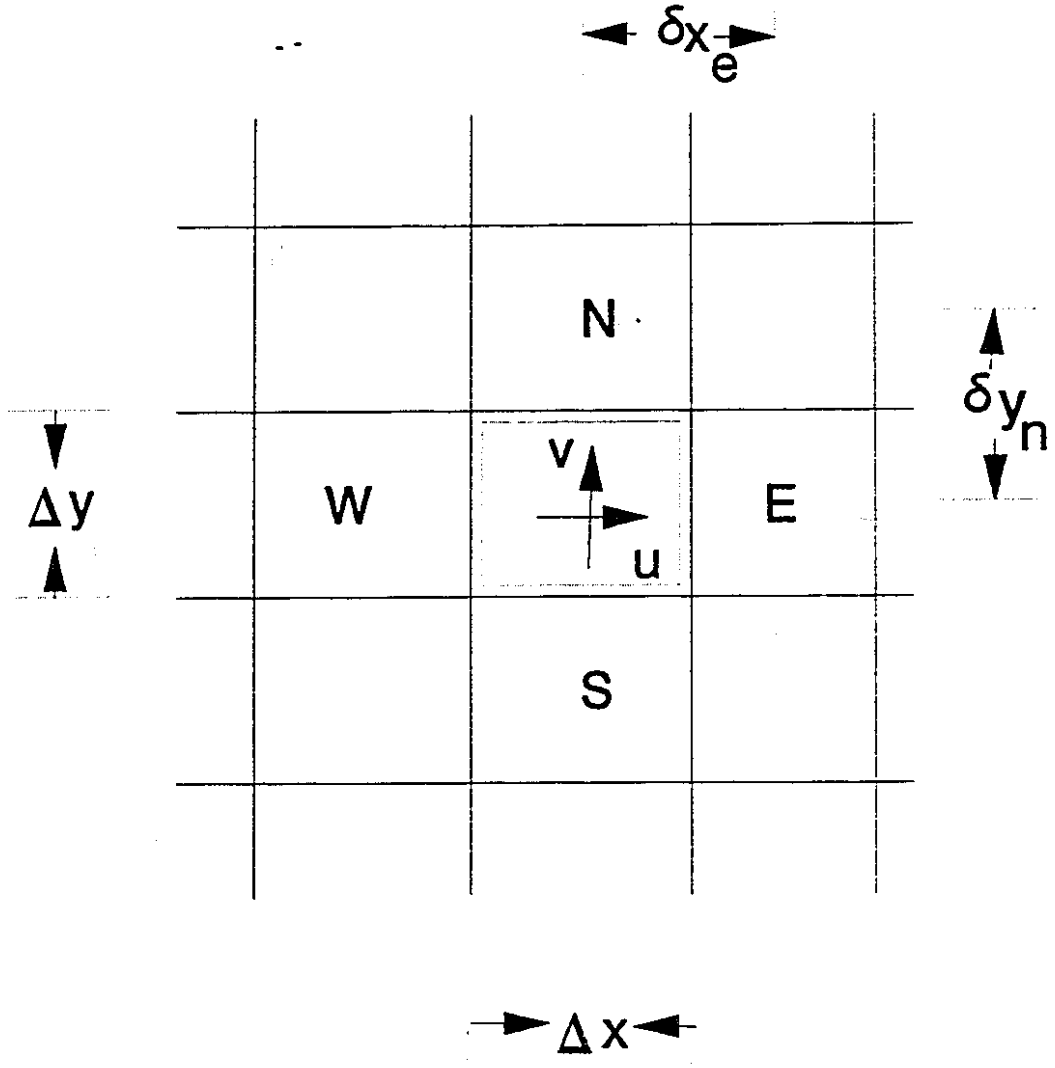

Fig.2.04: Non-staggered grid

A new notation is introduced where the terms enclosed within a bracket with an overbar denote a linear interpolation. For example

$$\overline{(B^u)}_w = f\ B_P^u + (1-f)\ B_W^u \qquad 2.54$$

where f is the weighting factor or the linear interpolation. When the cell face is equidistant from the adjacent grids, $f=0.5$.

The evaluation of the cell face velocities is illustrated at the west face.

$$u_w^* = \overline{\left(\frac{\sum_{nb} A_{nb}U_{nb}}{B^u}\right)}_w + \overline{\left(\frac{\Delta y}{B^u}\right)}_w (p_W^* - p_P^*) + (1-\alpha)\, u_w^{old} \qquad 2.55$$

Where

$$\overline{\left(\frac{\sum_{nb} A_{nb}U_{nb}}{B^u}\right)}_w = f\ \left(\sum_{nb} \frac{A_{nb}U_{nb}}{B^u}\right)_P + (1-f)\ \left(\sum_{nb} \frac{A_{nb}U_{nb}}{B^u}\right)_W \qquad 2.56$$

and

$$\overline{\left(\frac{\Delta y}{B^u}\right)}_w = \frac{fB_W + (1-f)B_P}{B_P B_W}\Delta y \qquad 2.57$$

The important feature of the above equation is that the cell face velocity is directly linked to the neighbouring cell grid pressures. The cell face velocities determined using the above formula are used to evaluate the coefficients in the discretization equations. In the pressure correction step, for the mass source term in Eq. 2.45 the velocities at the

faces are also evaluated using the above method.

The pressure correction equation is derived again using the continuity equation and the approximate form of the momentum equations. Since the corrections at the cell faces are required, the coefficients at the cell center values are interpolated. At the cell centers P and W the corrections for the velocity can be written as

$$u_P = u_P^* + d_P(p'_W - p'_e) \qquad 2.58$$

$$u_W = u_W^* + d_W(p'_{WW} - p'_W) \qquad 2.59$$

The cell face velocity correction is

$$u_w = u_w^* + \overline{d_w}(p'_W - p'_P) \qquad 2.60$$

and

$$\overline{d_w} = f\ d_W + (1-f)\ d_P$$

2.4.1 SIMPLE

For SIMPLE the cell center corrections for the velocities are obtained by making the identical assumption as the staggered grid case(Eq2.38a,b). Therefore,

The cell face correction coefficient is

$$d_W = \frac{\Delta y}{B_W^u} \qquad d_P = \frac{\Delta y}{B_P^u} \tag{2.61}$$

$$\overline{(d)}_w = \overline{\left(\frac{\Delta y}{B^u}\right)}_w \tag{2.62}$$

This is identical to Eq.2.57.

The solution algorithm can be described as follows

1)Estimate all the field variables and assemble the coefficients for the velocity equations.

2)Solve the momentum equations for the cell center velocities, u_P^* and v_P^*(Eq's 2.52 and 2.53).

3)Interpolate using Eq.2.55 to obtain the cell face velocities, u_w^*, v_s^*.

4)Assemble the coefficients for the pressure correction equation. Use the result from Step(3) to calculate the mass source.

5)Correct the cell center pressure and cell face and center velocities.

6)Check for convergence.

7)If convergence is not obtained take the corrected pressure and velocities(p,u,v) as the new estimates(p^*,u^* and v^*) and go back to Step(2)

2.4.2 SIMPLEC

SIMPLEC for the non-staggered grid is derived in the same manner as SIMPLE. To determine the cell center velocities, the difference of velocity corrections rather than the velocity corrections themselves are assumed to be zero. For the west face

$$\overline{d_w} = \overline{\left(\frac{\Delta y}{B^u - \sum_{nb} A_{nb}}\right)_w} \qquad 2.63$$

The steps in the algorithm are identical to the SIMPLE algorithm.

2.5 Boundary Conditions

The Navier-Stokes equations presented in Section 2.1 are partial differential equations with parabolic behaviour in time and elliptic behaviour in space. Boundary conditions are required along cell boundaries of the solution domain. The boundary conditions can be classified into three different types.

1) Dirichlet - values of the variables are given along boundaries.

2) von Neuman - gradient of the variables normal to the boundaries are prescribed.

3) Robin - combination of type 1 and 2.

Type 3 seldom occurs with the Navier-Stokes equations. Solid walls and inlet planes where the velocity is known belong to the first type. Outlet boundaries belong to the second type. The Dirichlet boundary conditions can be implemented by simply plugging the known value at the boundaries. The discretized equations at the boundaries contain one less unknown. The most frequently occuring von Neuman type boundary condition is the zero gradient condition. If the zero gradient condition occurs at the east boundary, the condition can be implemented simply by setting the east coefficient to zero, $A_E = 0.0$.

2.5.1 Wall Boundaries

The no-slip condition is used on walls. Velocities in all directions are set to zero

$$u=v=0.0 \tag{2.64}$$

2.5.2 Symmetry Plane

On symmetry planes, the normal gradient of the tangential velocity and normal velocity are set to zero. If the symmetry plane is the south boundary, the following boundary conditions are applied.

$$\frac{\partial u}{\partial y}=0.0 \quad v=0.0 \tag{2.65}$$

2.5.3 Inlet Plane

Usually profiles of u and v taken either from data or from prescribed analytical formulae.

2.5.4 Outlet Plane

If the exit plane is sufficiently far way from recirculation regions, fully developed flow can be assumed, i.e., gradients in the streamwise direction can be neglected. If the outlet plane is located at the east boundary.

$$\frac{\partial u}{\partial x}=\frac{\partial v}{\partial x}=0.0 \qquad 2.66$$

2.5.5 Boundary Conditions for the Pressure Correction Equation

Two kinds of boundary conditions are possible.

1) boundary pressure is given.

2) normal velocities at the boundaries are known.

Pressure boundary condition of type 1 is not considered since this type arises less frequently. For type 2, since the normal velocity is known it does not need to be corrected. For examples if the boundary is in the south direction $v'_s=0$ and the pressure correction equation becomes

$$\rho_e u_e \Delta y-\rho_w u_w \Delta y+\rho_n v_n \Delta x=S \qquad 2.67$$

or $a_s^P=0$. This is equivalent to setting zero gradient(von-Neuman) type boundary conditions.

2.6 Solution of the Discretization Equations

For each control volume a set of algebraic equations is formulated. There are as many equations as there are unknowns. One of the methods for solving the linear equation set is Gaussian elimination. However, such solution techniques are computationally inefficient and require large storage[Patankar(1981)]. Iterative techniques, which take

advantage of the sparse structure of the matrix, require less storage and are computationally more efficient. The solution technique employed in this work is a combination of the line-by-line method and a block correction scheme.

2.6.1 Line-by-line Method

If, in the discretized equation(Eq.2.25), the y-direction neighbours θ_N and θ_S are considered to be tentatively known, then the equation would have only three unknowns, θ_P,θ_E and θ_W. In x-direction, the discretization equation can be written as

$$a_i\theta_i=b_i\theta_{i+1}+c_i\theta_{i-1}+d_i \qquad i=2,I-1 \tag{2.68}$$

where θ_i,θ_{i+1} and θ_{i-1} stand for θ_P,θ_E and θ_W respectively. The coefficients are related to those in Eq.2.25 by

$$a_i=B_P \tag{2.69a}$$

$$b_i=A_E \tag{2.69b}$$

$$c_i=A_N \tag{2.69c}$$

$$d_i=A_N\theta_N+A_S\theta_S+b \tag{2.69d}$$

The resulting tridiagonal equation set can be solved by the TDMA(Tridiagonal Matrix Algorithm)[Patankar(1981)].

New coefficients P_i and Q_i are calculated from the recurrence relations

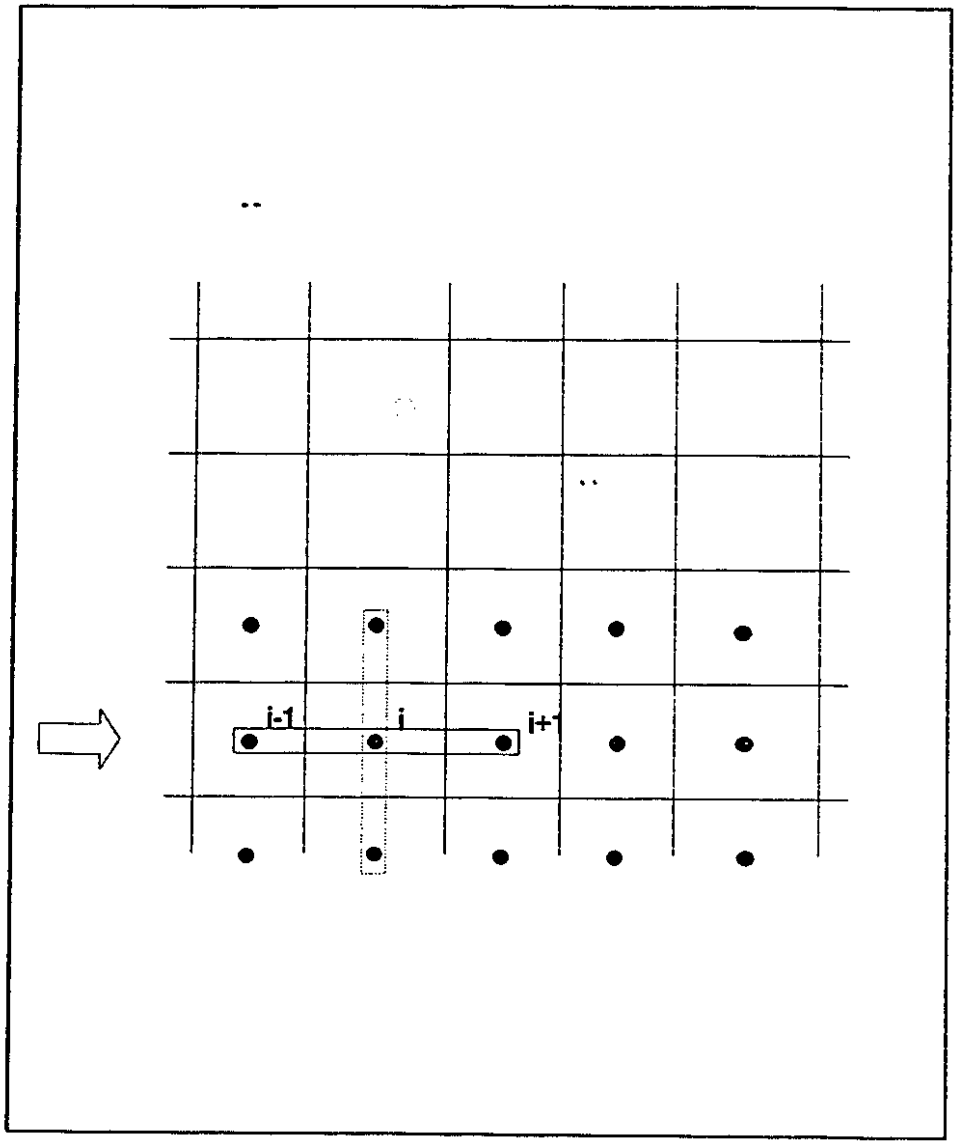

Fig.2.05: Line-by-line method

$$P_i = \frac{b_i}{(a_i - c_i P_{i-1})} \qquad 2.70$$

$$Q_i = \frac{(d_i + c_i Q_{i-1})}{(a_i - c_i P_{i-1})} \qquad 2.71$$

for i=2,l-1. The solution can be obtained by using

$$\theta_i = P_i \theta_{i+1} + Q_i \qquad 2.72$$

in the reverse order. The procedure requires a special treatment at the boundaries. When i=2

$$A_W = 0 \qquad d = d + A_W \theta_W \qquad 2.73$$

and when i=l-1

$$A_E = 0 \qquad d = d + A_E \theta_E \qquad 2.74$$

The above boundary modifications are not necessary if a small change is made to the algorithm. By setting $Q_1 = \theta_1$ and retaining the boundary coefficients, the boundary condition is automatically incorporated into the TDMA.

The line-by-line method consists of employing the TDMA along all the lines in the x direction. The procedure is then repeated along the lines in the y direction(Fig.2.05) and can be repeated until convergence is obtained.

A simple modification to the TDMA algorithm can accelerate the convergence significantly. The method is given in Van Doormaal and Raithby(1984). When sweeping from south to north, θ at the east grid point is approximated using

$$\theta_E^{old}=\theta_e^{old}+(\lambda-1)\,(\theta_p^{new}-\theta_p^{old}) \qquad 2.75$$

The discretized equation becomes

$$[B^p-A_E(\lambda-a)]\,\theta_P=A_W\theta_W+A_E[(\theta_E^{old})-(\lambda-1)\,\theta_P^{old}]+A_N\theta_N+A_S\theta_S+b \qquad 2.76$$

The TDMA algorithm is applied to the modified equation(Eq.2.76). The best result is obtained when λ is in the rage 1.6-1.95.

2.6.2 Block-Correction Scheme

The line-by-line method converges slowly if the initial starting value is very far from the solution. The purpose of the block-correction scheme is to obtain an approximate value of the final solution. Before the application of the line-by-line method, uniform corrections $\overline{\theta_i}$ are added along the lines of constant i. Therefore

$$\theta_{ij}=\theta_{ij}^{*}+\overline{\theta_i} \qquad 2.77$$

The corrections $\overline{\theta_i}$ are chosen such that the integral conservation over the control volume blocks defined by each constant-i line is exactly satisfied. The equation for the correction $\overline{\theta_i}$ is obtained by substituting Eq.2.68 into the original discretization equation and summing such equations for all values of j. The result is[Patankar(1981)]

$$A_i\overline{\theta_i}=B_i\overline{\theta_{i+1}}+C_i\overline{\theta_{i-1}}+D \qquad 2.78$$

where

$$B_i=\sum A_E \qquad 2.79a$$

$$A_i=\sum (B_P-A_N-A_S) \qquad 2.79b$$

$$C_i=\sum A_W \qquad 2.79c$$

$$D_i=\sum (A_E\theta_e^*+A_W\theta_w^*+A_N\theta_N^*+A_S\theta_S^*+d-B_P\theta_P^*) \qquad 2.79d$$

The summations in these expression are taken over j=2,m-1. The equation set can be solved by the TDMA. It should be noted that D_i represents the integral residual for the constant-i. The correction reduces all the integral residuals to zero. The same procedure is applied to the lines of constant j.

2.6.3 Diagonal Dominance

To obtain convergence with the iterative solution technique, an important condition needs to be satisfied. The discretization equation must be diagonally dominant. The coefficients must satisfy the following condition.

$$B_P \geq \sum_{nb} A_{nb} \qquad 2.80$$

First-order upwinding of the convective terms allows this requirement to be met. Therefore the iterative technique converge to a solution. The central differencing scheme

for the convection terms, when incorporated directly into the coefficients of the discretization equation does not meet the diagonal dominance condition generally. When the iterative solution technique is applied, the process may diverge.

This condition forces the implementation of higher-order upwinding for the convection terms in a certain manner if convergence is to be achieved. The implementation of higher-order upwinding methods is discussed in the next chapter in the context of three spatial dimensions.

3.0 Three Dimensional Method

Since the geometry of the RIM mixhead tube is a cylindrical chamber, the obvious choice of coordinates seems to be cylindrical coordinates. However, several difficulties are encountered if cylindrical coordinates are used. The jet inlet boundary conditions (e.g., fully developed parabolic profile) cannot be specified correctly and it would be difficult to consider more complicated mixhead geometries. To solve the problem without introducing simplifying assumptions, we need a more flexible method that can handle complex geometries.

There are several ways that the finite-volume method is used to treat problems in complex geometries. When simple Cartesian or cylindrical coordinates are used, the boundaries do not generally coincide with the coordinate lines and approximations to the boundary must be made. The first approach to overcome this difficulty is to treat the boundary as series of straight line segments and use interpolation. This method is not used frequently since the inaccurate interpolation at the boundaries degrades the accuracy of the numerical method considerably[Maliska and Raithby(1984)]. An alternative is to use the generalized coordinates(or body fitted coordinates). Two different approaches are possible with the generalized coordinates; general orthogonal and non-orthogonal coordinates. With an orthogonal coordinate system the mesh that can align the grid lines with the boundaries may be impossible to generate in a three dimensional space[Maliska and Raithby(1984)]. The generalized non-orthogonal curvilinear coordinate system is more

flexible than the orthogonal method with regards to mesh generation. The methods for the mesh generation are discussed extensively in the works by Thompson et. al(1985)].

With the generalized non-orthogonal coordinate system several different formulations are possible depending on the choice of the dependent variables. In most of previous formulations, Cartesian velocity components are chosen as the dependent variables. With this choice the Cartesian velocities can be located in many ways(Fig. 3.01). The Cartesian velocities can be staggered with the pressure at the cell center(Fig.3.01a). Shyy and his co-workers showed that a convergent calculation scheme can be developed[Shyy et al(1985) and Shyy and Vu(1991)]. However, the procedure breaks down when the grid lines are rotated by 90° [Vanka et. al(1985)]. Vanka et. al(1985) located pressures at the corners of the cells and velocities at the centers(Fig.3.01 b). This arrangement is also not satisfactory since an uneven pressure field may result as the solution. The third arrangement proposed by Maliska and Raithby(1984) locates all Cartesian components at the cell faces(Fig.3.01.c). This approach requires additional storage and computational effort. The fourth approach(Fig.3.01.d) is most economical in terms of the storage and computational efficiency. The Cartesian components are located at the cell centers with the pressure field, requiring least storage. A study performed by Melaaen(1992) showed that the grid non-orthogonality is handled better by the nonstaggered grid than a staggered grid.

Karki[1985] used the covariant velocity components as the dependent variable. The covariant velocities are aligned with the grid lines. Since these components are not normal to the cell faces, some averaging was necessary to calculate the normal flux. Another disadvantage of this method is that additional source terms arise due to the curvature effect[Shyy and Vu(1991)].

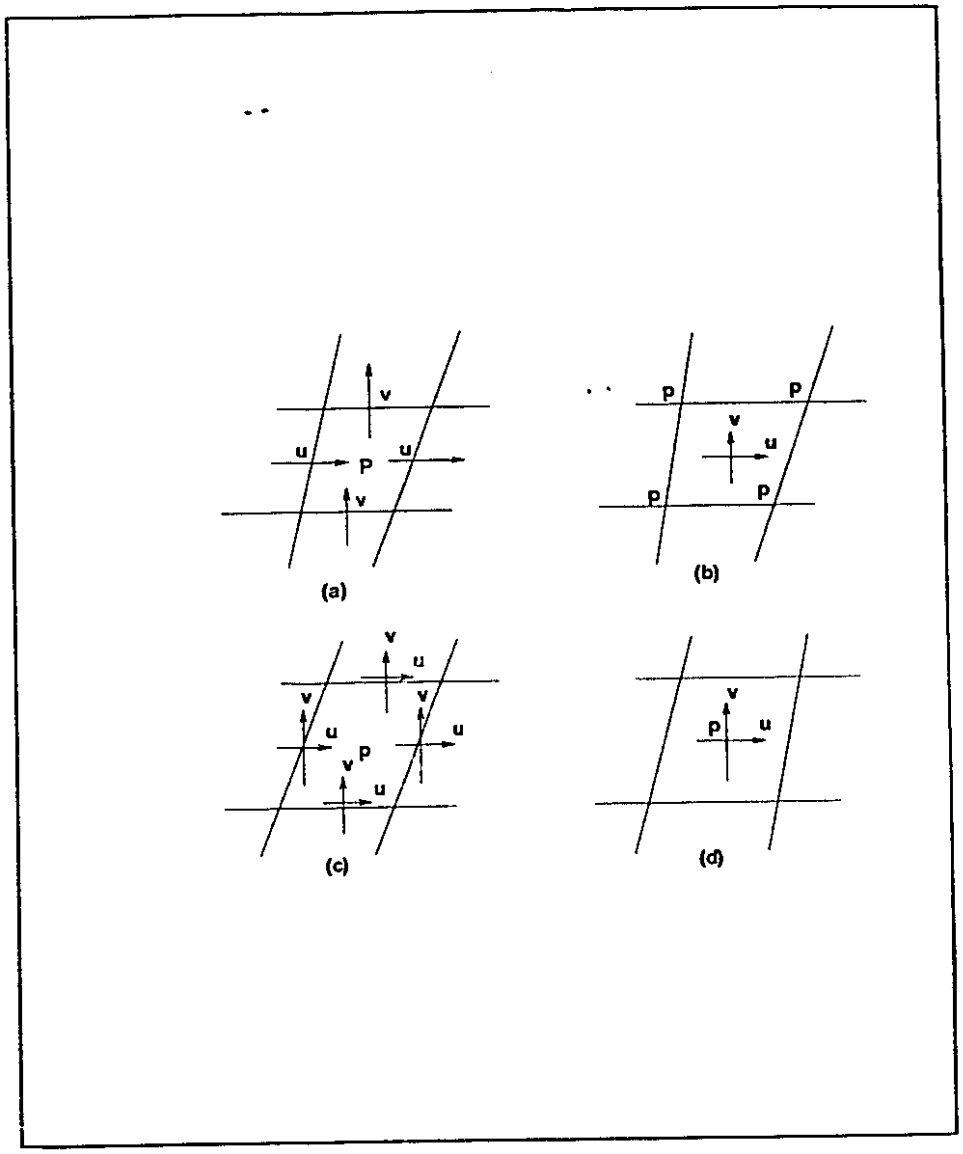

Fig.3.01: Possible cartesian velocity arrangements

In this chapter the details on the numerical method that has been developed to solve the 3-D transient Newtonian laminar flow in complex geometries are given. The Cartesian Navier-Stokes equations are transformed to the generalized non-orthogonal curvilinear coordinates. This transformation allows the computational physical boundary to coincide with a coordinate line in the transformed space.

The variables are discretized on a non-staggered mesh and second order accurate schemes for both convection and diffusion terms are used. The method is similar that of Rhie(1985) which was developed for 2-D turbulent flow. Yet, there are significant improvements with the interpolation of the cell boundary velocities. The original Rhie scheme has been the subject of controversy. The work of Acharya and Moukalled (1989) showed that mass conservation is not enforced with their scheme; therefore the solution obtained using their method is not accurate.

3.1 Governing Equations

Before introducing the governing equations, tensor notation is discussed briefly. Using tensor notation simplifies writing the three dimensional equations. The indexed variable, x_i, denotes (x,y,z). Repeated indices denote summation as shown below

$$\frac{\partial u_i}{\partial x_i} = \frac{\partial u}{\partial x} + \frac{\partial v}{\partial y} + \frac{\partial w}{\partial z} \qquad 3.01$$

For 3-D, laminar, Newtonian fluid flow the following equations describe the motion of incompressible fluid in a Cartesian coordinate system[Aris(1989)].

Continuity

$$\frac{\partial \rho u_i}{\partial x_i} = 0 \qquad 3.02$$

Momentum

$$\rho\left(\frac{\partial u_i}{\partial t} + \frac{\partial}{\partial x_j}(u_i u_j)\right) = -\frac{\partial P}{\partial x_i} + \frac{\partial}{\partial x_j}\left(\mu \frac{\partial u_i}{\partial x_j}\right) \qquad 3.03$$

Before proceeding further with the discussion of the transformations and discretizations, the following generalized transport equation is introduced in the tensor

$$\frac{\partial}{\partial t}(\rho\theta) + \frac{\partial}{\partial x_j}(\rho u_j \theta) = S^{\theta} + \frac{\partial}{\partial x_j}\left(\Gamma^{\theta} \frac{\partial \theta}{\partial x_j}\right) \qquad 3.04$$

notation.

As in Chapter 2, S^{θ} represents the pressure gradient source term. For the continuity equation θ equals to 1 and S^{θ} equals to 0.

3.2 Transformation

The transformation of a point in Cartesian coordinates to curvilinear coordinates is given by[Aris(1989)]

$$\epsilon^i = \epsilon^i(x, y, z) \tag{3.05}$$

The inverse transformation

$$x^i = x^i(\epsilon, \eta, \Gamma) \tag{3.06}$$

is assumed to be unique.

3.2.1 Jacobian and Inverse Jacobian

The first geometrical quantity that is defined is called the Jacobian or transform matrix.

$$J_j^i = \frac{\partial x^i}{\partial \epsilon^j} \tag{3.07}$$

The inverse Jacobian matrix is defined as.

$$\overline{J_j^i} = \frac{\partial \epsilon^i}{\partial x^j} \tag{3.08}$$

The equations written in Cartesian coordinates can be transformed to generalized non-orthogonal coordinates by applying transformation rules. The first-order derivative in generalized coordinates can be related to the first-order derivatives in Cartesian coordinates through the chain rule. For example

$$\frac{\partial \theta}{\partial \epsilon} = \frac{\partial \theta}{\partial x}\frac{\partial x}{\partial \epsilon} + \frac{\partial \theta}{\partial y}\frac{\partial y}{\partial \epsilon} + \frac{\partial \theta}{\partial z}\frac{\partial z}{\partial \epsilon} \tag{3.09}$$

The above equation can be generalized and rewritten using the tensor notation to give

$$\frac{\partial\theta}{\partial\epsilon^i}=\frac{\partial x^j}{\partial\epsilon^i}\frac{\partial\theta}{\partial x^j}=J_i^j\frac{\partial\theta}{\partial x^j} \qquad 3.10$$

Where J_i^j is the transpose of the Jacobian matrix.

The inverse transformation can be carried out similarly using the chain rule.

$$\frac{\partial\theta}{\partial x^j}=\frac{\partial\epsilon^k}{\partial x^j}\frac{\partial\theta}{\partial\epsilon^k}=\overline{J_j^k}\ \frac{\partial\theta}{\partial\epsilon^k} \qquad 3.11$$

Where $\overline{J_j^k}$ is transpose of the inverse Jacobian matrix.

The transformation of the governing equations given in the physical coordinate system to the new coordinate system gives rise to geometric derivatives expressed relative to the physical coordinate system(e.g., ε_x , ε_y , ε_z etc.). Since the physical coordinates are expressed as a function of the transformed coordinate system, we need to relate the inverse Jacobian matrix (ε_x , ε_y , ε_z etc.) to the Jacobian matrix ($x_\epsilon, y_\eta, y_\Gamma$ etc.).

For this we can use the identity,

$$\overline{J_k^j}\ J_l^k=\delta_l^j \qquad 3.12$$

Solving for the inverse Jacobian matrix($\overline{J_k^j}$) assuming that the Jacobian matrix(J_l^k) is known gives the following

$$\overline{J_1^1}=\epsilon_x=\frac{y_\eta z_\Gamma-y_\Gamma z_\eta}{|J|} \quad \overline{J_2^1}=\epsilon_y=\frac{x_\Gamma z_\eta-x_\eta z_\Gamma}{|J|} \quad \overline{J_3^1}=\epsilon_z=\frac{x_\eta y_\Gamma-x_\Gamma y_\eta}{|J|} \qquad 3.13a,b,c$$

$$\overline{J_2^1}=\eta_x=\frac{y_\Gamma z_\epsilon - y_\epsilon z_\Gamma}{|J|} \quad \overline{J_2^2}=\eta_y=\frac{x_\epsilon z_\Gamma - x_\Gamma z_\epsilon}{|J|} \quad \overline{J_2^3}=\eta_z=\frac{x_\Gamma y_\epsilon - x_\epsilon y_\Gamma}{|J|} \qquad 3.13d,e,f$$

$$\overline{J_3^1}=\Gamma_x=\frac{y_\epsilon z_\eta - y_\eta z_\epsilon}{|J|} \quad \overline{J_3^2}=\Gamma_y=\frac{x_\eta z_\epsilon - x_\epsilon z_\eta}{|J|} \quad \overline{J_3^3}=\Gamma_z=\frac{x_\epsilon y_\eta - x_\eta y_\epsilon}{|J|} \qquad 3.1.3g,h,i$$

$|J|$ is called the "Jacobian" and defined as the determinant of the Jacobian matrix

$$|J|=x_\epsilon y_\eta z_\Gamma + x_\eta y_\Gamma z_\epsilon + x_\Gamma y_\epsilon z_\eta$$

$$- x_\epsilon y_\Gamma z_\eta - x_\eta y_\epsilon z_\Gamma - x_\Gamma y_\eta z_\epsilon \qquad 3.14$$

3.2.2 Covariant and Contravariant Metric Tensors

The differential increment of length in Cartesian coordinates is

$$ds^2=dx^k dx^k \qquad 3.15$$

This can be related to the generalized coordinates as follows;

$$ds^2=\frac{\partial x^k}{\partial \epsilon^i}\frac{\partial x^k}{\partial \epsilon^j}d\epsilon^i d\epsilon^j \qquad 3.16$$

The covariant metric tensor

$$g_{ij}=\frac{\partial x^k}{\partial \epsilon^i}\frac{\partial x^k}{\partial \epsilon^j} \qquad 3.17$$

relates distance in the Cartesian coordinates to the infinitesimal coordinate increments in the generalized coordinate system.

The inverse of the covariant metric tensor can be defined. It is called the contravariant metric tensor.

$$g^{ij}=\frac{\partial \epsilon^k}{\partial x^i}\frac{\partial \epsilon^k}{\partial x^j} \qquad 3.18$$

3.2.3 Covariant and Contravariant Vectors and Normal Flux

In the new coordinate system, a Cartesian vector can be decomposed in two different ways. Let Cartesian basis vectors be denoted by i_i. Define a set of basis vectors such that they are normal to the coordinate surfaces(Fig3.02a)

$$e^{(i)}=\overline{J_k^i}i_k \qquad 3.19$$

The reciprocal(dual) basis vector which are tangents to the coordinate surfaces are defined as

$$e_{(i)}=J_i^k i_k \qquad 3.20$$

The basis vectors coincide only if the coordinates are orthogonal.

The contravariant components are normal vectors to the coordinate surfaces. These can be formed using the first set of basis vectors. For a Cartesian vector **u**, three contravariant components are given by

$$\overline{U^i}=u\bullet e^{(i)}=\frac{\partial \epsilon^i}{\partial x^j}u_j \qquad 3.21$$

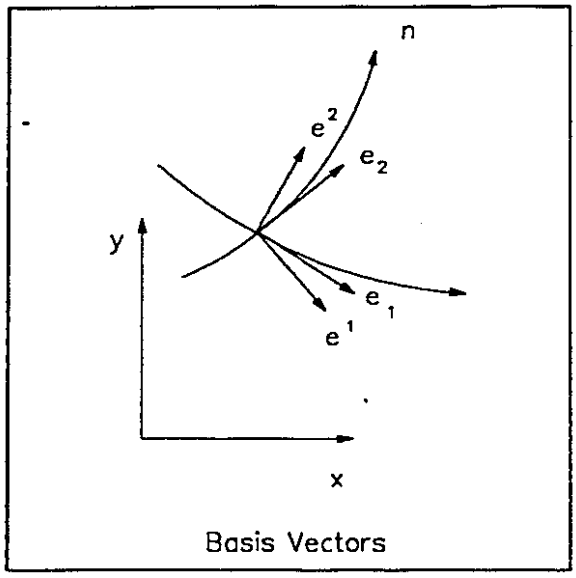
n
e²
e₂
y
e₁
e¹
x
Basis Vectors

a)

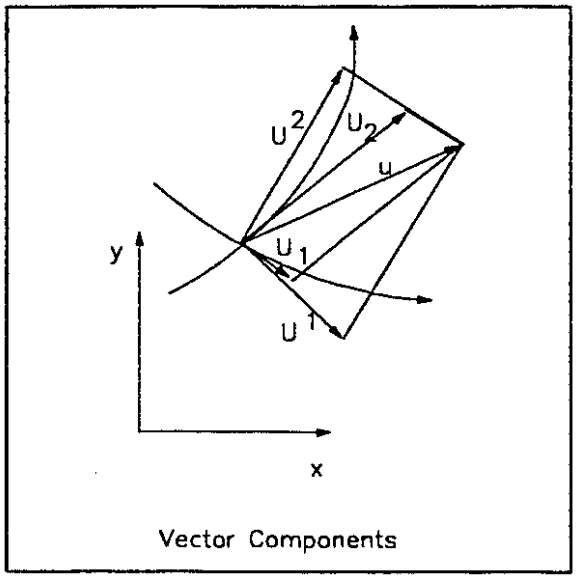
U²
U₂
u
y
U₁
U¹
x
Vector Components

b)

Fig.3.02

The covariant components, which are tangential vectors to the coordinate surfaces can be formed using the second set of basis vectors

$$\overline{U_i}=u\bullet e_{(i)}=\frac{\partial x^j}{\partial \epsilon^i}u_j \qquad 3.22$$

The contravariant and covariant components of a velocity vector are illustrated in Fig.3.02

The contravariant components of a velocity vector can be scaled by the Jacobian determinant to obtain the normal flux components.

$$U^i=|J|\overline{U^i}=|J|\frac{\partial \epsilon^i}{\partial x^j}u_j \qquad 3.23$$

The product of the Jacobian determinant and the transformation matrix gives the area vector.

$$A_j^i=|J|\frac{\partial \epsilon^i}{\partial x^j} \qquad 3.24$$

These are vectors with magnitude equal to the area of the face and direction perpendicular to the face. If the control volume has the dimensions($\Delta\epsilon,\Delta\eta,\Delta\Gamma$) in the computational space, the corresponding area in the physical space is given by

$$\Delta A^{\epsilon}=A^{\epsilon}\Delta\eta\Delta\Gamma \qquad 3.25$$

The three normal flux components of a velocity vector are given below.

$$U=|J|(\epsilon_x u+\epsilon_y v+\epsilon_z w)=A_j^1 u_j \qquad 3.26a$$

$$V=|J|(\eta_x u+\eta_y v+\eta_z w)=A_j^2 u_j \qquad 3.26b$$

$$W=|J|(\Gamma_x u+\Gamma_y v+\Gamma_z w)=A_j^3 u_j \qquad 3.26c$$

3.2.4 Transformed Equations

With the knowledge of the coordinate transformation relations presented above, we can proceed with the transformation of Eq.3.03. Two different transformation rules are applied. For source terms chain-rule differentiation is applied[Thompson et. al(1985), Rhie(1985), Meakin and Street(1988)]

$$\frac{\partial F}{\partial x^i}=\frac{\partial F}{\partial \epsilon^j}\frac{\partial \epsilon^j}{\partial x^i} \qquad 3.27$$

For the transport terms, a conservative transformation rule is applied[Thompson et al.(1985),Rhie(1985)]

$$\frac{\partial F}{\partial x^i}=\left(\frac{1}{J}\right)\frac{\partial}{\partial \epsilon^j}\left(JF\frac{\partial \epsilon^j}{\partial x^i}\right) \qquad 3.28$$

Application of these transformations to the Cartesian transport equations gives the following results

Continuity

$$\frac{\partial U^i}{\partial \epsilon^i}=0 \qquad 3.29$$

Transport Equations

$$\frac{\partial}{\partial t}(|J|\rho\theta)+\frac{\partial}{\partial \epsilon^i}(\rho U^i\theta) = S^\theta|J|+\frac{\partial}{\partial \epsilon^i}(G^{ik}\Gamma^\theta\frac{\partial\theta}{\partial \epsilon^k}) \qquad 3.30$$

where U^i are the normal flux components given in Eq. 3.22, and $G^{ik}=|J|g^{ik}$.

3.3 Discretization

The Navier-Stokes equations written in generalized coordinates are discretized using the finite-volume method. The steps outlined in the previous chapters are followed.

3.3.1 Grid Structure

The computational space has a uniform rectangular domain of dimensions l x m x n. The computational domain is divided into a number control volumes. In three dimensions, the control volumes are cubes with unit boundary surface areas. The terminology used for the control volumes is illustrated in Fig.3.03. The capital letters denote the cell centers and small letters, the cell faces. The cell center coordinates are stored in the three dimensional arrays x(i,j,k),y(i,j,k) and z(i,j,k). The cell corners are stored in another set of three dimensional arrays xc(i,j,k),yc(i,j,k) and zc(i,j,k). The cell centers are the centroids of the control volumes. The transport equations are discretized by constructing discrete conservation laws for the control volumes.

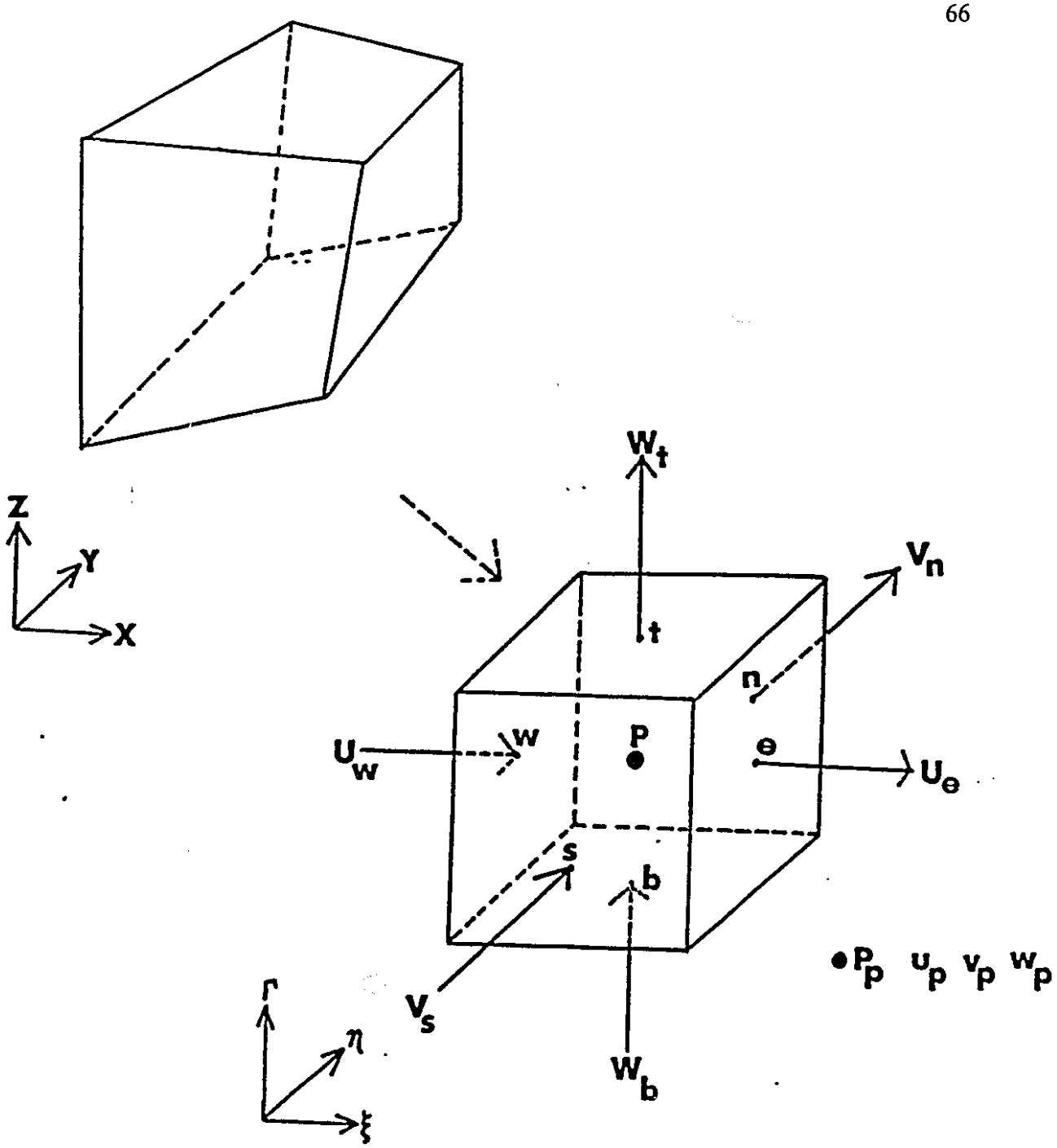

Fig.3.03: 3-D Contol volume

3.3.2 Geometric Quantities

As shown by Rosenfeld et al.(1991), an accurate discretization in the curvilinear coordinates requires the geometric conservation rule to be obeyed. The geometric conservation rule arises because of the conservative formulation. Eq. 3.28 implies

$$\frac{\partial}{\partial \epsilon^j}\left(J\frac{\partial \epsilon^j}{\partial x^i}\right)=0.0 \qquad 3.31$$

This equation says the sum of area vectors for the control volume should be zero, or that the individual control volume is closed.

To enforce this rule, the geometric quantities must be evaluated at the control volume faces. The interpolation of the cell center values to the cell face may violate the geometric conservation rule [Thompson et al.(1985), Rosenfeld et al.(1991)]. Evaluation of the Jacobian matrix is illustrated for the east face.

$$(x^i_\epsilon)_e=\frac{x^i(i+1,j,k)-x^i(i,j,k)}{\Delta\epsilon} \qquad 3.32$$

$$(x^i_\eta)_e=\frac{xc^i(i,j,k)-xc^i(i,j-1,k)+xc^i(i,j,k-1)-xc^i(i,j-1,k-1)}{2\Delta\eta} \qquad 3.33$$

$$(x^i_\Gamma)_e=\frac{xc^i(i,j,k)-xc^i(i,j,k-1)+xc^i(i,j-1,k)-xc^i(i,j-1,k-1)}{2\Delta\Gamma} \qquad 3.34$$

determinant can be determined using Eq. 3.14. The inverse Jacobian can be used to determine the contravariant metric tensor.

3.3.3 Integral Conservation Statement

Eq.3.30 is integrated over the control volume to construct the integral conservation statement

$$\int_{\Delta Vol}[\frac{\partial}{\partial t}(|J|\rho\theta)+\frac{\partial}{\partial\epsilon^i}(\rho U^i\theta-\Gamma^\theta g^{ik}|J|\frac{\partial\theta}{\partial\epsilon^k})]dV=\int_{\Delta Vol}S^\theta|J|dV \qquad 3.35$$

$$\Delta V=\Delta\epsilon\Delta\eta\Delta\Gamma$$

This equation states that the net accumulation rate of θ within a control volume is balanced by the net convective and diffusive fluxes across the control volume faces and the source or sink terms within the control volume. In the finite-volume method, the integral conservation statement is discretized rather than the original differential equation.

Several assumptions are introduced. The fluxes through the control volume boundaries are expressed as the product of the mean value through the face and the area of the control volume face. The source term is expressed as the product of the mean value associated with the cell center and the cell volume. The equation is linearized by substituting the unknown variables by the values from the previous iteration step. For example with the first convection term

$$\int_{\Delta Vol} \frac{\partial}{\partial \epsilon}(\rho U\theta)\, dV = \int_{\Delta Vol} \frac{\partial}{\partial \epsilon}(\rho U^{*}\theta) dV \qquad 3.36$$

The result is

$$\frac{\partial(\rho |J|\theta)}{\partial t}\Delta \dot{Vol} + [(\rho U^{*}\theta - \Gamma^{\theta} g^{1k} |J| \frac{\partial \theta}{\partial \epsilon^{k}})_{e} - (\rho U^{*}\theta - \Gamma^{\theta} g^{1k} |J| \frac{\partial \theta}{\partial \epsilon^{k}})_{w}]\Delta\eta\Delta\Gamma$$

$$+[(\rho V^{*}\theta - \Gamma^{\theta} g^{2k} |J| \frac{\partial \theta}{\partial \epsilon^{k}})_{n} - (\rho V^{*}\theta - \Gamma^{\theta} g^{2k} |J| \frac{\partial \theta}{\partial \epsilon^{k}})_{s}]\Delta\epsilon\Delta\Gamma$$

$$[(\rho W\theta - \Gamma^{\theta} g^{3k} |J| \frac{\partial \theta}{\partial \epsilon^{k}})_{t} - (\rho W\theta - \Gamma^{\theta} g^{3k} |J| \frac{\partial \theta}{\partial \epsilon^{k}})_{b}]\Delta\epsilon\Delta\eta = S^{\theta} |J| \Delta Vol \qquad 3.37$$

3.3.4 Time Derivative

A first-order backward time difference is used. This scheme is unconditionally stable for an arbitrary time step size Δt.

$$\frac{\partial(\rho |J|\theta)}{\partial t}\Delta V = \frac{(\rho |J|\theta) - (\rho |J|\theta)^{\circ}}{\Delta t}\Delta\epsilon\Delta\eta\Delta\Gamma \qquad 3.38$$

The convective and diffusive fluxes are evaluated at the present time level. Only the term denoted with $^{\circ}$ is evaluated in the past time.

3.3.5 Diffusion Terms

Owing to non-orthogonality, the diffusion terms contain cross derivatives. At the

east face, the diffusion term fully expanded is;

$$(\Gamma^{\theta} g^{1k} |J| \frac{\partial \theta}{\partial \epsilon^k})_e = (\Gamma^{\theta} g^{11} |J| \frac{\partial \theta}{\partial \epsilon})_e + (\Gamma^{\theta} g^{12} |J| \frac{\partial \theta}{\partial \eta})_e + (\Gamma^{\theta} g^{13} |J| \frac{\partial \theta}{\partial \Gamma})_e \qquad 3.39$$

Central differences are used for the derivatives.

$$(\frac{\partial \theta}{\partial \epsilon})_e = \frac{\theta_E - \theta_P}{\Delta \epsilon} \qquad 3.40$$

$$(\frac{\partial \theta}{\partial \eta})_e = \frac{\theta_{ne} - \theta_{se}}{\Delta \eta} \qquad 3.41$$

$$(\frac{\partial \theta}{\partial \Gamma})_e = \frac{\theta_{te} - \theta_{be}}{\Delta \Gamma} \qquad 3.42$$

3.3.6 Convection Term

Discretization of the convection terms is important in obtaining accurate solutions to computational fluid dynamics problems. The first-order upwinding method presented in Chapter 2 is the simplest stable scheme for the discretization of the convection terms. However the use of this scheme produces inaccurate results due to the false diffusion error[De Vahl Davis and Mallison(1976), Leonard(1979)]. At high Reynolds numbers, false diffusion plays an important role, producing solutions which contain artificially higher levels of diffusion. Several proposals have been made to improve the accuracy of the convection term discretization. Some of the proposals contained in the literature are briefly reviewed below. A method of implementing higher-order upwinding schemes is presented. The discussion for each method begins with the finite-difference analog of the convective derivative since the finite-difference is more easily conceptualized.

3.3.6.1 First-Order Upwinding

A more detailed discussion of the method than in Chapter 2 is presented. When a convective derivative is discretized using the first-order upwinding scheme, the following result is obtained.

$$\frac{\partial(U\,\theta)}{\partial\epsilon}=\begin{cases} U_P\dfrac{\theta_P-\theta_W}{\Delta\epsilon}+\alpha\dfrac{\partial^2\theta}{\partial\epsilon^2} & \text{if } U_P>0 \\ U_P\dfrac{\theta_E-\theta_P}{\Delta\epsilon}-\alpha\dfrac{\partial^2\theta}{\partial\epsilon^2} & \text{if } U_P<0 \end{cases} \qquad 3.43$$

The derivative is discretized at the cell center. Grid points are equidistant with $\Delta\varepsilon$ as the spacing. This method introduces a nonphysical coefficient $\alpha=\frac{1}{2}U\Delta\epsilon$ which is called the numerical or artificial diffusivity of the upwind scheme. When convection becomes dominant this term introduces a diffusive effect which does not physically exist.

In the control volume sense this scheme is equivalent to step wise interpolation(Fig.3.4). The contribution from the convection coefficients for the 3-D scheme are given below.

$$C_E^{\theta}=\max[-\rho\ U_e\Delta\eta\Delta\Gamma,\ \ 0.0] \qquad 3.44a$$

$$C_w^{\theta}=\max[\ \rho U_w \Delta\eta\Delta\Gamma,\ 0.0] \qquad 3.44b$$

$$C_N^{\theta}=\max[-\rho V_n \Delta\epsilon\Delta\Gamma,\ 0.0] \qquad 3.44c$$

$$C_S^{\theta}=\max[\ \rho V_s \Delta\epsilon\Delta\Gamma,\ 0.0] \qquad 3.44d$$

$$C_T^{\theta}=\max[-\rho W_t \Delta\epsilon\Delta\eta,\ 0.0] \qquad 3.44e$$

$$C_B^{\theta}=\max[\ \rho W_b \Delta\epsilon\Delta\eta,\ 0.0] \qquad 3.44f$$

Although smooth converged solutions can be obtained with this method, extensive studies[Han et.al(1981),Shyy(1985)] show that the method fails to give accurate solutions at high Reynolds numbers. Due to the false diffusion error, the strength of motion is severely underpredicted. For recirculating flows, the method predicts weaker vortices and sometimes an incorrect flow field[De Vahl Davis and Mallison(1976)].

3.3.6.2 Flux Blending

This scheme, first proposed by Khosla and Rubin(1974) blends first-order upwinding with a central differencing scheme to obtain a more accurate discretization for the convection terms. The finite-difference representation of this scheme is

$$\frac{\partial(U\theta)}{\partial\epsilon}=\begin{cases} U_P\dfrac{\theta_P-\theta_W}{\Delta\epsilon}+\lambda U_P\left(\dfrac{\theta_E-\theta_W}{2\Delta\epsilon}-\dfrac{\theta_P-\theta_W}{\Delta\epsilon}\right) & U_P>0 \\ U_P\dfrac{\theta_E-\theta_P}{\Delta\epsilon}+\lambda U_P\left(\dfrac{\theta_E-\theta_W}{2\Delta\epsilon}-\dfrac{\theta_E-\theta_P}{\Delta\epsilon}\right) & U_P<0 \end{cases} \qquad 3.45$$

The terms enclosed within the round brackets are included in the right-hand side

(source term) of the matrix equation and are evaluated using the values from the previous iteration step. This is called the deferred correction approach and allows the stability of the first-order upwind scheme for the higher-order schemes. The blending factor λ can be between 0 and 1. When λ is 0 the scheme becomes the first-order upwinding and when λ is 1 the scheme becomes central differencing. The optimum value of λ damps out the wiggles due to central differencing.

The flux-blending scheme is not implemented in this work, since it is difficult to obtain the optimum λ which damps out numerical oscillations. The implementation of the higher-order upwinding follows the deferred correction approach. The higher-order scheme is split between a stable upwinding scheme plus source terms which lag behind one iteration.

3.3.6.3 Second-Order Upwinding

A better approximation of the cell face value would be to use two upstream nodal values to find the cell face value(Fig.3.04).

For the east and west faces[Shyy (1985)]:

$$\theta_e = \begin{cases} 1.5\theta_P - .5\theta_W & U^e > 0 \\ 1.5\theta_E - .5\theta_{EE} & U^e < 0 \end{cases} \qquad 3.46a$$

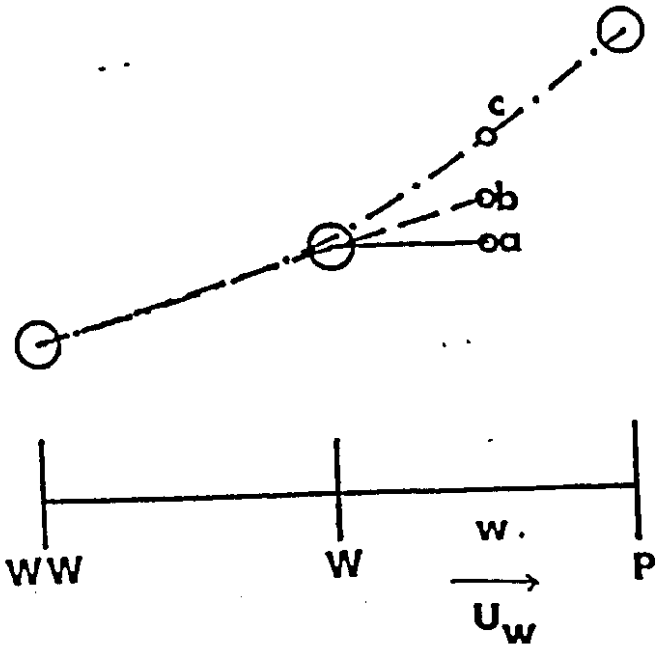

a) First-Order Upwinding

b) Second-Order Upwinding

c) QUICK

Fig.3.04 : Higher-order upwind schemes

$$\theta_w=\begin{cases}1.5\theta_W-.5\theta_{WW} & U^w>0\\ 1.5\theta_p-.5\theta_E & U^w<0\end{cases} \qquad 3.46b$$

To retain the diagonal dominance of the discretized equations, some terms must be grouped with the source term. The formulation that ensures this is first-order upwinding with the remaining terms grouped with the source term. The coefficients retain the same form as the first-order upwinding method and the remaining terms are lumped with the source term. The value of the variable at the faces can be written as

$$\theta_e=\begin{cases}\theta_P+S_e & S_e=.5(\theta_P-\theta_W) & U^e>0\\ \theta_E+S_e & S_e=.5(\theta_E-\theta_{EE}) & U^e<0\end{cases} \qquad 3.47a$$

$$\theta_w=\begin{cases}\theta_W+S_w & S_w=.5(\theta_P-\theta_W) & U^w>0\\ \theta_P+S_w & S_w=.5(\theta_P-\theta_E) & U^w<0\end{cases} \qquad 3.47b$$

The source term in Eq.3.37 contains the contributions from Eq.3.47a and Eq.3.47b and the similar formulation from the remaining faces. Therefore,

$$S_a^\theta=s_a^\theta+(CW\cdot S_w-CE\cdot S_e)+(CS\cdot S_e-CN\cdot S_n)+(CS\cdot S_b-CT\cdot S_t) \qquad 3.48$$

3.3.6.4 QUICK

If a third node is included, a higher-order approximation can be obtained[Leonard(1979)]. This method is equivalent to fitting a polynomial, $\theta_{\nu}=C_1+C_2\varepsilon+C_3\varepsilon^2$ with upstream weighting. For east and west faces the approximations for θ are

$$\theta_e=\begin{cases}\frac{3}{8}\theta_E-\frac{1}{8}\theta_W+\frac{3}{4}\theta_P & U^e>0\\ \frac{3}{8}\theta_P-\frac{1}{8}\theta_{EE}+\frac{3}{4}\theta_E & U^e<0\end{cases} \qquad 3.49a$$

$$\theta_w=\begin{cases}\frac{3}{8}\theta_P-\frac{1}{8}\theta_{WW}+\frac{3}{4}\theta_W & U^w>0\\ \frac{3}{8}\theta_W-\frac{1}{8}\theta_E+\frac{3}{4}\theta_P & U^w<0\end{cases} \qquad 3.49b$$

The QUICK scheme, depending on the method of implementation may yield coefficients which can become negative, thus destroying the diagonal dominance condition. Various workers have experimented with different forms and many of them found convergence problems. To obtain convergence, a false transient term must be added or a very small relaxation factor must be used [Han et. al(1981),Pollard and Siu(1982)]. To achieve stability, the scheme must be recast into a diagonally dominant form. As with second-order upwinding; first-order upwinding, with the remaining terms lumped with the source term, can ensure diagonal dominance and stability. Therefore,

$$\theta_e=\begin{cases}\theta_P+S_e & S_e=\frac{1}{8}(3\theta_E-2\theta_P-\theta_W) \quad U^e>0\\ \theta_E+S_e & S_e=\frac{1}{8}(3\theta_P-2\theta_E-\theta_{EE}) \quad U^e<0\end{cases} \tag{3.50a}$$

$$\theta_W=\begin{cases}\theta_W+S_w & S_w=\frac{1}{8}(3\theta_P-2\theta_W-\theta_{WW}) \quad U^w>0\\ \theta_P+S_w & S_w=\frac{1}{8}(3\theta_W-2\theta_P-\theta_E) \quad U^w<0\end{cases} \tag{3.50b}$$

In the study of Shyy(1985), the QUICK scheme generated spurious numerical oscillations which were not as serious as with central differencing. In some problems, the oscillations were serious enough to affect the accuracy of solution, however.

3.3.7 Discretization Equation

Substituting the individual term discretization into the integral conservation statement(Eq.3.37) gives the final discretization equation.

$$A_P\theta_P=\sum_{nb}A_{nb}\theta_{nb}+S^\theta \tag{3.51}$$

The individual terms are given by

$$A_E=CE+(\Gamma^\theta G^{11})_e \tag{3.52a}$$

$$A_W=CW+(\Gamma^\theta G^{11})_w \tag{3.52b}$$

$$A_N=CN+(\Gamma^\theta G^{22})_n \tag{3.52c}$$

$$A_S=CS+(\Gamma^{\theta}G^{22})_s \qquad 3.52d$$

$$A_T=CT+(\Gamma^{\theta}G^{33})_t \qquad 3.52e$$

$$A_B=CB+(\Gamma^{\theta}G^{33})_b \qquad 3.52f$$

$$A_P=A_E+A_W+A_N+A_S+A_T+A_B \qquad 3.53$$

The coefficients can have an alternate form if the non-orthogonality terms are included with the coefficients. The non-orthogonality terms are included with the source term S^{θ}.

Since the equations are nonlinear, underrelaxation is provided using the parameter α[Patankar(1981a), Patankar(1981b). The discretization equation(Eq.3.51) is modified to

$$B_P\theta_P=\sum_{nb} A_{nb}\theta_{nb}+S^{\theta} \qquad 3.54$$

and

$$B_P=\frac{A_P}{\alpha} \qquad 3.55$$

$$S^{\theta}=S^{\theta}+\frac{(1-\alpha)}{\alpha}A_P\theta_P \qquad 3.56$$

3.4 Pressure-Velocity Coupling

The discussion up to this point focused upon the discretization of the generalized transport equation. In this section the numerical method used for the solution of the

Navier-Stokes equations in generalized non-orthogonal curvilinear coordinate system is discussed.

3.4.1 Discretized Navier-Stokes Equations

The discretized momentum equations contain the dot product of pressure derivatives and the area vector. The discretized momentum equation is

$$B_P u_P^i = \sum_{nb} A_{nb} u_{nb}^i + S^{u^i} + |J|\left(\frac{\partial \epsilon^j}{\partial x^i}\frac{\partial P}{\partial \epsilon^j}\right) \qquad 3.57$$

The discretized continuity equation is

$$U_e - U_w + V_n - V_s + W_t - W_b = 0 \qquad 3.58$$

3.4.2 Evaluation of the Cell Face Velocities

When a non-staggered grid arrangement is used, a linear interpolation of the cell grid velocities to obtain the cell face velocities can lead to wiggles and oscillations in the velocity and pressure field. A method to overcome this difficulty was to use the staggered grid. The staggered grid method is compact and efficient for the Cartesian coordinates in two dimensions. However, with 3-D curvilinear coordinates, four-sets of control volumes are required and the storage of the geometric coefficients for four-sets of control volumes would require a large amount of computer memory. The non-staggered grid method first proposed by Rhie(1981) allows the velocities and pressure to be defined at the same grid points. The implementation of this method in two-dimensional Cartesian coordinates is

discussed in Chap. 2. Here, Rhie's scheme is extended to a three-dimensional non-orthogonal coordinate system. The implementation in non-orthogonal curvilinear coordinates is discussed in Burns and Wilkes(1987) , Rodi et al(1989), and Kobayashi and Pereira(1991). Other approaches are possible with the non-staggered grid system. Thiart(1990) uses pressure upwinding. Regio and Camarero(1986,1987) use opposed differencing.

The method proposed by Rhie is described first. A straight forward interpolation of the normal flux at the east face can be written as

$$U_e=0.5(U_E+U_P)=\overline{U_e} \tag{3.59}$$

The overbar denotes the linearly interpolated quantities at the location indicated by the subscript. The linear interpolation of the normal flux contains the pressure gradient which is the average of central differencing. Rhie(1981) proposes that the pressure gradient evaluated at the cell center is substituted with the pressure gradient that is evaluated directly at the face. Therefore

$$U_e=\overline{U_e}+\overline{C_e}\left(\overline{\left(\frac{\partial P}{\partial \epsilon}\right)_e}-\left(\frac{\partial P}{\partial \epsilon}\right)_e\right) \tag{3.60}$$

where

$$\overline{C_e}=\left(\frac{\overline{|J|^2 g^{ii}}}{A_P}\right)_e \tag{3.61}$$

Several workers examined this method and arrived at the conclusion that the

$$\overline{C_e}=\overline{(\frac{|J|^2 g^{ii}}{A_P})_e} \qquad 3.61$$

Several workers examined this method and arrived at the conclusion that the solution obtained with Rhie's original method may create problems. Majumdar(1988) showed that the solution obtained with Rhie's method depends upon the under-relaxation factor α, due to the presence of linearly interpolated underrelaxed velocities. The study of Acharya and Mukalled (1989) showed that Rhie's scheme failed to enforce mass conservation for skewed grids. This may be attributed to the way the contravariant velocities were evaluated at the cell faces. The pressure gradient correction(Eq.3.60) provided to the averaged normal fluxes may not represent the true mass imbalance at each iteration step[Acharya and Moukalled(1989)].

To overcome the difficulty with enforcement of mass conservation, the Cartesian velocities are interpolated to cell faces and the pressure gradient correction is applied. The corrected Cartesian velocities are then transformed to the normal fluxes using Eq.3.26. This route requires less averaging of the geometric information and the geometric conservation rule is not violated.

At the cell centers E and P the equation for the u-momentum can be written as

$$u_P=\frac{1}{B_P}((\sum_{nb} A_{nb}u_{nb})_P+S^P-(A_1^1 P_\epsilon+A_1^2 P_\eta+A_1^3 P_\Gamma)_P)+(1-\alpha)u_P^{\circ} \qquad 3.62$$

centers are substituted by the cell face values which are stored. For the pressure gradient in the main direction(ε-direction for east face velocity), the neighbouring cell grid pressures(E and P location pressures) are used to evaluate the pressure gradient.

$$u_e=\frac{1}{\overline{B_e}}(\overline{(\sum_{nb} A_{nb}u_{nb})_e+S^u-(A_1^2P_\eta+A_1^3P_\Gamma)_e})-(A_1^1P_\epsilon)_e+(1-\alpha)u_e^\circ$$

$$=\overline{H_e}-(A_1^1P_\epsilon)_e+(1-\alpha)u_e^\circ \qquad 3.64$$

Therefore, the cell face Cartesian velocity consists of three parts; 1) a linearly interpolated part which consists of the coefficients and the pressure gradients in the transverse directions, 2) the pressure source term in the main direction, and 3) the under-relaxed part.

The other Cartesian components, v_e and w_e are evaluated using a similar method. The normal flux components are determined using Eq.3.26. The normal flux component at the east face can be written as

$$U_e=A_1^1\overline{H_e^u}+A_2^1\overline{H_e^v}+A_3^1\overline{H_e^w}-\frac{A_i^1A_i^1}{\overline{B_e}}(\frac{\partial P}{\partial \epsilon})_e+(1-\alpha)U_e^\circ \qquad 3.65$$

The normal flux at other faces can be determined in a similar manner.

3.4.3 SIMPLEC Algorithm

The problem of finding pressure that satisfies continuity is more complex in the non-orthogonal curvilinear coordinate system. The continuity equation must be used to find the pressure field indirectly. When a correct pressure field is obtained, the velocity satisfies the continuity constraint.

In non-orthogonal coordinates, continuity is written in terms of the normal fluxes. The normal flux at each face is linked to all three components of the Cartesian velocity. The normal fluxes and cell center Cartesian velocities need to be corrected to drive the velocity field to convergence. The corrections can be written as

$$U=U^*+U' \tag{3.66a}$$

$$V=V^*+V' \tag{3.66b}$$

$$W=W^*+W' \tag{3.66c}$$

$$u=u^*+u' \tag{3.66d}$$

$$v=v^*+v' \tag{3.66e}$$

$$w=w^*+w' \tag{3.66f}$$

Initial solutions are obtained with the guessed pressure field p^*.

$$B_P u_P^* = \left(\sum_{nb} A_{nb} u_{nb}^* + S^u - \left(J\frac{\partial \epsilon_j}{\partial x}\frac{\partial P^*}{\partial \epsilon_j}\right)\right)_P \tag{3.67a}$$

$$B_E u_E^* = (\sum_{nb} A_{nb} u_{nb}^* + S^u - (J \frac{\partial \epsilon_j}{\partial x} \frac{\partial P^*}{\partial \epsilon_j}))_E \qquad 3.67b$$

The corrected solution is

$$B_P u_P = (\sum_{nb} A_{nb} u_{nb} + S^u - (J \frac{\partial \epsilon_j}{\partial x} \frac{\partial P}{\partial \epsilon_j}))_P \qquad 3.68a$$

$$B_E u_E = (\sum_{nb} A_{nb} u_{nb} + S^u - (J \frac{\partial \epsilon_j}{\partial x} \frac{\partial P}{\partial \epsilon_j}))_E \qquad 3.68b$$

The correction can be derived by subtracting Eq.3.67 from Eq.3.68. The result is

$$B_P u_P' = (\sum_{nb} A_{nb} u_{nb}' - (J \frac{\partial \epsilon_j}{\partial x} \frac{\partial P'}{\partial \epsilon_j}))_P \qquad 3.69a$$

$$B_E u_E' = (\sum_{nb} A_{nb} u_{nb}' - (J \frac{\partial \epsilon_j}{\partial x} \frac{\partial P'}{\partial \epsilon_j}))_E \qquad 3.69b$$

The equations relate the velocity corrections to the pressure corrections in all directions. If the pressure corrections are retained in all directions the resulting pressure correction equation would involve 15 points. This is not tractable using the tridiagonal matrix algorithm and a more complex matrix solution technique is required. To obtain the solution to the pressure correction, without resorting to special solvers, an approximation is introduced where the pressure correction only in the main direction is taken into

account. The u velocity correction is related to the pressure correction in ε-direction only, and for v and w velocity corrections the pressure correction in the η and Γ directions are used respectively. This approximation is valid if the grid does not contain severe non-orthogonality.[Shyy et. al(1985), Peric(1990)]

The SIMPLEC[Van Doormal and Raithby(1987)] approximations require that $\sum_{nb} A_{nb} u'_P$ and $\sum_{nb} A_{nb} u'_E$ are subtracted from Eq.3.69a and Eq.3.69b respectively. Therefore

$$u'_e = -\left(\frac{\overline{1}}{(B - A_{nb})}\right) A_1^1 (P'_E - P'_P) \qquad 3.70$$

Similar equations can be written for other Cartesian components. The normal flux correction can be written as

$$U' = A_1^1 u' + A_2^1 v' + A_3^1 w' \qquad 3.71$$

Therefore

$$U' = -A_1^i A_1^i \frac{\overline{1}}{(B - \sum A_{nb})_e} (P_E - P_P) \qquad 3.72$$

For other cell faces similar normal flux corrections can be derived.

Substituting the above equations into the continuity equation yields

$$A_P P'_P = A_E P'_E + A_W P'_W + A_N P'_N + A_S P'_S + A_T P'_T + A_B P'_B + b \qquad 3.73$$

where

$$A_E=(A_1^i A_1^i)_e \overline{\frac{1}{(B-\sum A_{nb})_e}} \qquad 3.74a$$

$$A_W=(A_1^i A_1^i)_w \overline{\frac{1}{(B_W-\sum A_{nb})_w}} \qquad 3.74b$$

$$A_N=(A_2^i A_2^i)_n \overline{\frac{1}{(B_N-\sum_{nb} A_{nb})_n}} \qquad 3.74c$$

$$A_S=(A_2^i A_2^i)_s \overline{\frac{1}{(B_S-\sum_{nb} A_{nb})_S}} \qquad 3.74d$$

$$A_T=(A_3^i A_3^i)_t \overline{\frac{1}{(B_T-\sum_{nb} A_{nb})}} \qquad 3.74e$$

$$A_B=(A_3^i A_3^i)_b \overline{\frac{1}{(B_B-\sum_{nb} A_{nb})_b}} \qquad 3.74f$$

and

$$A_P=A_N+A_S+A_E+A_W+A_T+A_B \qquad 3.75$$

$$b=-(U_e^*-U_w^*+V_n^*-V_s^*+W_t^*-W_b^*) \qquad 3.76$$

The iteration steps can be summarized as follows.

i) Using the guessed pressure field (p^*) and cell face normal fluxes(U^*,V^*,W^*)obtain the solutions to the momentum equations (u^*,v^*,w^*).

2) Obtain the cell face velocities using the method outlined in section 3.4.2.

3) Solve the pressure correction equation to obtain corrections to the pressure field(p') and correct the cell face normal fluxes and pressure.

4) Check for convergence.

5) If the iteration is not converged return to step 1) using the result as the initial guess.

6) If converged, end iteration process.

The discretization equations are solved using the block-correction method and the line-by-line sweep using the TDMA algorithm. The one dimensional algorithm is applied plane by plane in all three directions. The implementation of this method is discussed in the previous chapter.

4. Test Problems

Before applying the method developed in the previous chapters to the impinging jet problem, a rigorous test of the method is necessary to establish its accuracy. The code developed is used to solve various problems with previously published solutions. The problems selected test various aspects of the algorithm. The driven cavity problem, at high Reynolds numbers, test the accuracy of the convection term discretization. The driven cavity problem is solved using both rectangular Cartesian and non-orthogonal coordinate systems. The polar cavity problem tests the accuracy of the method using an orthogonal curvilinear grid system. Finally, the three-dimensional aspect of the algorithms is tested using the 90-deg bend rectangular duct.

4.1 Driven Cavity

The two dimensional driven cavity problem solves the flow field in a square cavity with the top of the cavity moving at a constant speed. The geometry of this flow field is rather simple and shown in Fig. 4.01a. The Reynolds number for this flow field is based on the cavity length.

$$Re = \frac{\rho u d}{\mu} \qquad 4.01$$

Where ρ is the density of fluid, u is the velocity of the lid and d is the dimension of

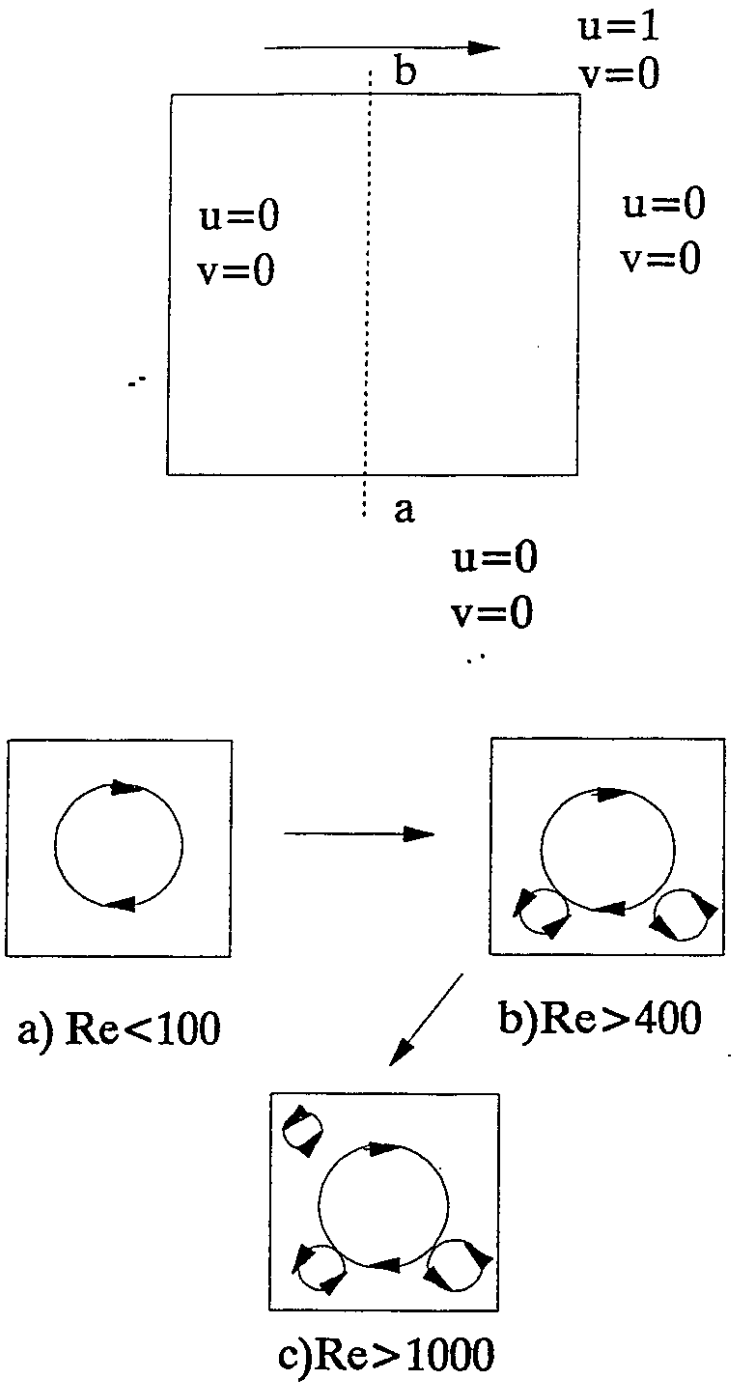

Fig.4.01:Driven cavity schematic solution forms

for given boundary condition

cavity.

The governing equations are two-dimensional Cartesian equations.

$$\frac{\partial}{\partial x_i}(\rho u_j u_i) = -\frac{\partial p}{\partial x_i} + \frac{\partial}{\partial x_i}(\mu \frac{\partial u_j}{\partial x_i}) \qquad 4.02$$

$$j=1,2$$

The problem is made dimensionless by normalizing the variables. The velocities are normalized with the lid velocity and the distance is normalized with the dimension of the square cavity. The governing equations can be rewritten as

$$\frac{\partial}{\partial \overline{x_i}}(\overline{u_j}\ \overline{u_i}) = -\frac{\partial \overline{p}}{\partial \overline{x}} + \frac{1}{Re}\frac{\partial}{\partial \overline{x_i}}(\frac{\partial \overline{u_j}}{\partial \overline{x_i}}) \qquad 4.03$$

The normalized variables are

$$\overline{x_i} = \frac{x}{D} \qquad \overline{u_i} = \frac{u_i}{V} \qquad \overline{p} = \frac{p}{\rho V^2} \qquad 4.04$$

The lid velocity , density of fluid and dimension of cavity are all set to unity. Therefore, the viscosity is the scaling parameter for the flow field.

At low Reynolds numbers a central recirculation zone is present, but as the Reynolds number is increased secondary recirculation zones develop. At a Reynolds number of 100 one secondary recirculation zone forms in addition to the central recirculation zone. An additional secondary vortex appears in the left-hand corner when the Reynolds number reaches 400. A third secondary vortex appears in the upper left hand

corner when the Reynolds number reaches 1000(Fig.4.01 b). The solution by Burgraff(1966) at a Reynolds number of 400, using a stream function-vorticity formulation and central differencing scheme is compared to the present scheme.

4.1.1 Grid and Boundary Condition

Three different types of grids are used to solve the problem(Fig. 4.02 a,b,c). The first type used is a uniform Cartesian grid. The second grid is a non-orthogonal grid in which the grid lines intersect at angles other than 90 degrees. The third grid is a non-uniform expanding and contracting grid with higher grid density near walls and corners. The grid size was fixed at 31x31 for all three types. For the top wall a constant velocity is specified and for side walls no-slip condition is specified. The iteration was carried out until the sum of residuals of each velocity components and the sum of mass residuals decreased to $1x10^{-5}$.

4.1.2 Results and Discussions

The first two grid types are used to solve the problem at a Reynolds number of 400 and the results at the vertical centreline are compared with the solution of Burgraff(1966). The third grid type was used to study the qualitative details of flow field at the higher Reynolds number of 3200.

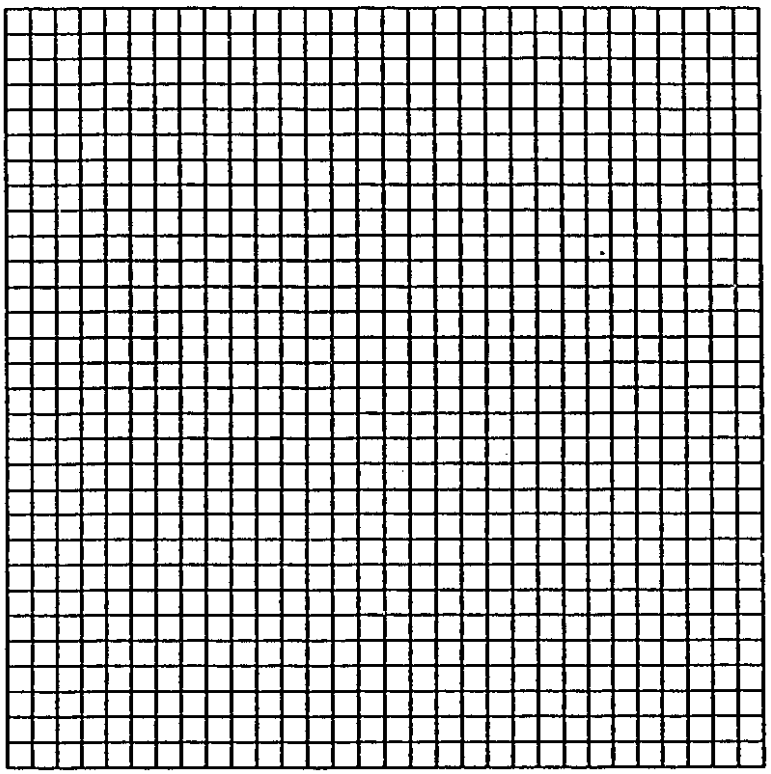

Fig. 4.02a: Driven cavity grid, Cartesian

31x31

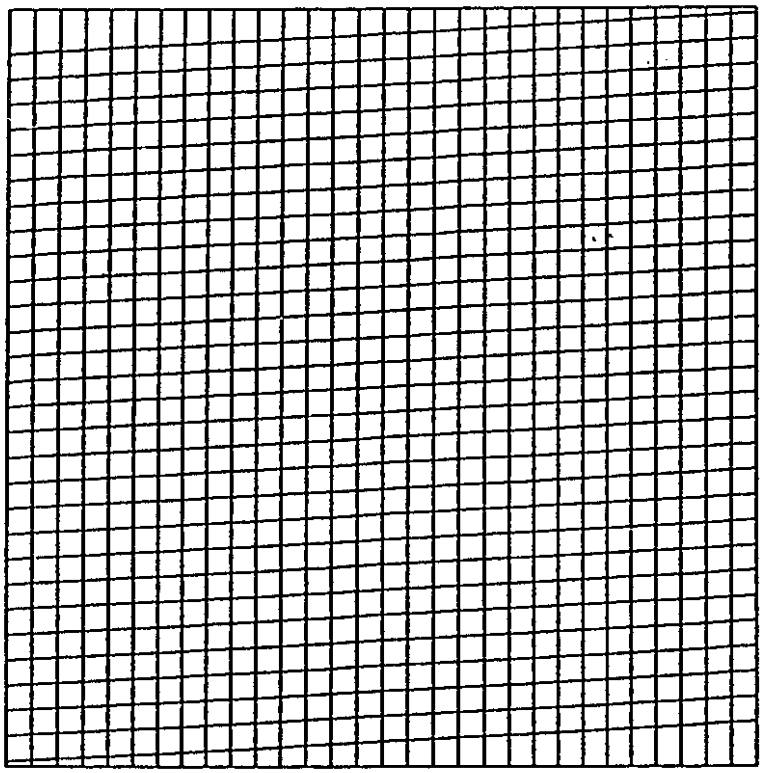

Fig.4.02 b: Driven cavity grid, non-orthogonal,

31x31

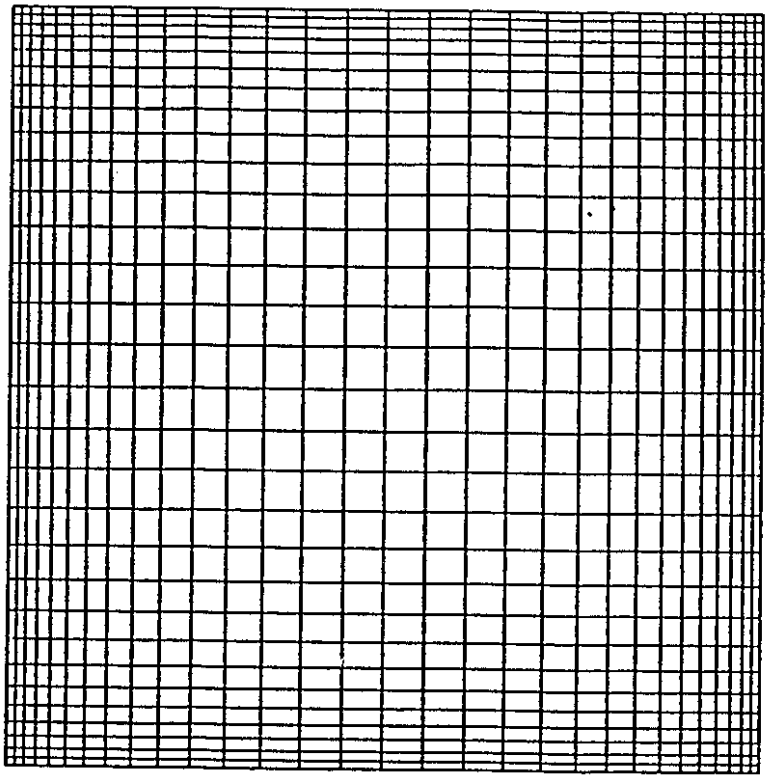

Fig. 4.02 c: Driven cavity grid, non-uniform

31x31

The vertical centerline(Fig. 4.01 line ab) u-velocity comparison is given in Fig.4.03. The result obtained with the first-order upwinding scheme shows poor agreement with the Burgraff's results. The false diffusion error causes the profile obtained using the first-order upwinding to be less steep. The second-order upwinding results are in good agreement with Burgraff. The non-orthogonal, skewed grid results differ only slightly from the orthogonal Cartesian grid result.

The difference between the orthogonal grid result and non-orthogonal grid result is attributed to truncation errors due to the non-orthogonality. Additional discretization error arises when the grid is non-orthogonal[Thompson et al.(1985)].

The velocity vector plot for a Reynolds number of 3200 is given in Fig.4.04. The result is obtained with second-order upwinding. Street and Meakin(1988) used a 41x41 grid to compute the same flow field and also obtained four vortices. If a first-order discretization scheme is used, the vortex in the upper left-hand corner may not appear[De Vahl Davis and Mallison(1976)]. The stream function contours plots are given in Fig.4.05 and the pressure contours are given in Fig.4.06. The results are nearly identical to the results obtained by Kim(1988) in which a quadratic finite element method was used obtain the solution.

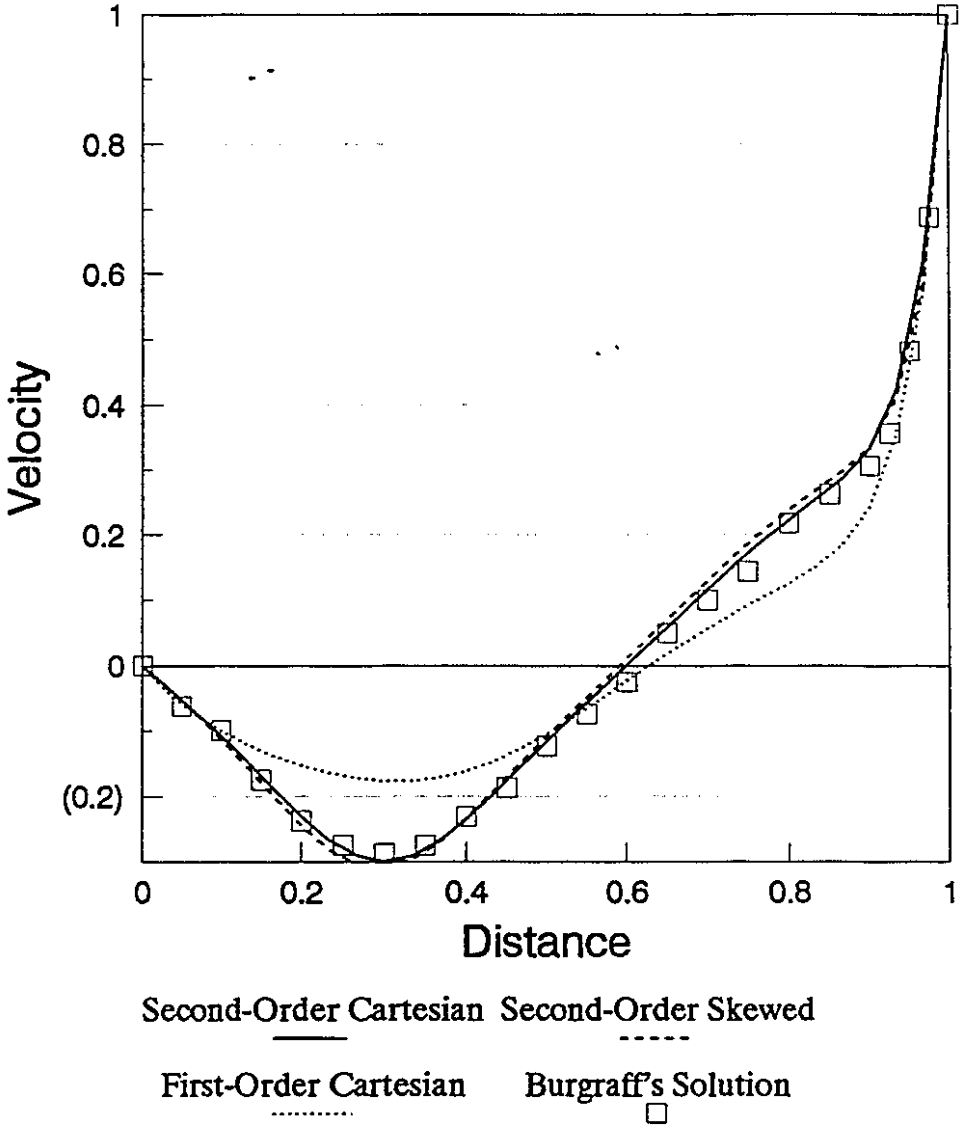

Fig. 4.03: Driven cavity centerline u- velocity comparison, Re=400

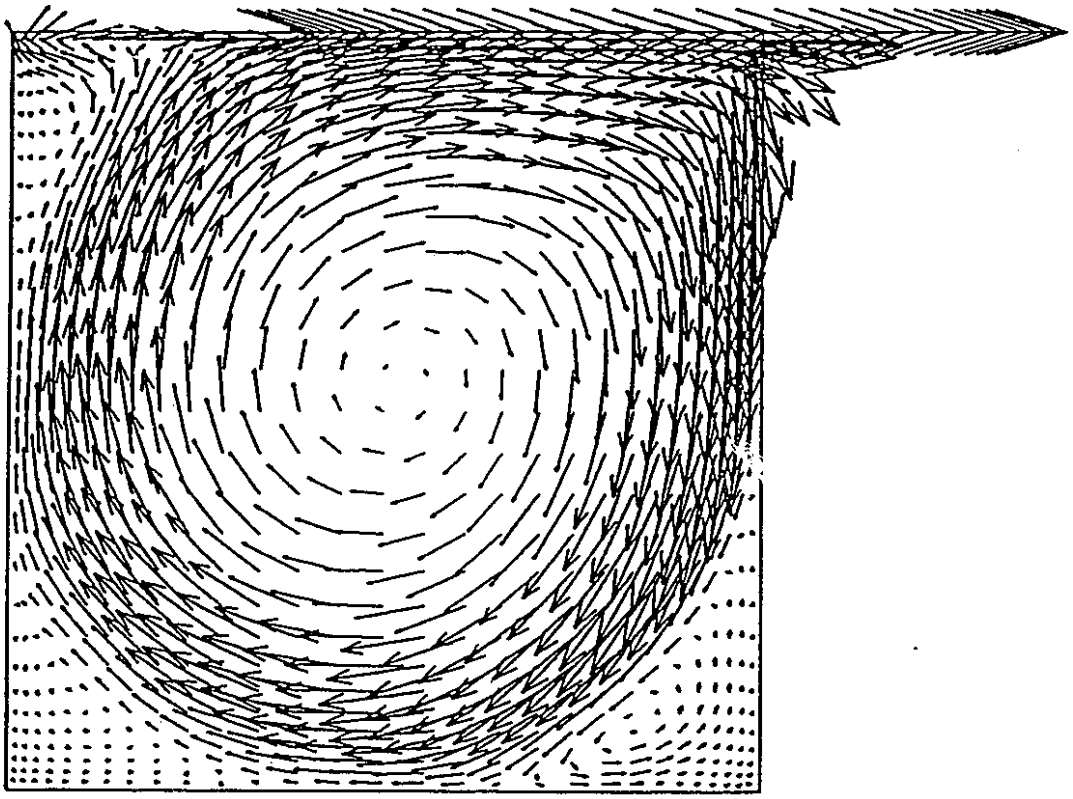

Fig. 4.04: Driven cavity velocity vector plot , Re=3200

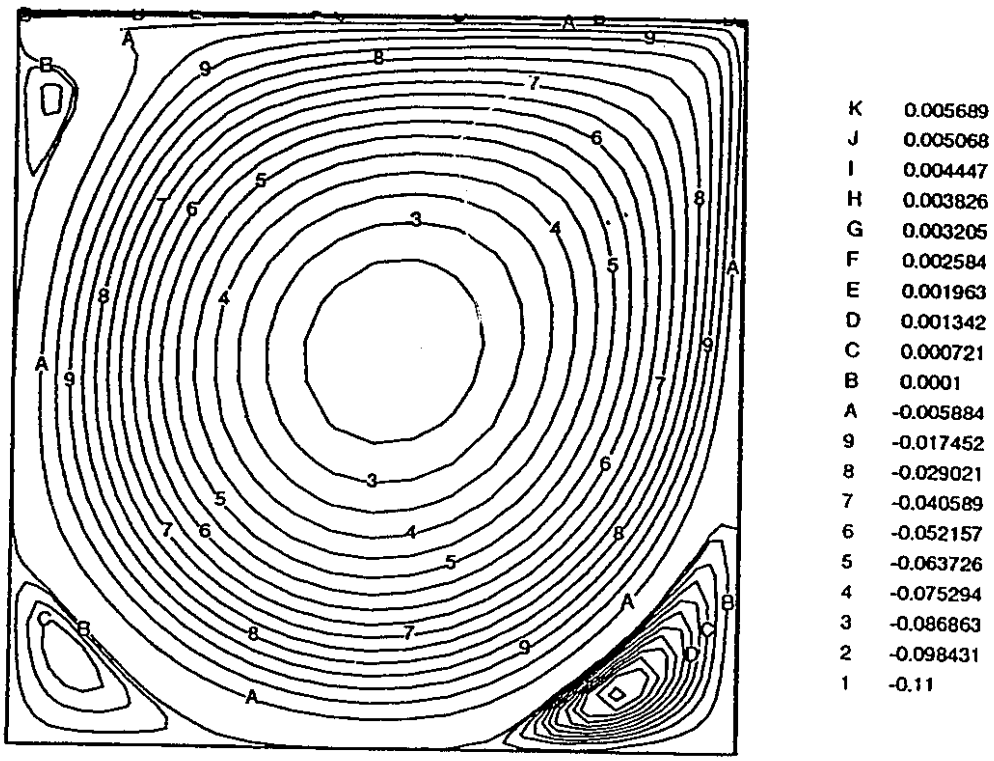

K	0.005689
J	0.005068
I	0.004447
H	0.003826
G	0.003205
F	0.002584
E	0.001963
D	0.001342
C	0.000721
B	0.0001
A	-0.005884
9	-0.017452
8	-0.029021
7	-0.040589
6	-0.052157
5	-0.063726
4	-0.075294
3	-0.086863
2	-0.098431
1	-0.11

Fig.4.05 Driven cavity stream function contour plot, Re=3200

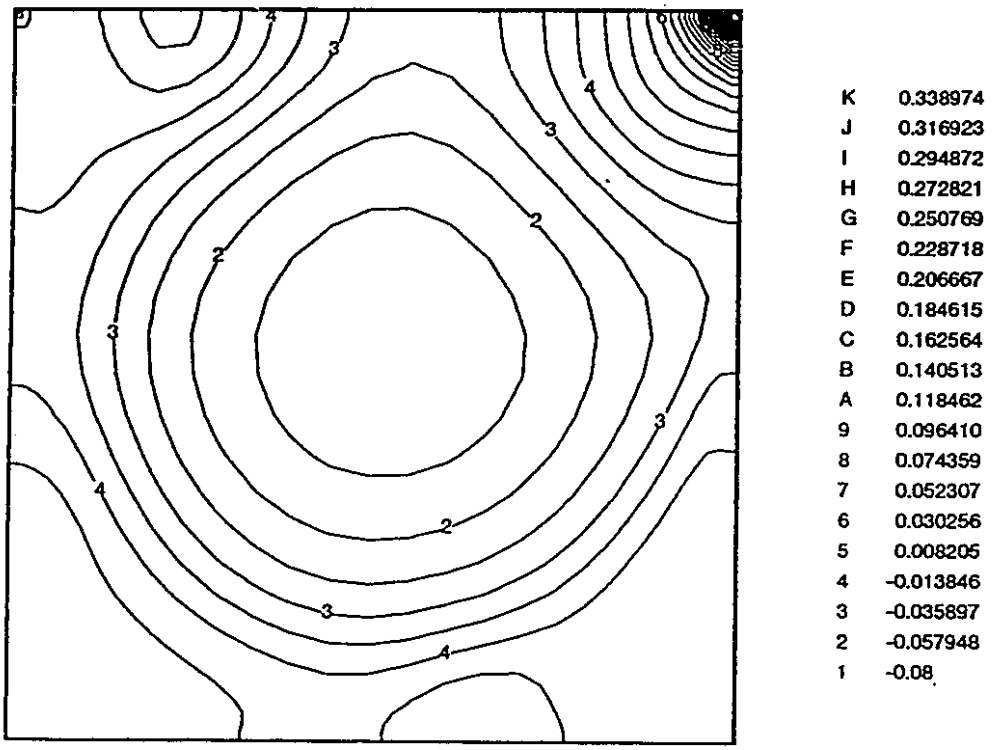

Fig. 4.06 : Driven cavity pressure contour plot, Re=3200

4.2 Polar Cavity

The driven polar cavity was studied numerically and experimentally by Fuchs and Tillmark(1985) and Fuchs(1985). The experimental appratus consisted of an inner cylindrical surface, straight side walls, and a section of another cylinder with a larger radius. The inner cylinder rotated at a constant angular velocity(Fig. 4.07). Fuchs and Tillmark(1985) used Laser Dopper Anemometry to measure velocities at various points inside the cavity and the multigrid algorithm to solve the problem numerically. The multigrid solution algorithm which uses the solution from the coarse grid as the initial condtion for the solution at the fine grid was used. Second-order central differencing was used for both convection and diffusion terms. Their solution using a 80x80 grid gave results which matched the L.D.A. data.

4.2.1. Grid and Boundary Condition

The polar cavity grid is displayed in Fig. 4.08. A 39x39 non-uniform curvilinear grid is used. The grid is finer near the walls and corners. The boundary conditions imposed are similar to the previous problem. The inner wall moves at a constant angular velocity and the other walls are stationary. The Reynolds number of the flow based on the length of the bottom wall is 350.

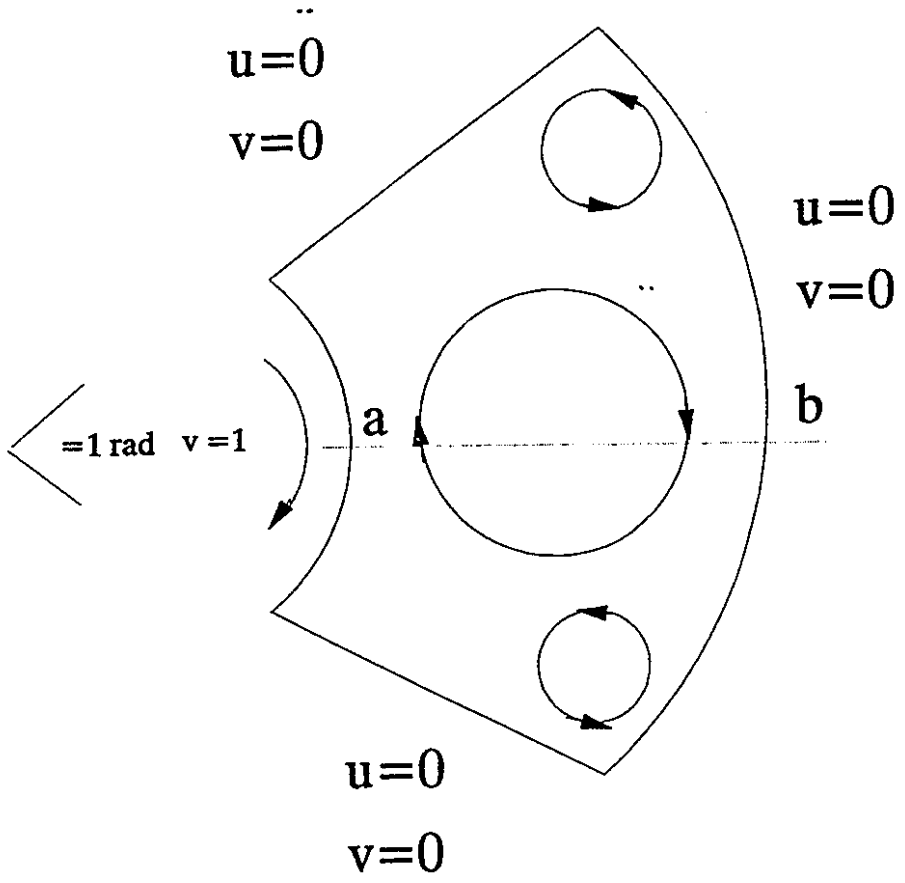

Fig. 4.07: Driven polar cavity, **Re=350**

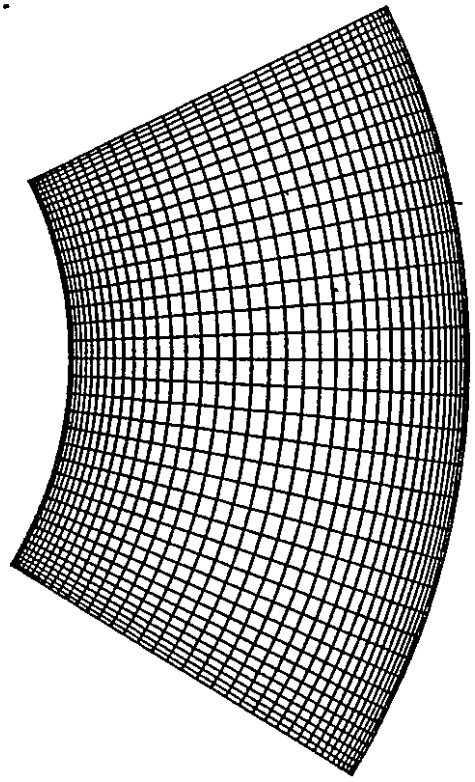

Fig. 4.08: Driven polar cavity grid

4.2.2 Results and Discussions

The horizontal centreline(line ab in Fig 4.07) u-velocity calculated is compared with the L.D.A. measurements from Fuchs and Tillmark(Fig. 4.09). The plot shows that the calculated results agree closely with the L.D.A. measurements. The numerical results of Fuchs and Tillmarks using 80x80 mesh gave results which are nearly identical to the numerical predictions of this work. The equally accurate results at a lower grid density than the scheme of Fuchs and Tillmark(1985) is probably due to the use of a fine grid near the walls and corners of the cavity and the conservative formulation of the primitive variables in this study. The method used by Fuchs and Tillmark was non-conservative stream-function vorticity formulation. As discussed earlier in Chapter 2, the conservative formulation is more accurate. The velocity vector plot given in Fig. 4.10 shows three distinct recirculation zones

4.3 90-Degree Bend Square Duct

Humphrey et al.(1977) carried out a detailed experimental analysis of laminar flow in a 90-degree bend(Fig. 4.11). Their velocity measurements will be compared with the numerical predictions of this study. Numerical comparisons to theses experiments have also been made by Humphrey et al.(1977) and Rhie (1985), who used 60x15x10 and 50x22x15 grids respectively. The Reynolds number of the flow, based on the hydraulic diameter, was 790. The Dean number was $De=Re(d/2R_c)^{1/2}=368$ where d is the hydraulic

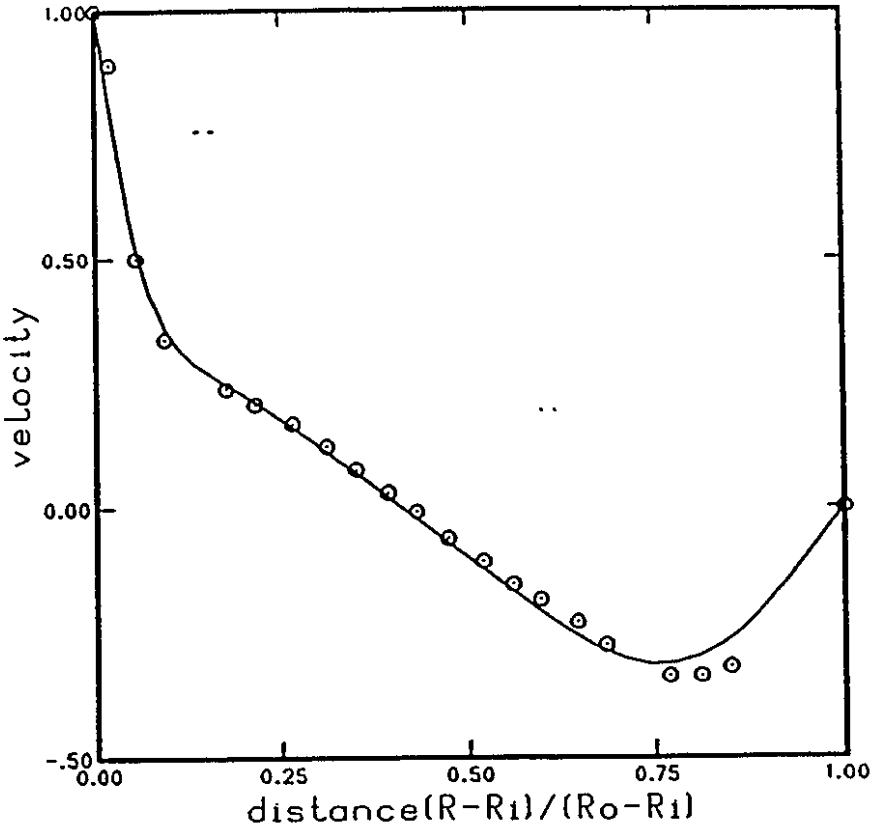

Fig. 4.09 : Polar cavity horizontal centerline u-velocity

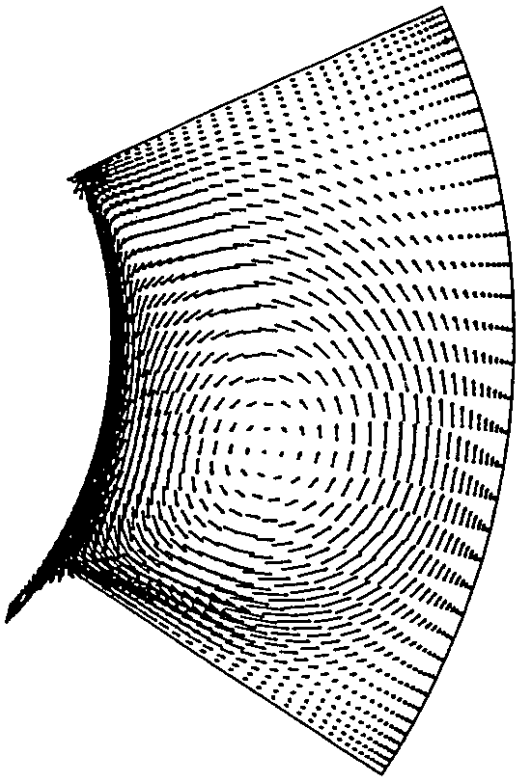

Fig. 4.10 : Polar cavity velocity vector plot

diameter and R_c is the mean radius of curvature. The longitudinal velocities were measured using a laser dopper anemometer, but the other velocity components were not measured.

At x=-5,(5 hydraulic diameters before the bend) a fully developed velocity profile was observed by Humphrey et al.(1977). As the fluid travelled through the bend, there was an acceleration towards the outer radius wall and deceleration near the inner radius wall. A small longitudinal recirculation was observed immediately into the bend, near the outer corner of the duct. The secondary flow pattern was not expermentally investigated; only numerical results were given. Numerical results on the 90-degree plane showed the presence of two counter-rotating vortices, each filling half of the plane.

4.3.1 Grid and Boundary Condition

In this work, the presence of a symmetry plane is taken into consideration and only half of the domain is discretized. The boundary conditions are:

at the inlet(x=-5): U,V,W= fully developed laminar profile

at the walls: U,V,W=0.0

at the symmetry plane(z=0) : $\frac{\partial U}{\partial \Gamma}=0.0$, $\frac{\partial V}{\partial \Gamma}=0.0$, $W=0.0$

at the exit(y=10) : $\frac{\partial U}{\partial \epsilon}=0.0$, $\frac{\partial V}{\partial \epsilon}=0.0$, $\frac{\partial W}{\partial \epsilon}=0.0$

The grid used is shown in Fig.4.12. The problem is first solved using a 40x17x11($\epsilon x \eta x \Gamma$) grid. The grid is then refined to 61x23x17 and 70x25x19. The

results from the intermediate grid are presented. The highest and lowest grid densities are used to study the grid density dependence.

4.3.2 Results and Discussions

Three different methods of discretiztion of the convection terms are used to solve the problem. The numerical results at the 90 degree and 60 degree planes are plotted in Figures 4.13 and 4.14 for the 61x21x17 grid with the experimental results of Humphrey et. al(1977). At the 90 degree and 60 degree planes the first-order upwinding method results are consistent with the previous work, i.e., the velocity profiles were not as steep as the data and the peak velocities were consistently under-predicted[Humphrey et al.(1977) and Rhie(1985)]. The results obtained with the higher order methods are in excellent agreement with the observed experimental values at the 90 degree planes(Fig 4.13a). The higher-order methods under-predict the velocity in the symmetry line at the 60 degree plane(Fig 4.14a). The experimental results show a sharp rise in the velocity profile indicating that a finer grid is needed near the wall.

The weak longitudinal recirculation zone, which was observed experimentally, is also determined numerically with all three discretization schemes. The streamwise velocity vector plot is given in Fig. 4.15 for the QUICK scheme.

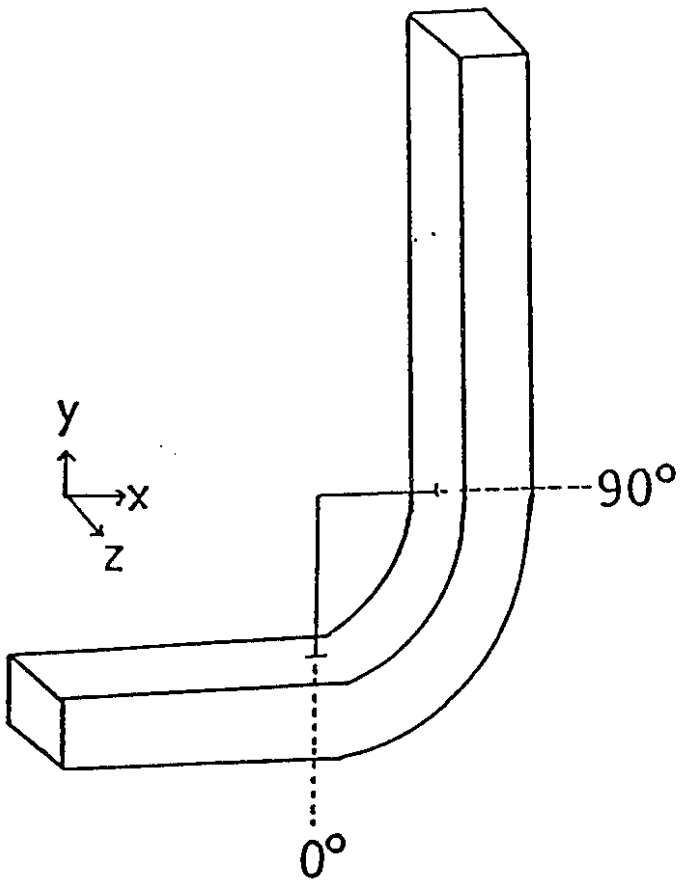

Fig. 4.11: 90-degree bend duct

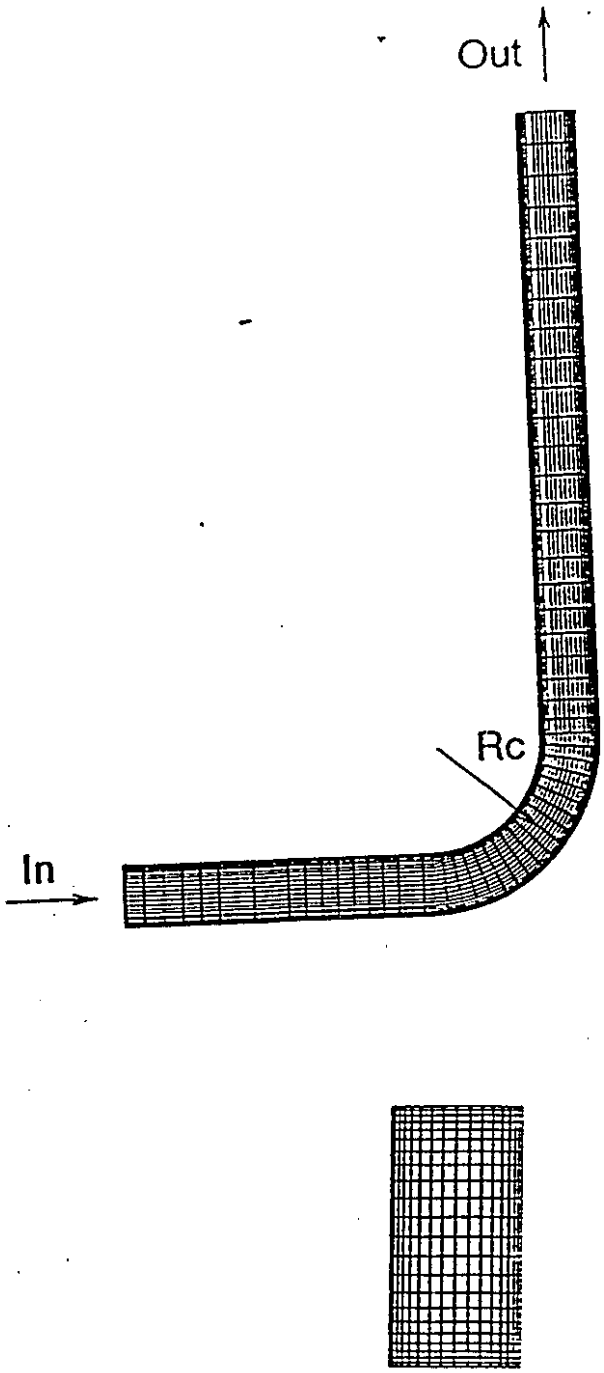

Fig. 4.12: 90-degree bend duct grid

In Fig. 4.16 the vector plots of the secondary flow in the 90-degree plane are given. The upwinding results indicate the presence of one vortex, while the higher-order schemes indicate a cellular-type flow pattern with weak secondary vortices. The first-order upwinding result is consistent with other published results[Humphrey et al.(1977), Rhie(1985)]. The higher-order upwinding results indicate a more complicated flow pattern which is consistent with the phenomenon first studied by Dean(1927). If a critical Dean number(which indicates the ratio of the curvature effect to the viscous effect) is exceeded, the secondary flow is unstable and results in the development of a second, stable laminar flow pattern which consists of several vortices superimposed on the main flow[Nandakumar and Masiliyah(1986)]. This phenomenon was observed by Cheng et al.(1977) using flow visualization studies which showed complex flow patterns at high De numbers.

In Fig.4.17 the effect of grid refinement for the three schemes is shown at the 90 degree symmetry plane. The first-order upwinding scheme solution is not grid-independent and changes significantly as the grid is refined. The higher-order upwinding scheme solution at the lowest grid density are very similar to those at the highest grid density and the 61x23x17 grid shows near grid independence of the solution. It is difficult to achieve total grid independence, especially with highly convected flows in 3-D.

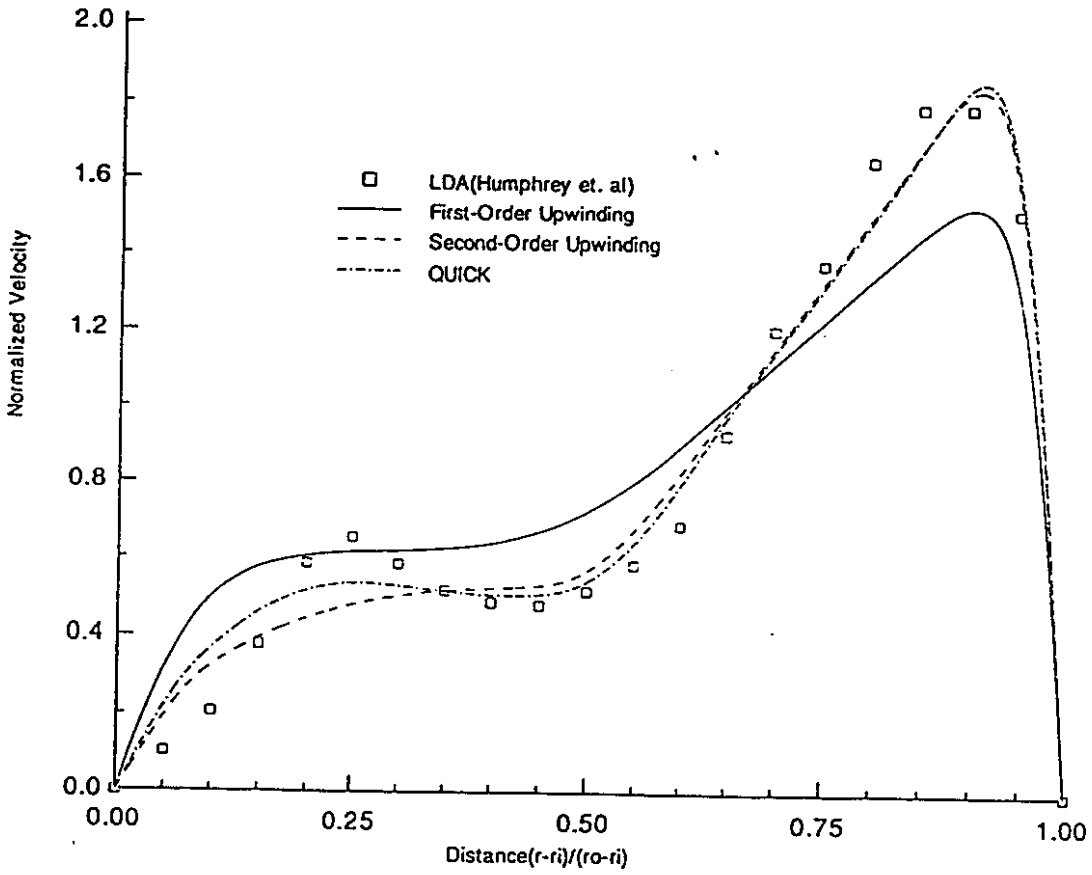

Fig. 4.13a : Comparison of results at the 90 degree plane along the central plane within the duct

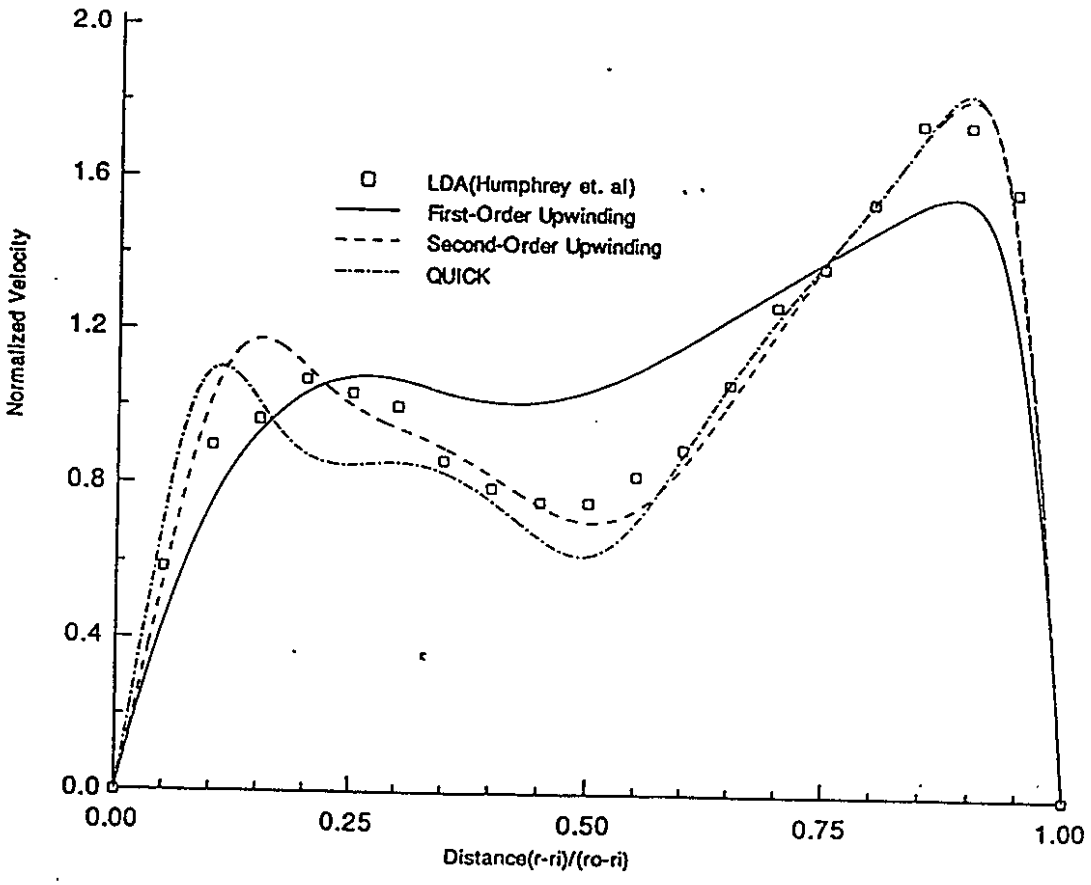

Fig. 4.13b: Comparison of results at the 90 degree plane along the plane halfway between the symmetry and the outside wall

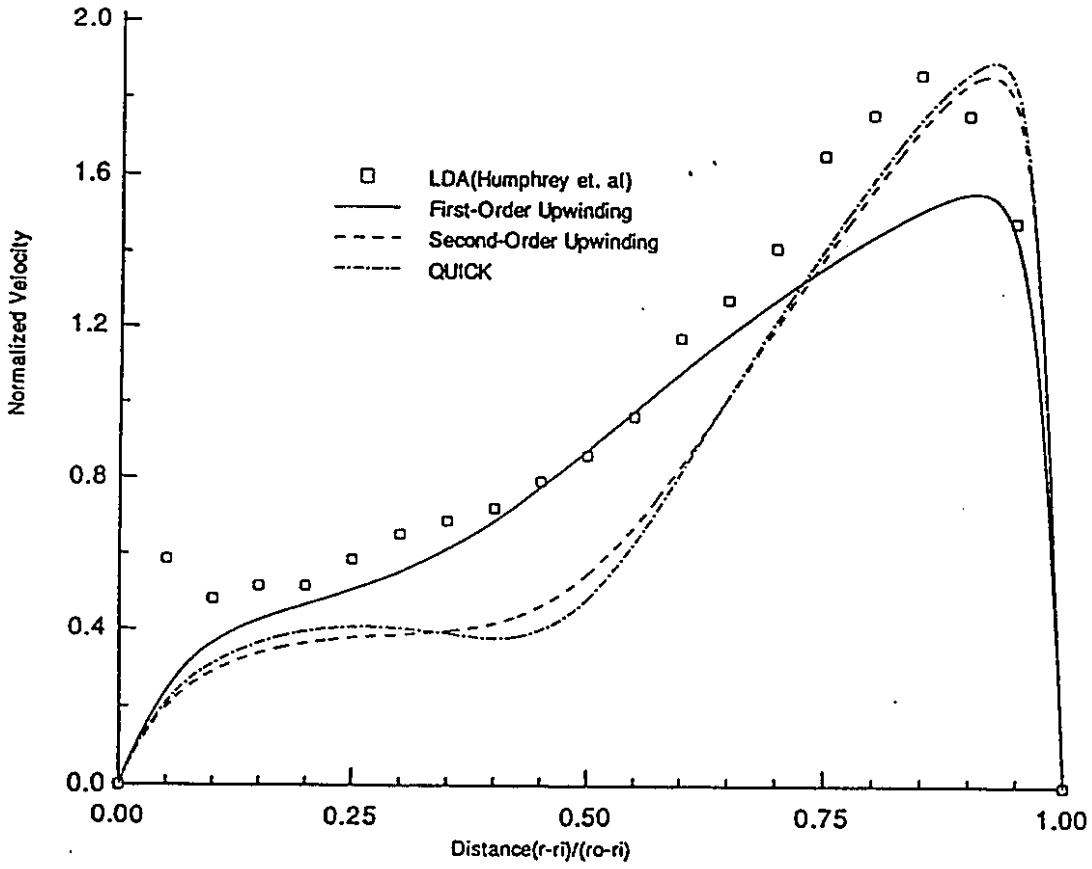

Fig. 4.14a: Comparison of results at the 60 degree plane along the central symmetry plane

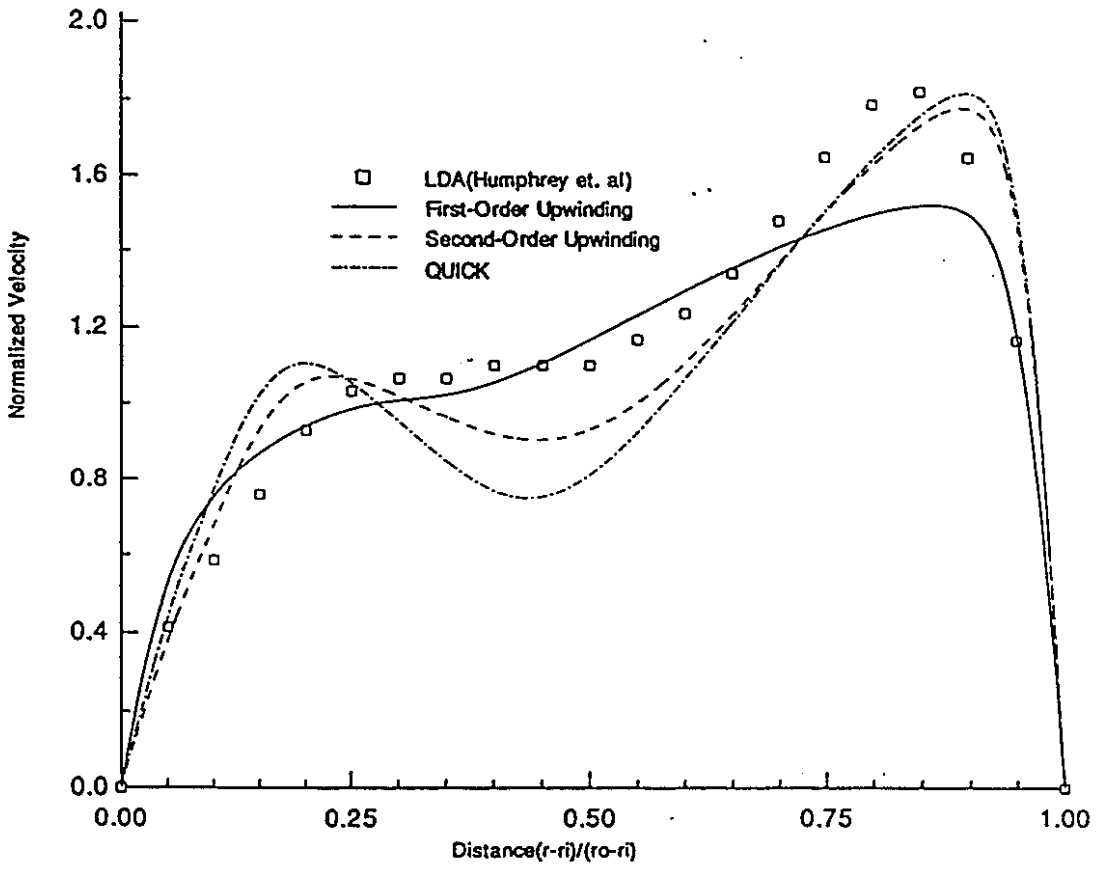

Fig.4.14 b: Comparison of results at the 60 degree plane along the plane halfway between the symmetry plane and the outside wall

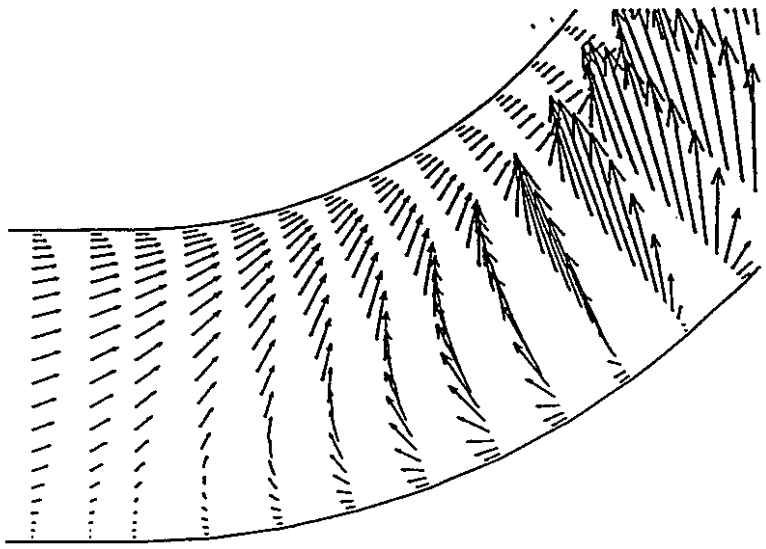

Fig. 4.15: Velocity vectors in the plane z=0.485

showing longitudinal recirculation

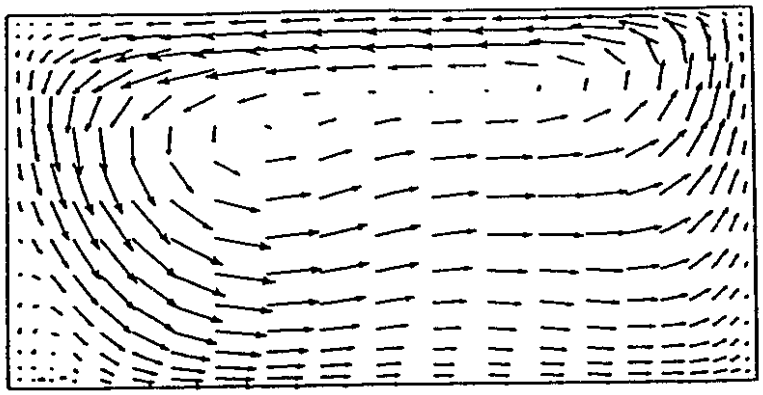

first-order

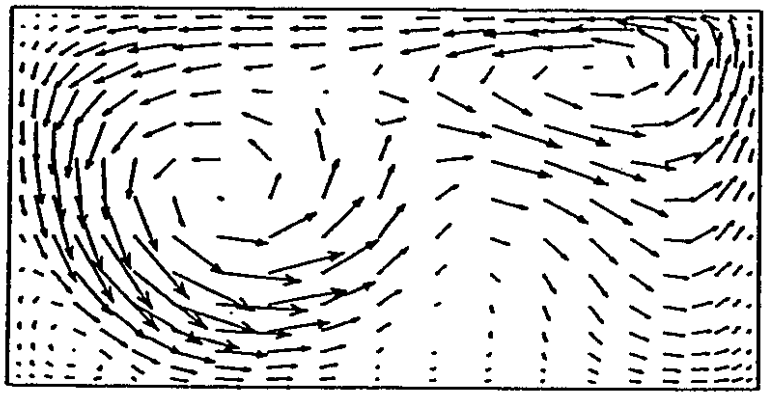

second-order

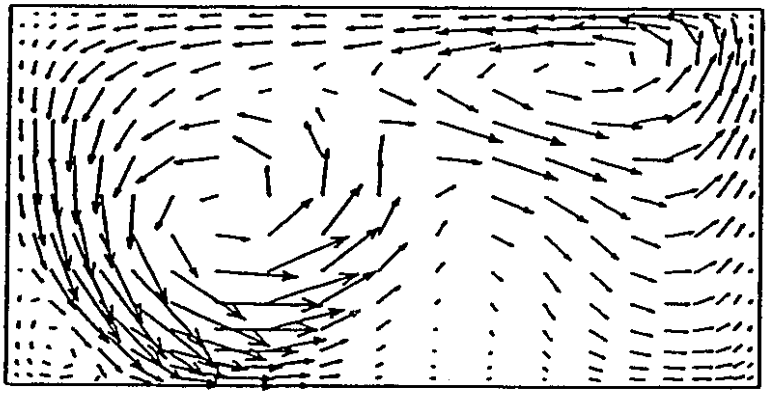

QUICK

Fig. 4.16 : Transverse vector plots at 90-degree plane

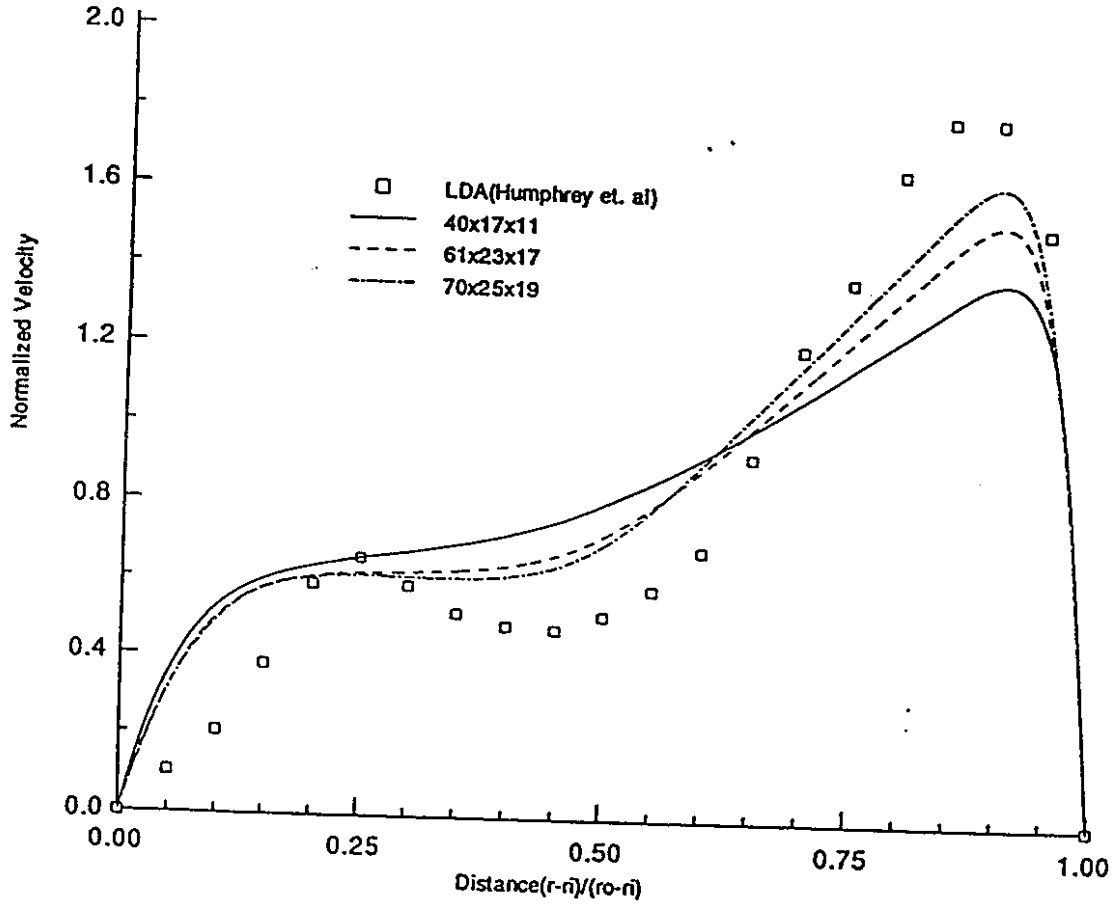

Fig. 4.17a: Effect of grid refinement in the 90 degree plane for first-order upwinding

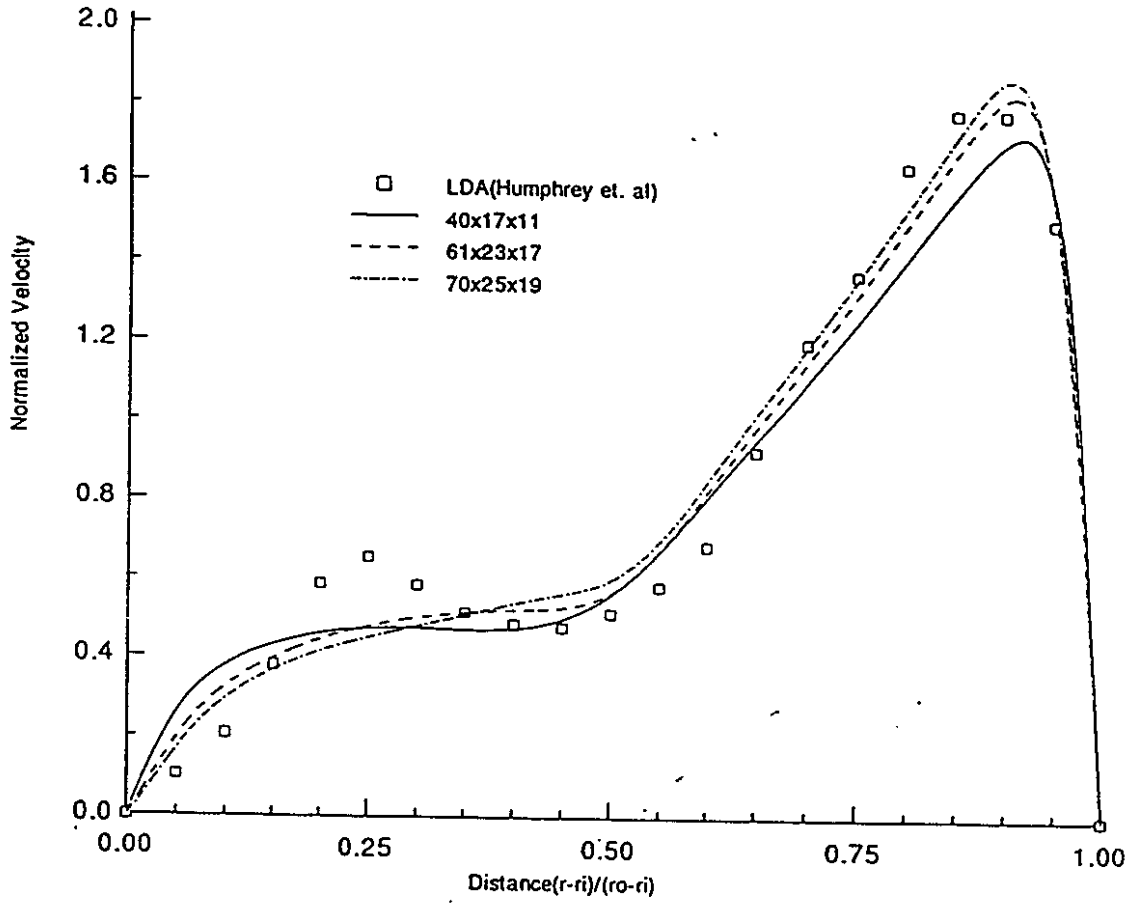

Fig. 4.17 b: Effect of grid refinement in the 90 degree plane for second-order upwinding

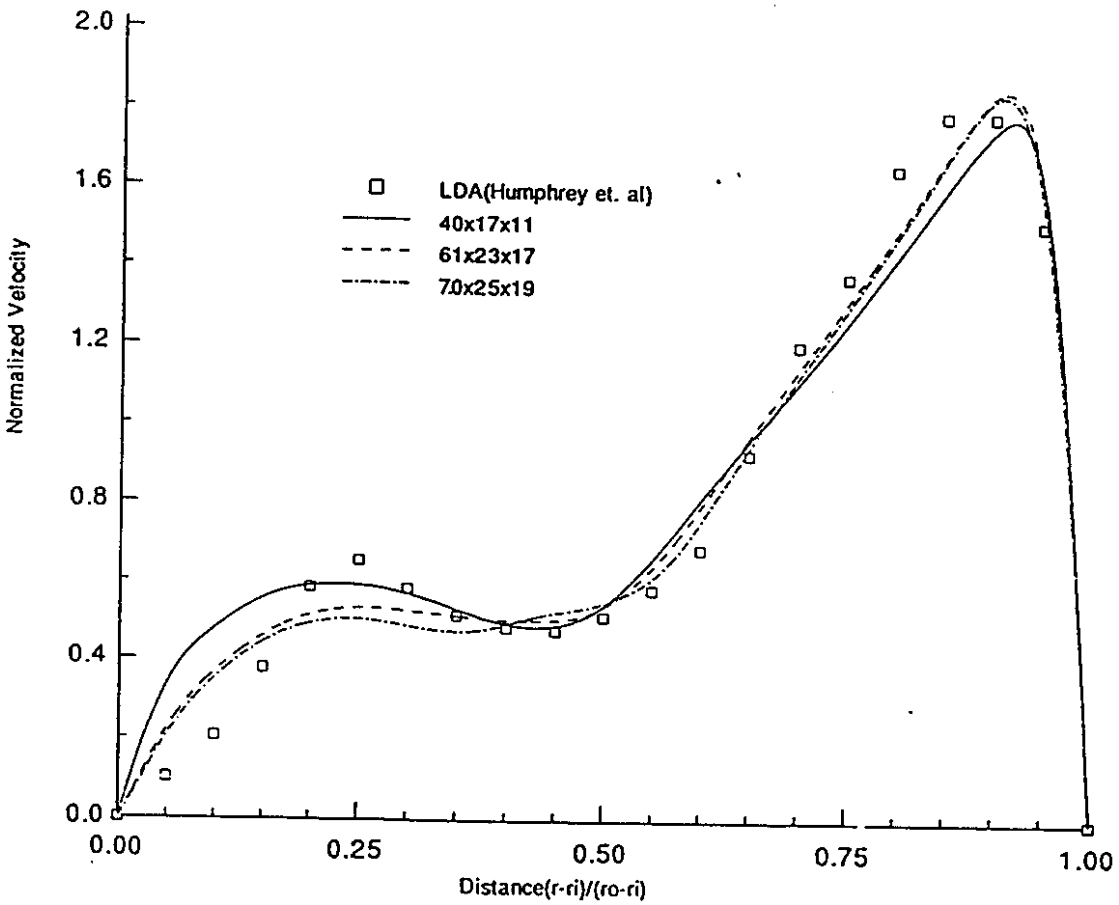

Fig. 4.17c: Effect of grid refinement for in the 90 degree plane for QUICK

PAGINATION ERROR.

TEXT COMPLETE.

ERREUR DE PAGINATION.

LE TEXTE EST COMPLET.

NATIONAL LIBRARY OF CANADA.

CANADIAN THESES SERVICE.

BIBLIOTHEQUE NATIONALE DU CANADA.

SERVICE DES THESES CANADIENNES.

5. Steady State Opposed Jet Flow

Within a certain range of parameters which characterize this flow field, the flow pattern is symmetric and stationary; the variables are independent of time and only spatial dependence exits. The parameters which describe a flow system include the geometric dimensions of a system, velocity of the flow field, and the fluid properties. The parameters are expressed in dimensionless form by the Reynolds number. The experimental works indicate that the range of Reynolds numbers at which steady state exists is very narrow for jet-to-jet impingement[Lee et al.(1980), Sandell(1983)]. However, as described in Chap. 1, previous investigators present an unclear picture of the jet impingement process. In this chapter, the steady state solution of jet-to-jet impingement is investigated using the numerical method developed in the previous chapters. The steady state algorithm(time derivative of zero) is used to obtain the solution at low Reynolds numbers. In Chap. 6, the unsteady state is explored using time integration. No previous calculations of this flow field appear to have been reported. Steady, finite-element calculations of very low Reynolds number impinging jets were recently published by Schunk et al.(1990). However, they assumed that the flow was symmetric about an axis through the jets.

5.1 Grid and Boundary Conditions

The RIM mixhead geometry grid is shown in Fig. 5.01(c.f. Fig.1.04). In the axial

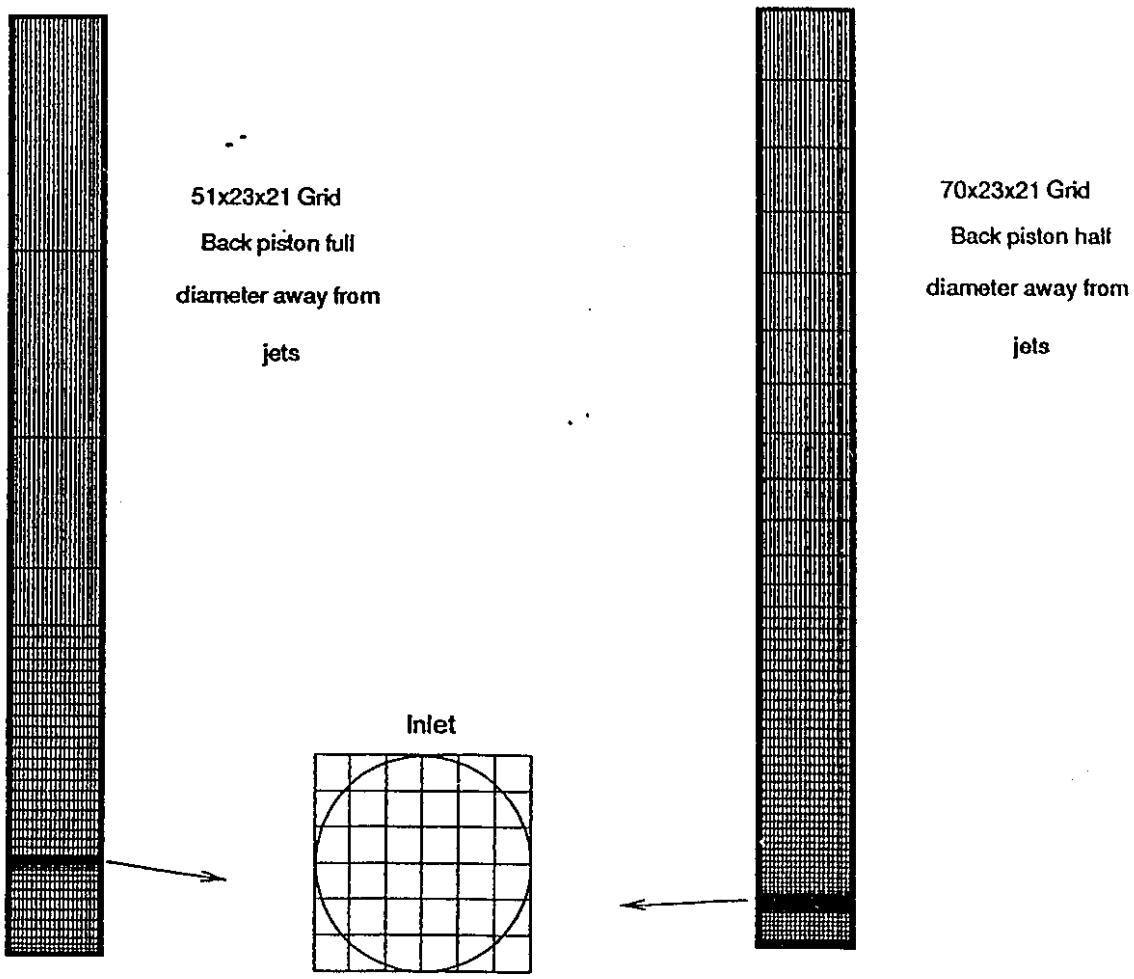

Fig. 5.01a: RIM Grid-

vertical jet impingement plane and inlet

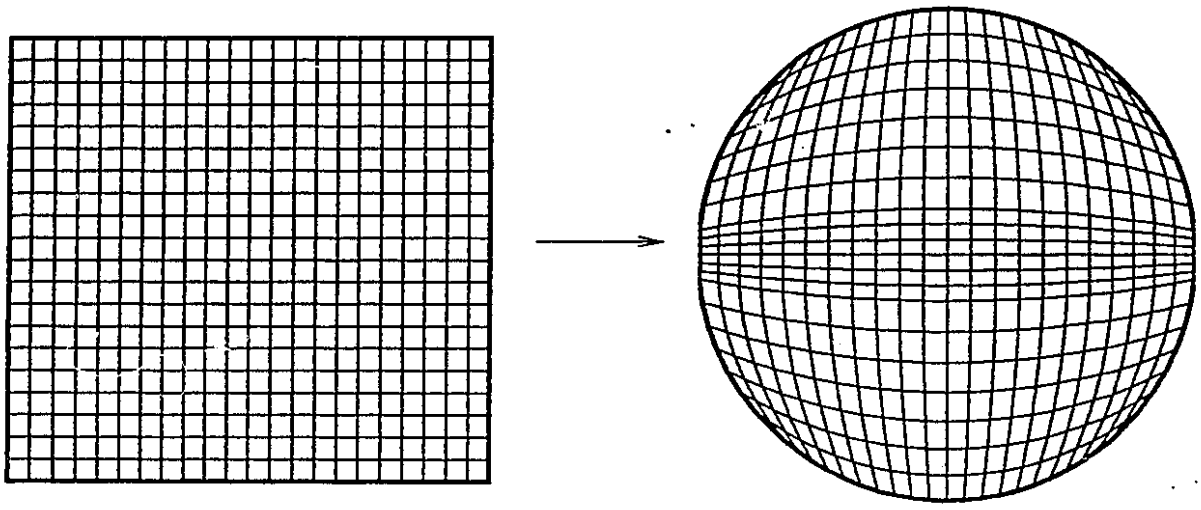

Fig.5.01b:RIM grid-

horizontal plane

direction, two grids of 51 and 70 lines are used. The cylinder is formed by transforming 23x21 rectangular computational domain into a circular physical domain using the transfinite interpolation technique[Thompson et al.(1990)]. The inlet boundary condition is specified using a 7x7 rectangular grid at the side of the cylinder. The round jet is specified using the fully developed equation for a pipe flow.

$$v=2v_{avg}(1-(\frac{r}{R})^2) \qquad 5.01$$

where V_{avg} is the average jet inlet velocity. Therefore, the round jet is specified by stepwise approximations on a rectangular grid. The no slip or zero velocity condition is specified at the wall, and for the mix-chamber outlet, the zero velocity gradient condition is specified.

The flow problems are conveniently formulated by expressing the variables in dimensionless forms. The length units are divided by the diameter of the chamber and the velocities are scaled by the average jet inlet velocity. The resulting governing equation in nondimensional form is

$$\frac{\partial}{\partial x_i}(\overline{u_i}\ \overline{u_j}) = \frac{\partial \overline{p}}{\partial x_j} + \frac{1}{Re}\frac{\partial^2 \overline{u_j}}{\partial x_i \partial x_i} \qquad 5.02$$

where

$$\overline{x_i}=\frac{x_i}{D} \qquad \overline{P}=\frac{p}{\rho V_{avg}^2} \qquad \overline{u_i}=\frac{u_i}{V_{avg}} \tag{5.03}$$

and

$$Re=\frac{u\,D}{\nu} \tag{5.04}$$

The chamber diameter(D) is set to 1 and the jet diameter(d) is set to 0.1. The distance from jets to the exit is 10D. The inlet jet Reynolds number is

$$Re_{jet}=\frac{.1\;V_{avg}}{\nu} \tag{5.05}$$

The density and average velocity are arbitrarily set to unity and the Reynolds number is adjusted by changing the viscosity. For example, to obtain the jet Reynolds number of 10 the viscosity is set to .01.

5.2 Results and Discussions

All variables were initially set to zero. The second-order upwinding method was used for the convection terms and second-order central differences were used for the diffusion terms. Iteration was continued until the convergence criterion was met. For velocities and pressure, the following convergence criterion was used at each point.

$$\left|\frac{\theta-\theta^{old}}{u_{avg}}\right|<10^{-5} \tag{5.06}$$

5.2.1 Back Piston, full diameter away from jets

The distance between the piston head and jets was set to the chamber diameter in the first set of runs and 0.5 times the chamber diameter in the second set of runs. The last result is obtained with the jets at unequal velocities.

The results for Reynolds number 10 are given in Figs. 5.02 to 5.04. In Fig. 5.02 the vector plots at four different horizontal planes are shown. In Fig.5.03 the vector plot at the vertical jet impingement plane and corresponding u-velocity contour plots are shown. At this Reynolds number the viscous terms dominate the convection terms. Small recirculation zones are present near the jet entrances. The pressure contours show the highest pressure occurs at the jet entrance(Fig.5.04).

The vector plots for the Reynolds number of 50 are given in Fig. 5.05 to 5.07. The velocity vector plots in four horizontal planes are shown in Fig.5.05. The vector and u-velocity contour plots along the vertical jet impingement plane are shown in Fig.5.06. Two connected recirculation zones form above and below the jets. The pressure contours are on the horizontal jet impingement planes are shown in Fig.5.08. The highest pressure occurs at the impingement point. The vector and pressure fields are symmetric with respect to the vertical center planes.

At a Reynolds number of 75, the recirculation zone becomes stronger(Fig.5.08 and

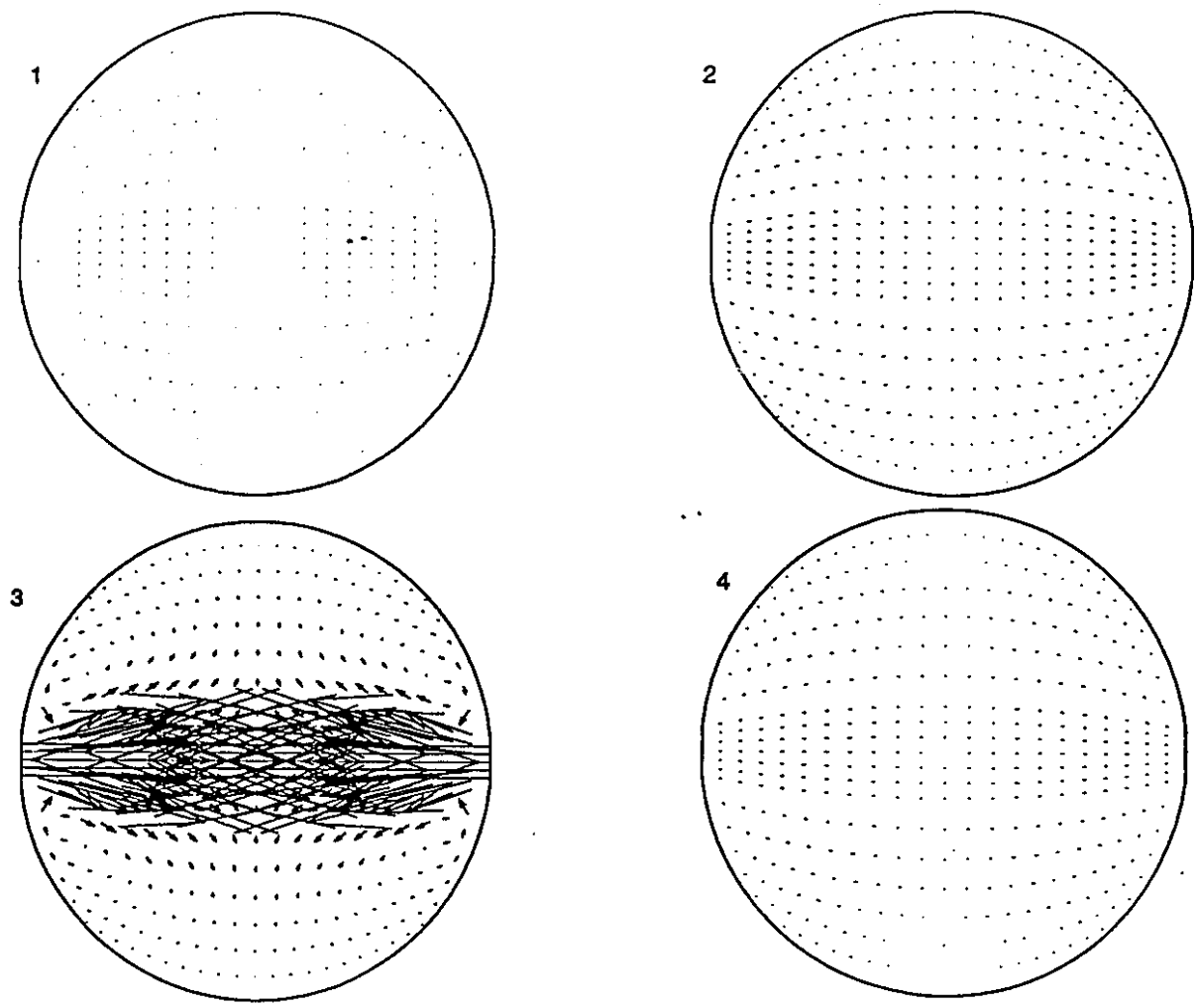

Fig.5.02: Velocity vector plots at

different horizontal planes, Re_{Jet}=10

1. 0.1775 D from bottom
2. 0.6870 D from bottom
3. 1.0000 D from bottom
4. 1.4250 D from bottom

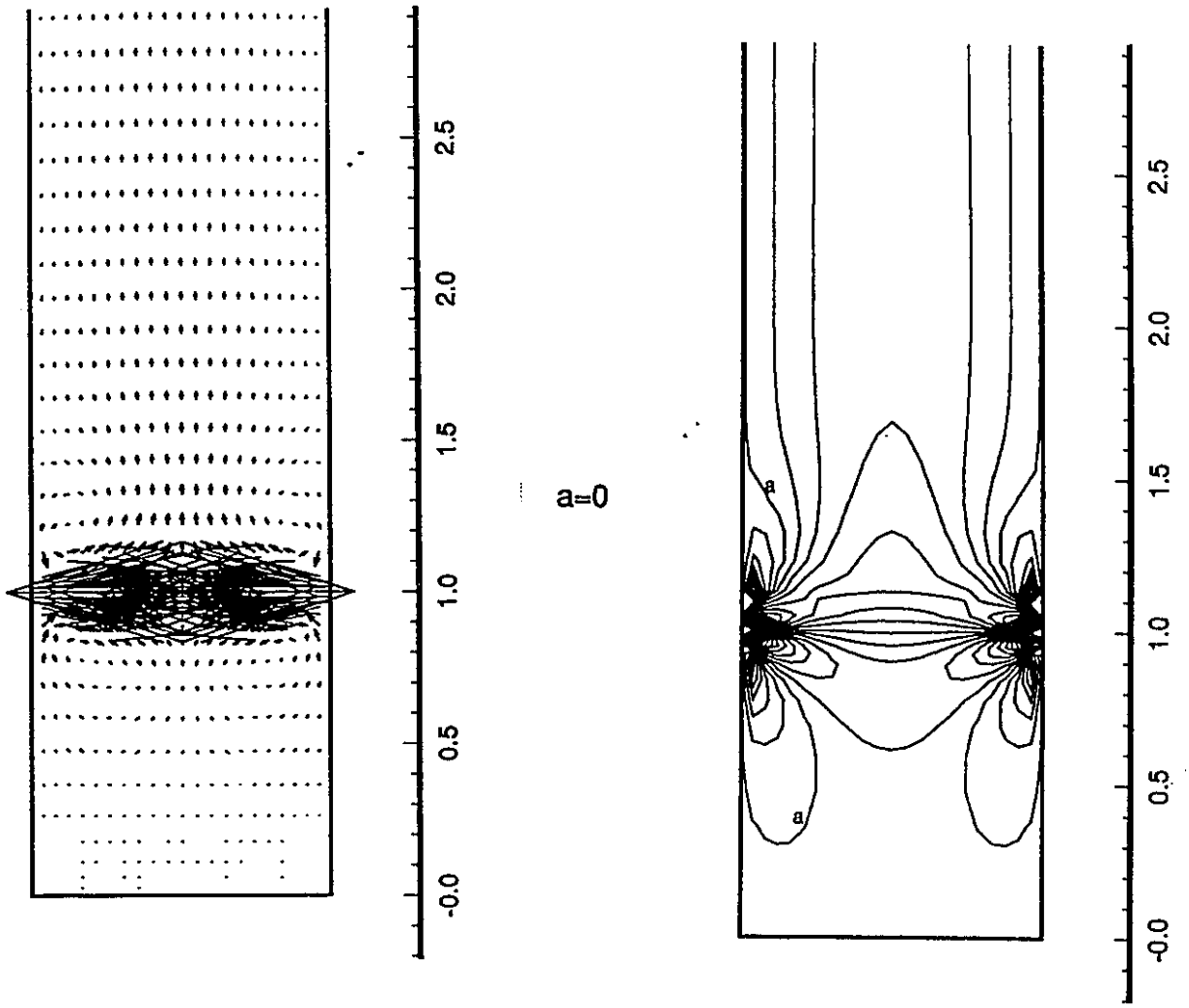

5.03: Velocity vector and U-velocity contour plots along the vertical jet impingement plane, Re_{jet}=10

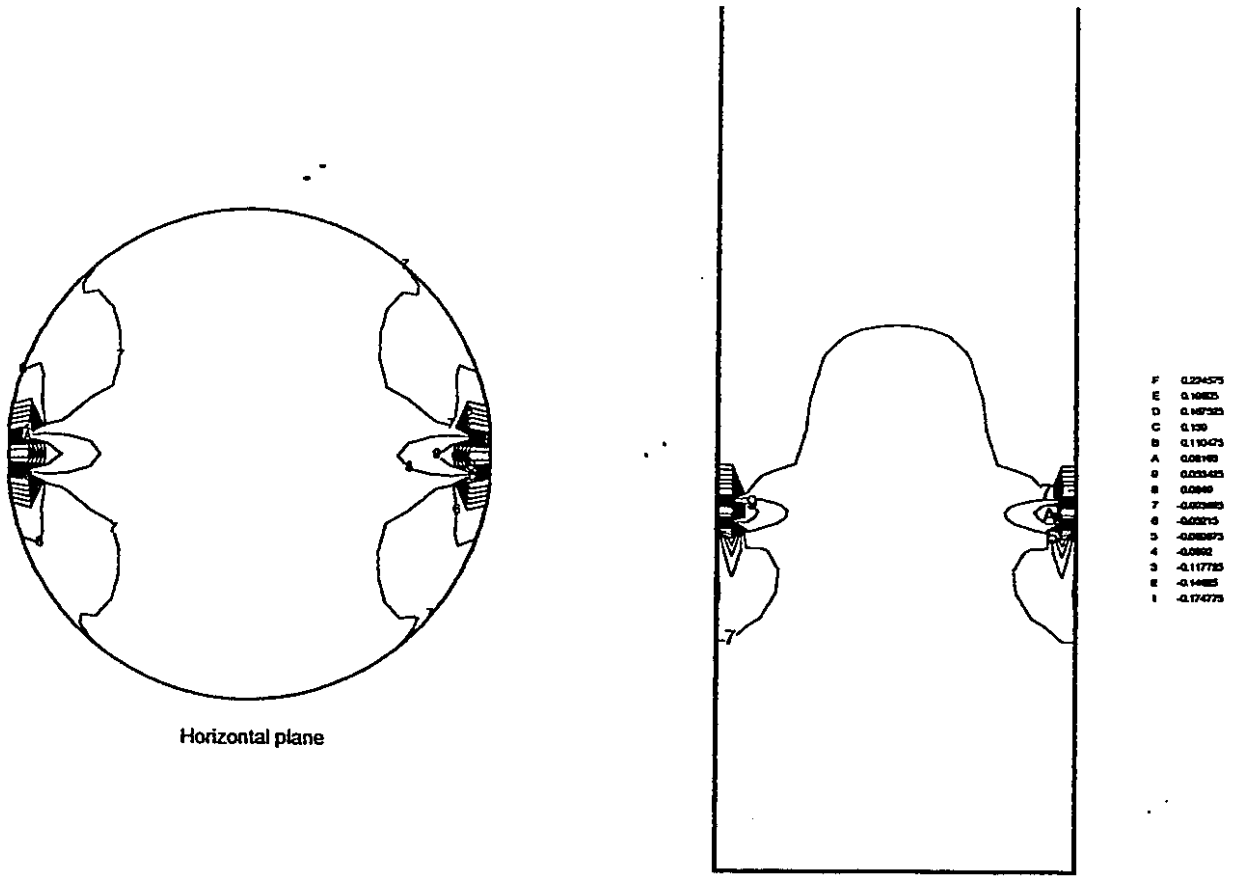

Fig.5.04: Pressure contour plots along the horizontal and vertical jet impingement planes, Re_{jet}=10

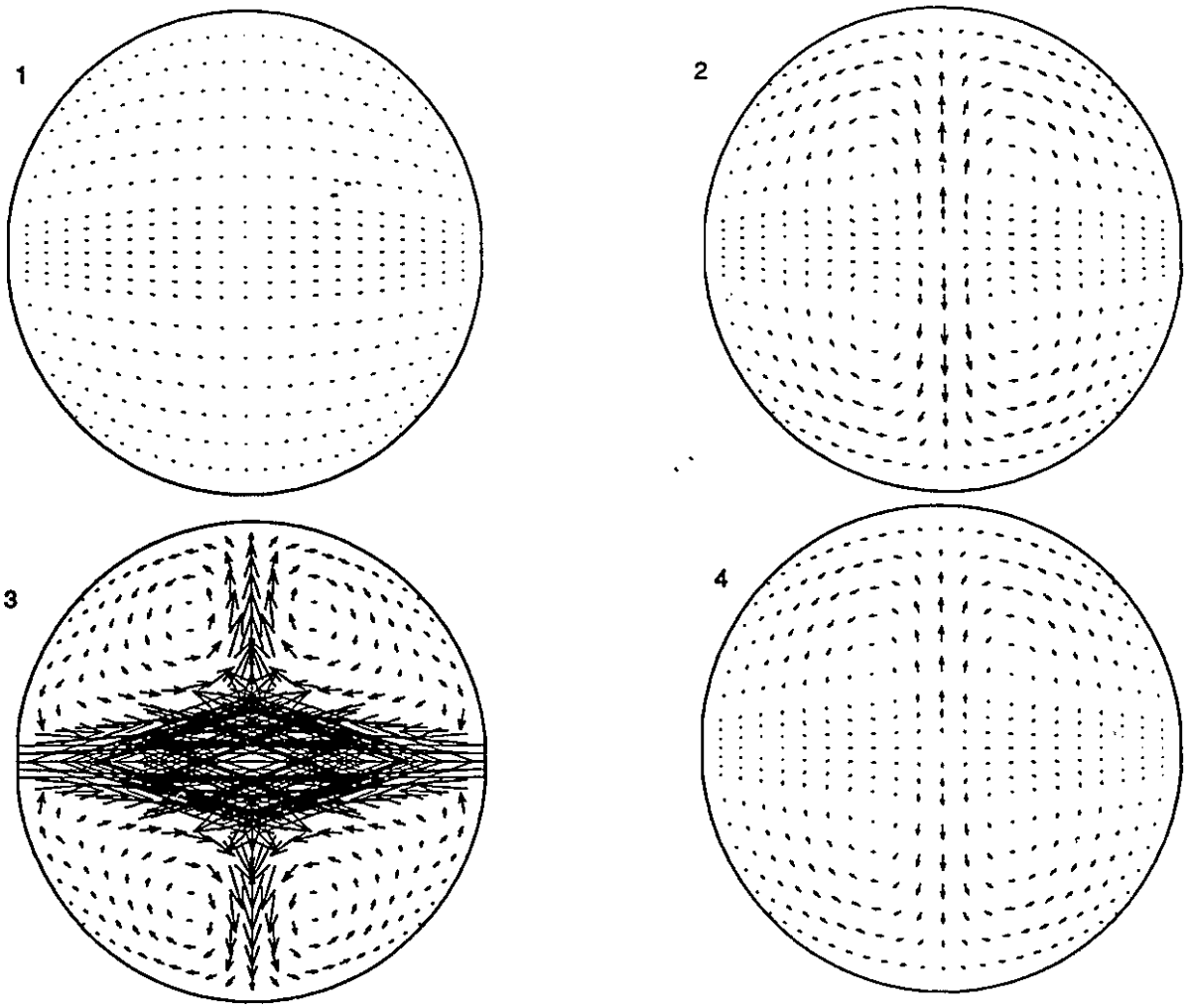

Fig.5.05: Velocity vector plots at

different horizontal planes, Re_{jet}=50

1. 0.1775 D from bottom
2. 0.6870 D from bottom
3. 1.0000 D from bottom
4. 1.4250 D from bottom

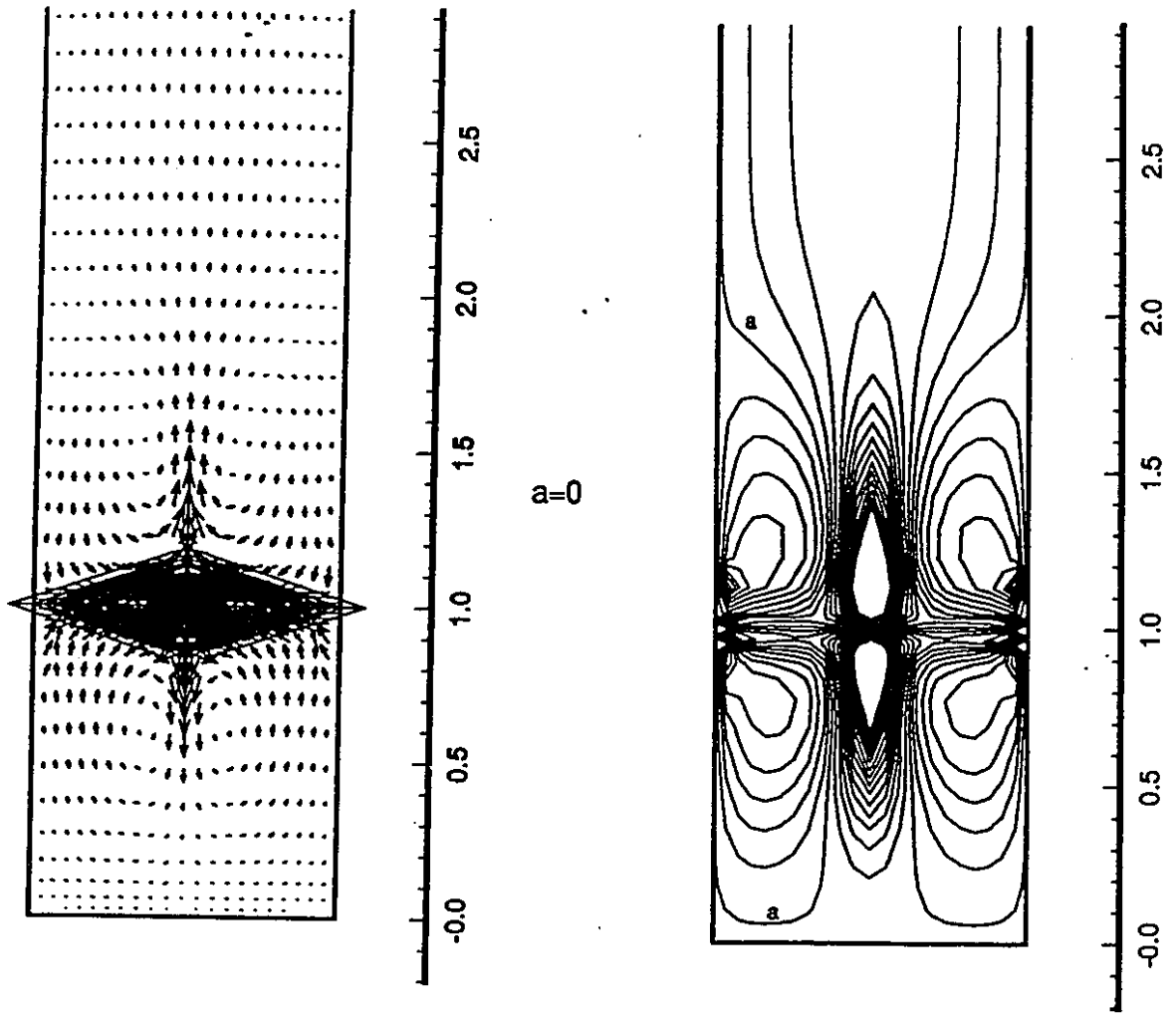

Fig.5.06: Velocity vector and u-velocity contour plots along the vertical jet impingement plane, Re_{jet}=50

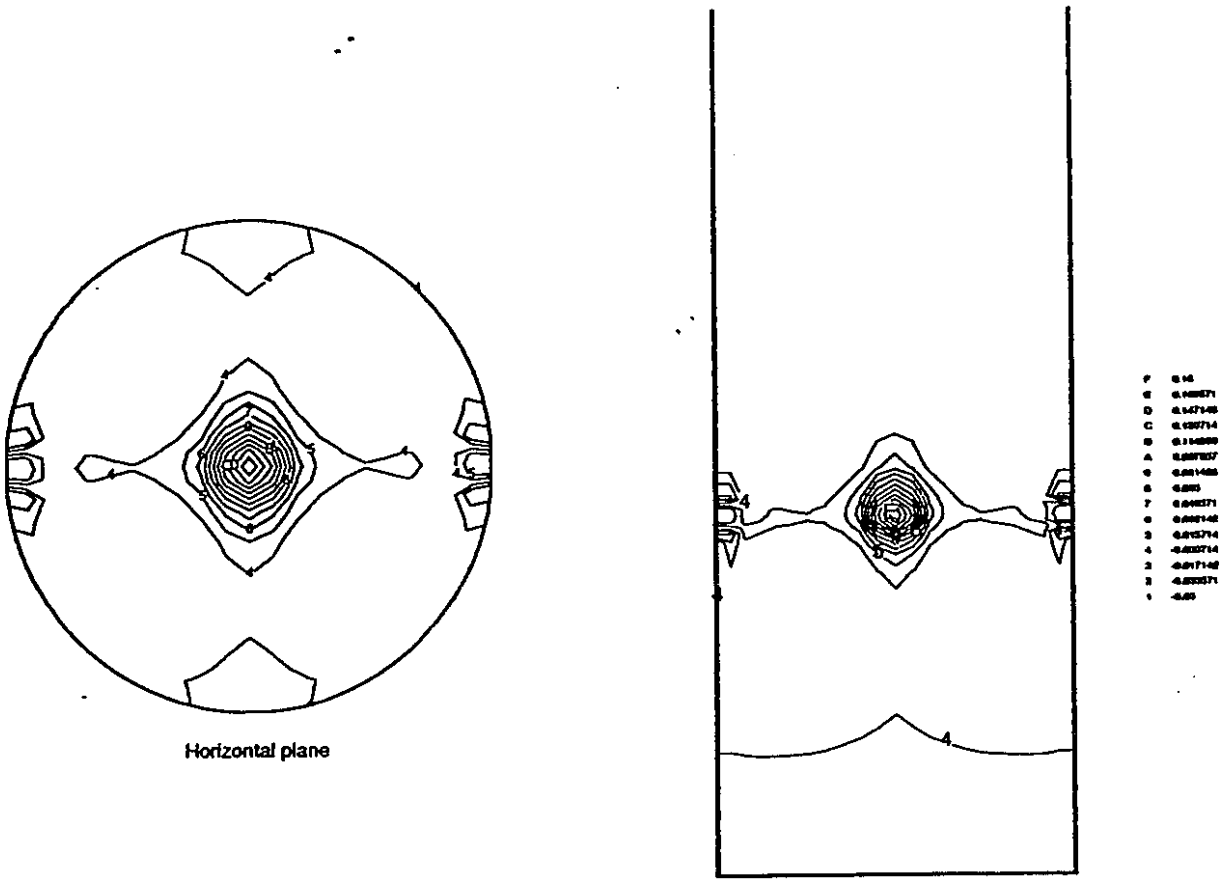

Fig.5.07: Pressure contour plots along the horizontal and vertical jet impingement planes, Re_{jet}=50

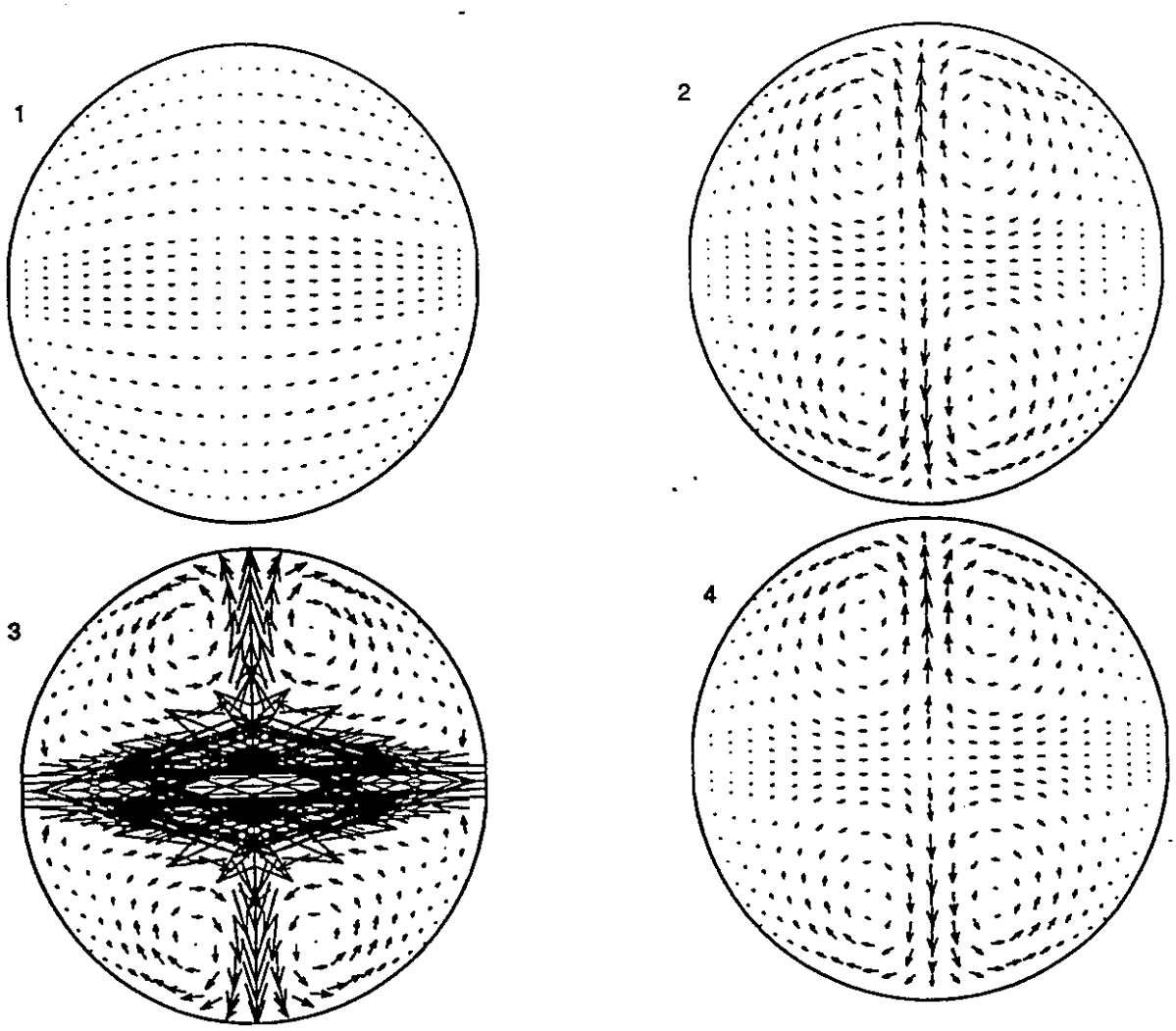

Fig.5.08: Velocity vector plots at

different horizontal planes, Re_{jet}=75

1. 0.1775 D from bottom
2. 0.6870 D from bottom
3. 1.0000 D from bottom
4. 1.4250 D from bottom

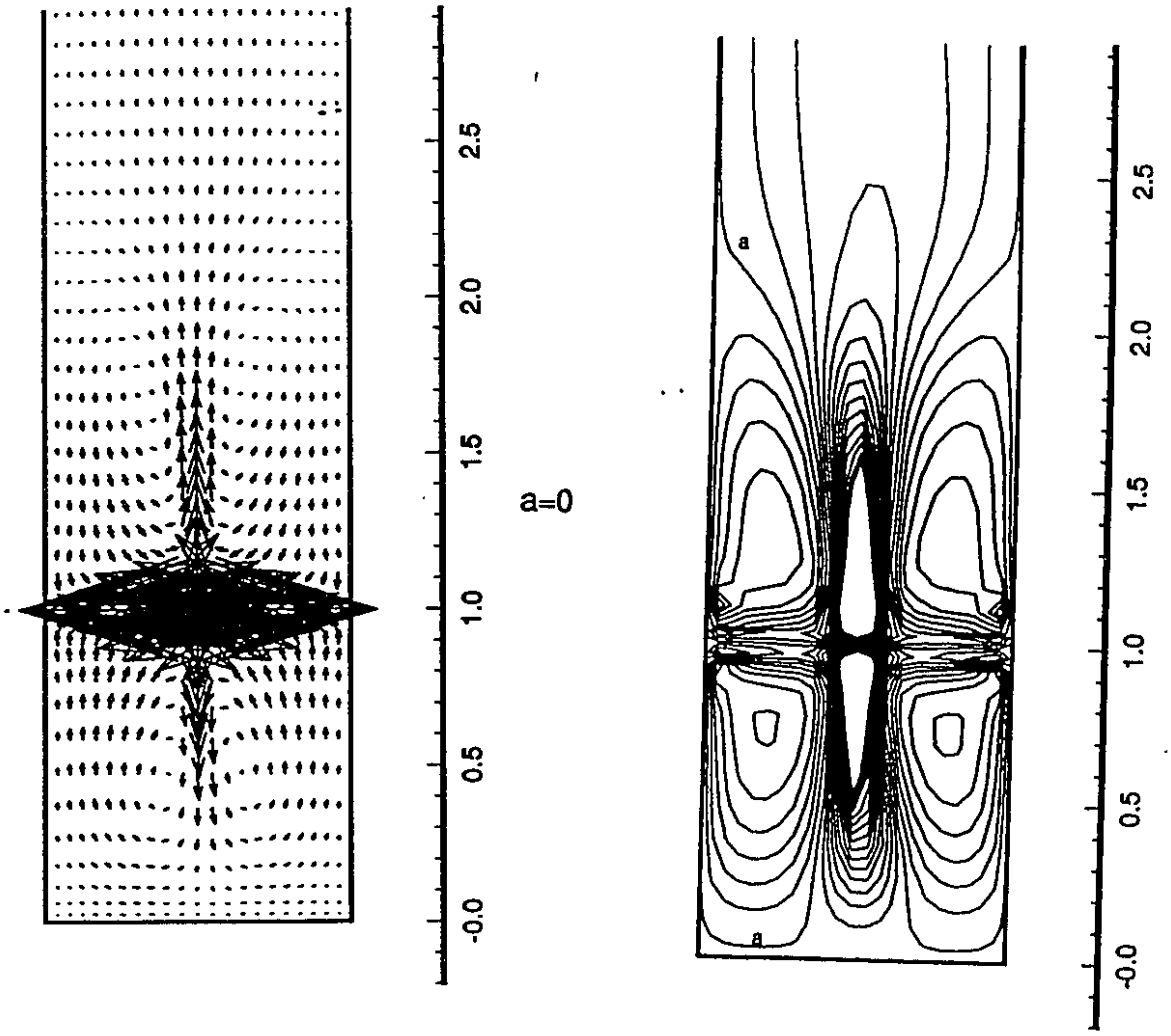

Fig.5.09: Velocity vector and u-velocity contour plots along the vertical jet impingement plane, Re_{jet}=75

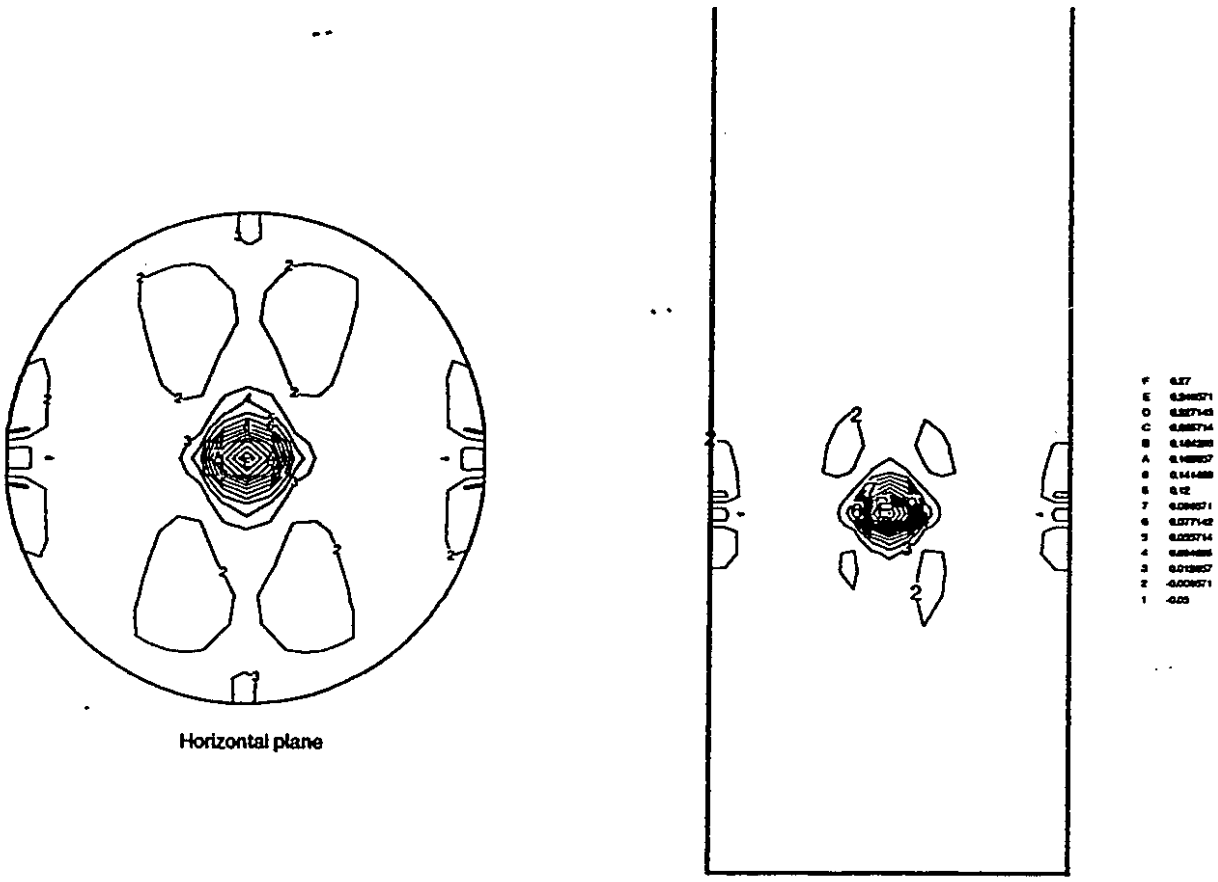

Fig.5.10: Pressure contour plots along the horizontal and vertical jet impingement planes, Re_{jet}=75

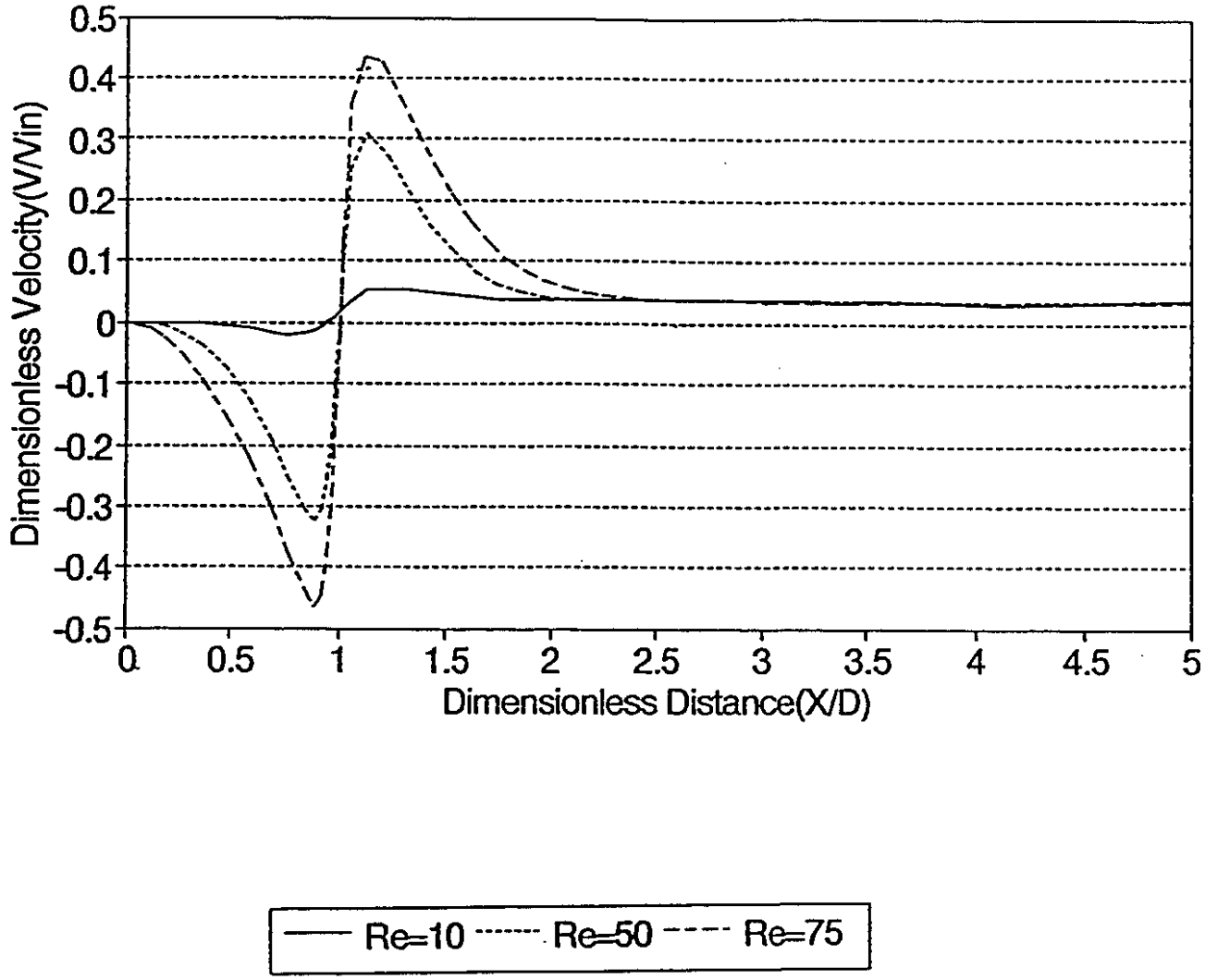

Fig.5.11 Centerline axial velocity comparison

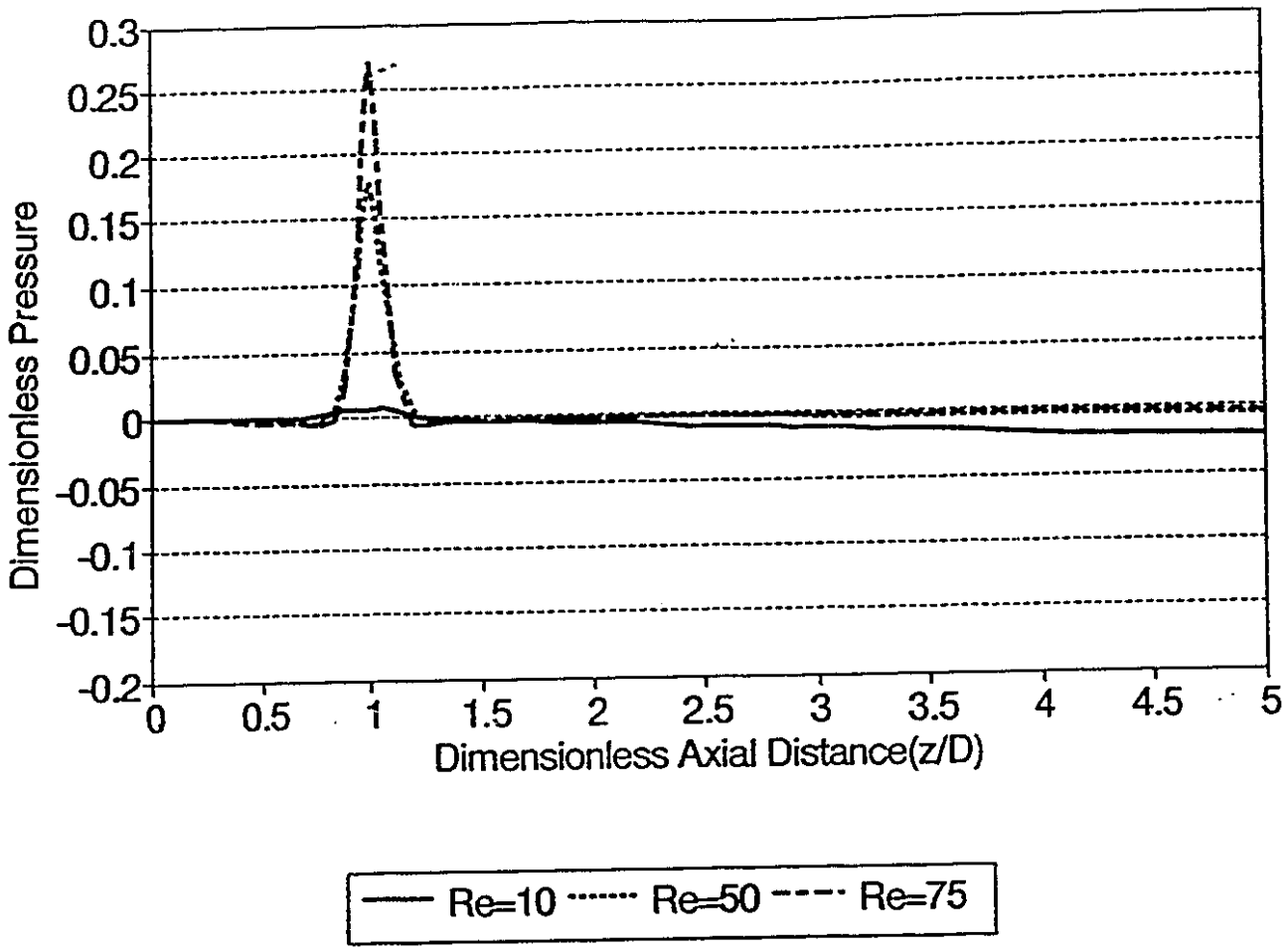

Fig. 5.12: Centerline pressure comparison

Fig.5.10) and the center pressure also increases(Fig.5.10). The u-velocity contour plot(Fig. 5.09b) and the pressure contour plot(Fig. 5.10) show that the flow field is now slightly asymmetric.

A comparison of the centerline axial velocity is given in Fig.5.11. As the Reynolds number of the flow increases the velocity profile becomes sharper reaching a higher maximum. A comparison of the pressure through the vertical centerline is given in Fig.5.12. The pressure at the impingement point increases as the Reynolds number increases. At higher Reynolds numbers, the velocity cannot be damped out by viscosity and most of the kinetic energy is converted to pressure. The theoretical inviscid limit for the stagnation pressure is 0.5 since the average inlet velocity is 1.

The calculated flow field is in good agreement with the experimental visualization. The study of Wood et al.(1991) using flow visualization techniques showed that the jets impinge head on and form a radial jet that travels radially. The part of the jet travelling toward the closed end will impinge on the bottom and divide. Similarly, the material leaving the impingement point toward the cylindrical walls will impinge and divide. Re-entrainment of this material by the jet creates a 3-D recirculation zone going around each of the jets. These zones are counter-rotating ring vortices on either side of the impingement plane.

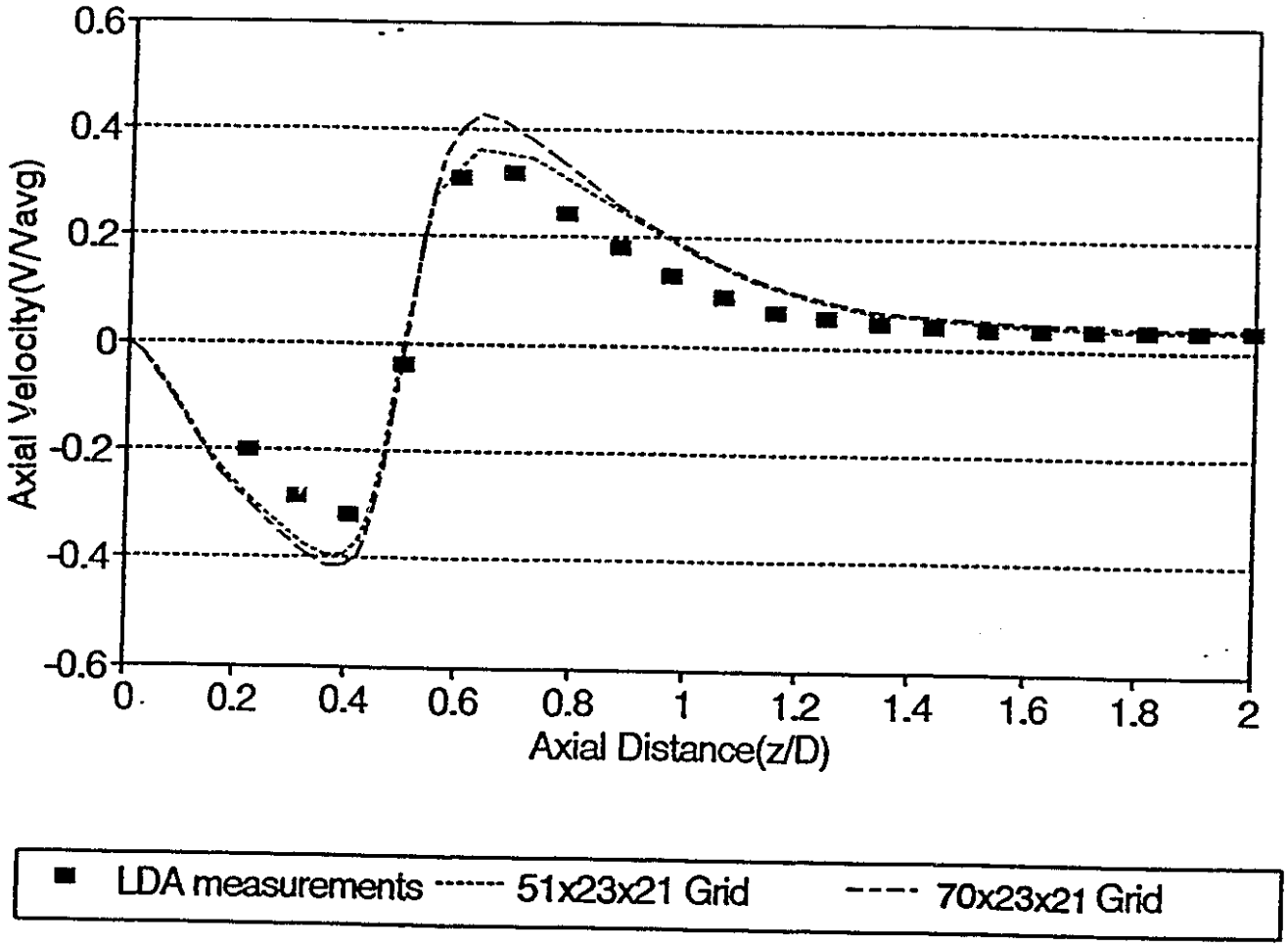

Fig. 5.13 : Centerline axial velocity comparison LDA and numerical, Re=50

Back piston 0.5 chamber diameter away from jets

5.2.2 Back piston, half chamber diameter way from jets

The bottom of the chamber is set at one-half chamber diameter away from the jet outlet. The results are nearly identical to the previous case. At low Reynolds numbers(Re less than 10), the jets do not impinge, but spread out into the chamber without forming recirculation zones. At higher Reynods numbers, the jets impinge head on and four recirculation zones are formed. At a Reynolds number of 50, LDA measurement data are available[Johnson(1990)]. The numerical results for two different grid densities are compared with the L.D.A. data in Fig.5.13. The initial results at 51x23x21 grid density agrees with the L.D.A. results closely. A grid refinement to 70x23x21, changes the solution only slightly.

5.2.3 Unequal Flowrates

The distance between the back piston and jets is kept at a half chamber diameter and one jet is twice the velocity of the other jet. The Reynolds numbers are 50 for the slower jet(left) and 100 for the faster jet(right). The results are given in Fig. 5.14 to Fig. 5.16. The velocity vector plot along the vertical impingement plane shows that jet impingement points moves to a location near the entrance of the weaker jet. The velocity vectors along the horizontal jet impingement plane(Fig. 5.15) also show that the impingement point has moved to the entrance of the weaker jet. The pressure contour plot(Fig. 5.16) shows that the highest pressure occurs near the entrance of the weaker jet.

5.2.4 Concentration

One of the main purposes of the opposed jet configuration is to promote mixing. The mixing phenomenon is very difficult to quantify in detail[Ottino(1989)] . In this work, an approximate treatment is given using the transport equations. In polymer systems, the mixing occurs mainly through convection[Ottino(1989)] and diffusion plays an insignificant part. The transport equation for monomer can be written as

$$\frac{\partial U_i C}{\partial \epsilon_i} = 0 \qquad 5.06$$

The inlet concentration of 1 unit is specified for the left jet. For the wall zero concentration is specified. If mixing occurs, the exit concentration profile would become uniform. The results are given for the Reynolds number 10 and 50. The concentration contours along a horizontal plane, 3 chamber diameters from the jets are given. With the Reynolds number 10, mixing does not occur at all(Fig. 5.17a). The monomer stays only on one side. With the Reynolds number 50, the concentration contours show that the monomer which enters from one side travels to the other side. The contours show that the concentration is still higher on one side. The slight mixing at the Reynolds number of 50 can be explained by the presence of the impingement point which acts as the hyperbolic point of a dynamical system. The presence of hyperbolic points promote mixing[Ottino(1989)]. The existence of a hyperbolic point is discussed in detail in Chap. 7.

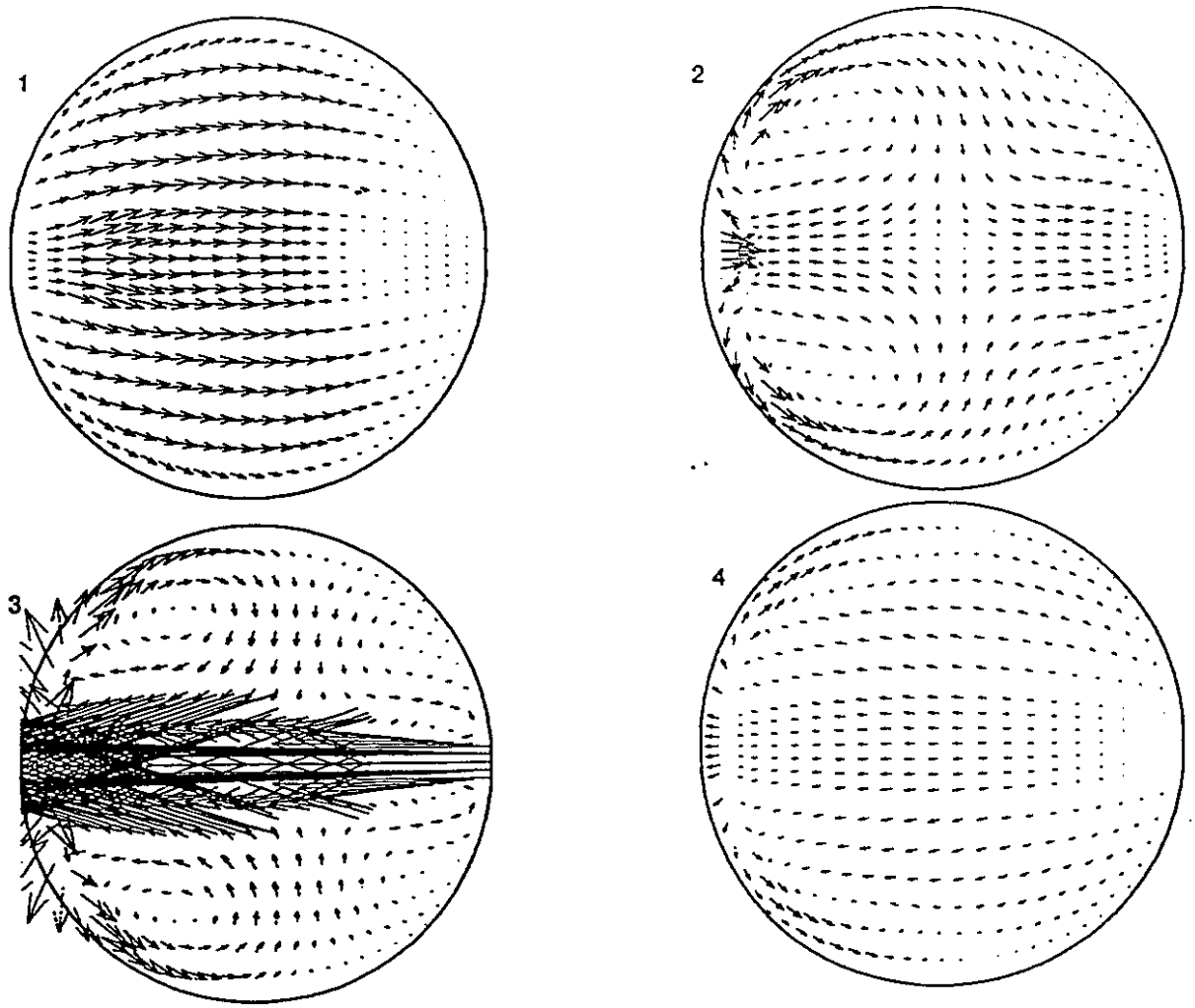

Fig. 5.14: Velocity vector plot along different horizontal planes,

Unequal flowrates

1. 0.0841 D from bottom
2. 0.3254 D from bottom
3. 0.5000 D from bottom
4. 0.9110 D from bottom

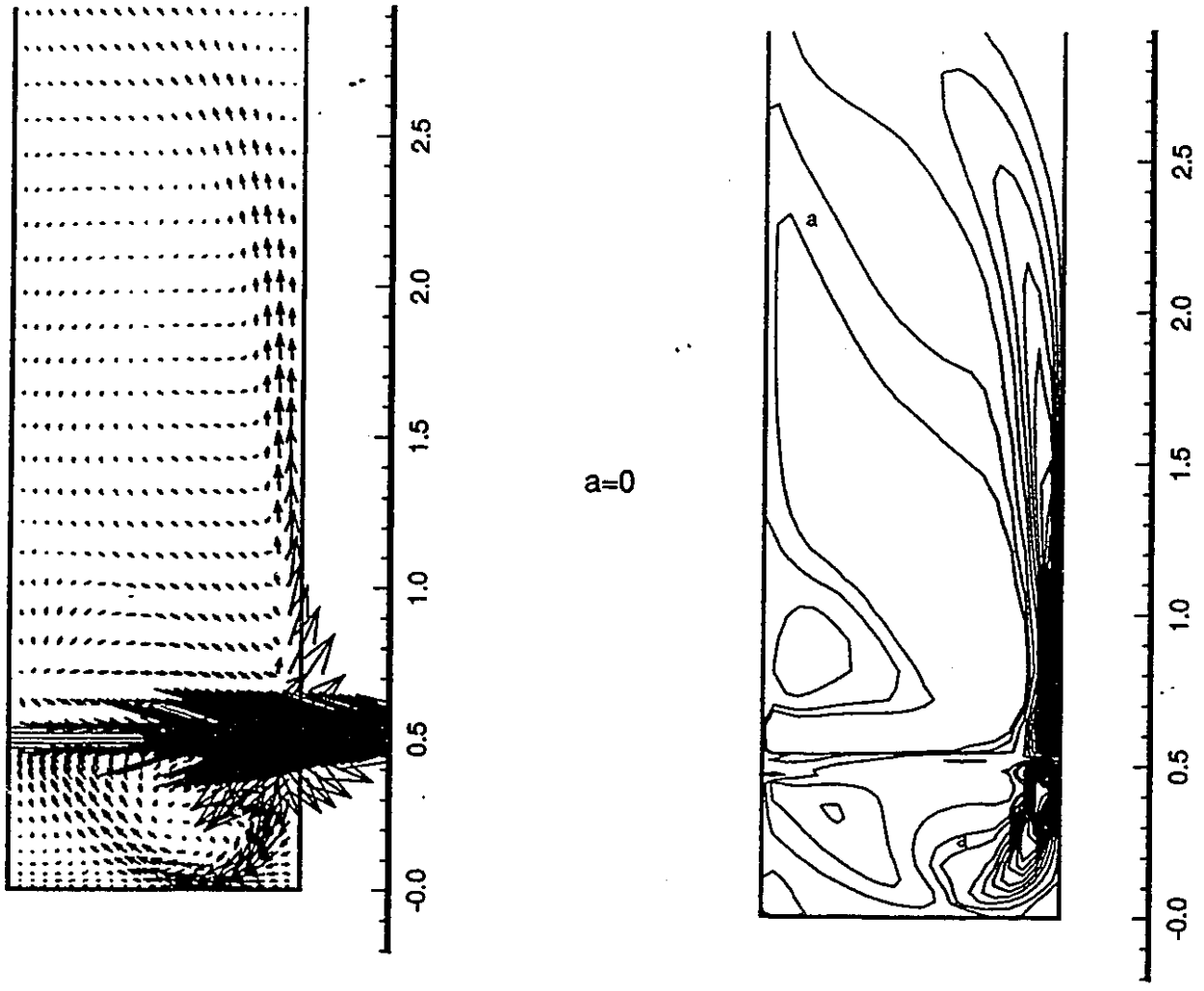

Fig. 5.15 : Velocity vector and u-velocity contour plots along the vertical jet impingement planes, Unequal flowrates

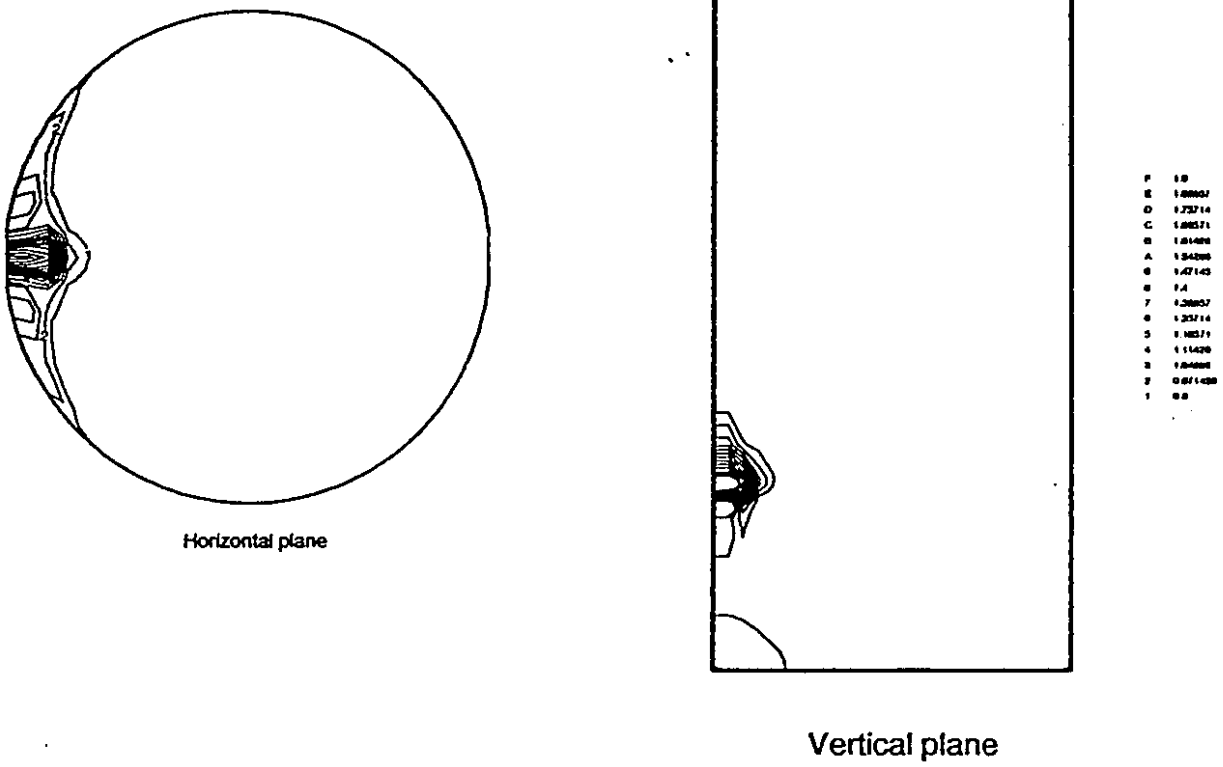

Fig. 5.16: Pressure contour plots , horizontal and vertical impingement planes

Unequal flowrates

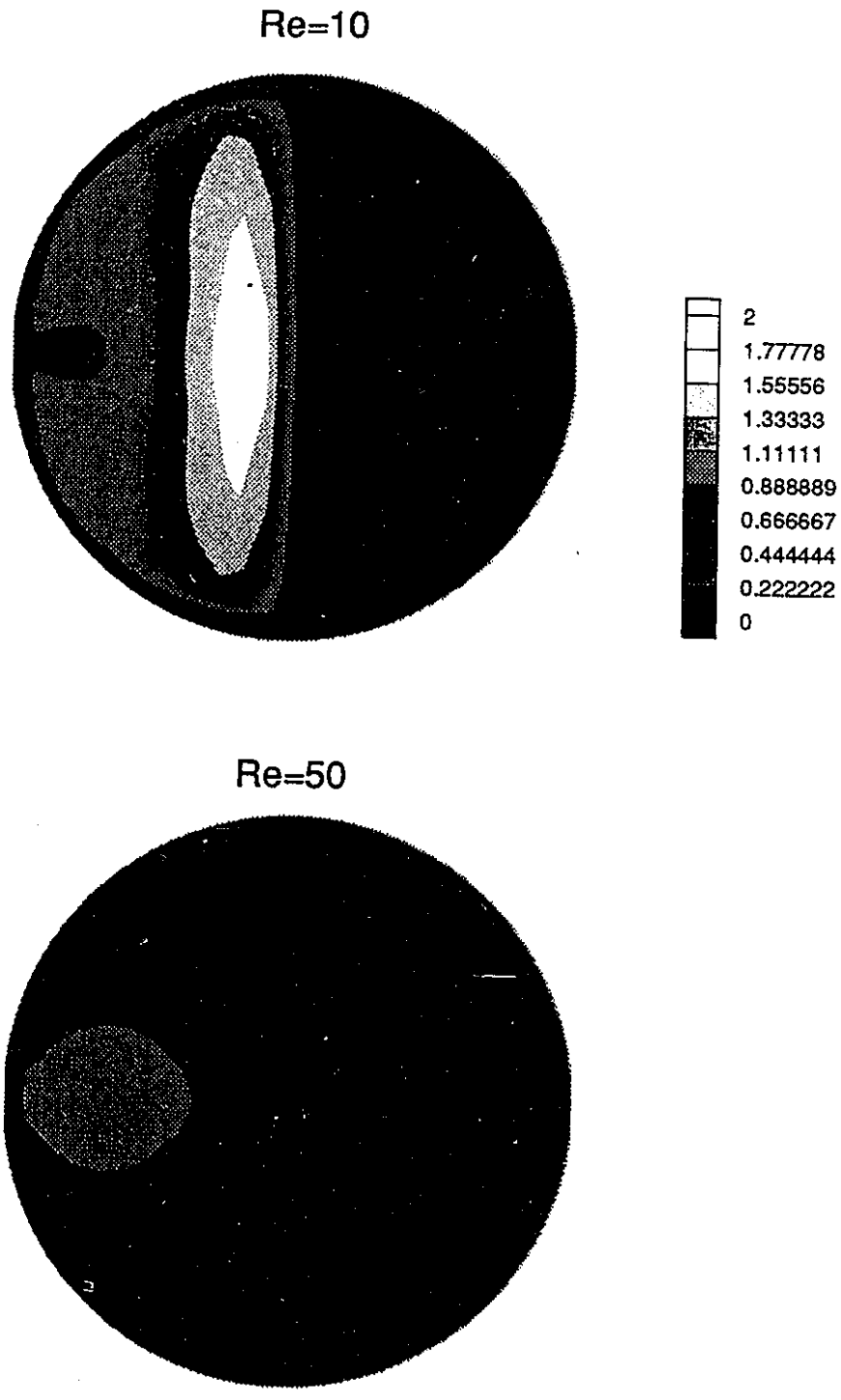

Fig. 5.17: Concentration contours along the horizontal planes

Three chamber diamters from bottom

6. Unsteady Opposed Jet Flow

In this chapter the time dependent behaviour of the opposed jet flow field is studied. Flow fields can be steady and symmetrical for limited ranges of parameters that characterize them. Outside these ranges, a flow field encounters instability and can exhibit a more complicated asymmetrical steady state or unsteady behaviour. The point at which the symmetrical steady state can no longer be sustained is called the transition or critical point[Sobey and Drazin(1986)]. The transition from, a symmetric steady state to another set of states is called bifurcation[Drazin and Reid(1981)]. Several modes of bifurcation can exist. A pitchfork bifurcation occurs when a symmetric steady state forms a new more complex asymmetric steady state. Transition to a time periodic oscillation is called the Hopf bifurcation[Drazin and Reid(1981)]. The purpose of this section is to explore the behaviour of the opposed jet flow field above the critical point using nonlinear time integration as developed in the previous chapters. Several previous numerical studies, which explored the transient behaviour of a flow field, are reviewed first. Although previous studies predominantly focused on the 2-dimensional flow field, some useful insights can be gained with the numerical methods used to capture the oscillations.

Flow around a cylinder shows an instability at a Reynolds number based on a cylinder diameter of about 30. Above this Reynolds number, the flow field oscillates and vortex shedding occurs. The first numerical study to predict vortex shedding was carried out by Fromm and Harlow(1963). The initial perturbation was provided by impulsively

starting the cylinder, i.e., a uniform velocity field was specified everywhere. They used central differencing for both convection and diffusion terms, which resulted in physically unrealistic oscillations in front of the cylinders. Sobey and Drazin(1986) showed that the flow through an expanding channel exhibits a wide range of steady state and unsteady behaviour. At low Reynolds numbers, the channel flow field is symmetrical and steady. When the Reynolds number is increased, the symmetry through the channel centerline breaks down and the flow field forms an asymmetrical two dimensional steady state. At higher Reynolds numbers three dimensional steady state occurs and when the Reynolds number is sufficiently large, unsteady oscillation occurs. A numerical method was used to integrate the two dimensional equations in time. A typical run took 30 CPU hours on a Cray 1 computer. They concluded that their numerical results agreed with experiments up to a Reynolds number of 150. Davis and Moore(1982) used the QUICKEST scheme of Leonard(1981) to study the flow over rectangles. To obtain the oscillations that are consistent with experiments, a higher-order upwinding method was needed for the convection terms. The grids used varied from 41x40 to 61x74, and up to 24 CPU hours were required to obtain a steady oscillation.

The experimental works of Sandell et. al(1985) and Wood et al. (1991) suggest that the opposed jet flow field becomes oscillatory above a critical Reynolds number. Using the stability theory terminology, a Hopf bifurcation exists. The critical or the transition point depends on the geometry of the system. Important factors include the jet diameter to chamber diameter ratio and the angle of jets with respect to the cylinder

wall.

6.1 Problem formulation

The non-dimensional formulation of the previous chapter is extended to include the time derivative. The dimensionless time is given by

$$\bar{t}=\frac{tV}{D} \qquad 6.01$$

where V is the inlet velocity. A dimensionless number called the Strouhal number is used to characterize the fluid oscillation.

$$St=\frac{fd}{V} \qquad 6.02$$

The jet diameter,d, is chosen as the characteristic length since the distance at which the change in velocity occurs is nearly d. Dynamically similar systems have the same Strouhal number.

6.2 Results and Discussions

The grid used in the unsteady simulations is shown in Fig. 5.01 . Two mesh densities were used in the simulations(51x23x21 and 70x23x21) to determine the effects of grid density on solution accuracy. The grid size limitation is imposed by the need to do the problem in a reasonable CPU time.

At low Reynolds numbers(less than 75), the steady iteration process yields solutions that satisfy the mass and momentum constraints and the solution obtained is symmetrical about the vertical center planes. At Reynolds numbers greater than 75 the steady iteration process produces an asymmetrical solution. At time t=0 this asymmetric, steady state solution is used as the initial condition for the Reynolds number of 100. In the first stage we advance the velocity and pressure components from the previous stage at $t=t_n$ to the new state at time $t=t_n+\Delta t$. At each time step, the SIMPLEC algorithm is applied. The momentum equations are solved first and the pressure correction equation is solved to obtain a velocity field with zero divergence. The time integration was carried out with an arbitrary time step size Δt at first. The time step was decreased until the velocity oscillation, monitored at 4 diameters above the jets, did not change. The largest time step, Δt, used is .1 and the smallest, at high Reynolds numbers, is .005. Usually up to 50 iterations are required to obtain convergence to 1e-6. At higher Reynolds numbers the solution from lower Reynolds numbers are used as the initial condition.

6.1.1 Piston head full chamber diameter away from jets(H=D)

In the first set of runs, the bottom of the chamber(piston head) was positioned at a full chamber diameter below the jets. A grid size of 51x23x21 is used. At a Reynolds number of 100, the time integration with the steady state solution as the initial condition, shows that a rather slow movement of the flow field exists. The lateral velocity at 4 jet diameters above the jet impingement plane on the chamber centreline is monitored. The

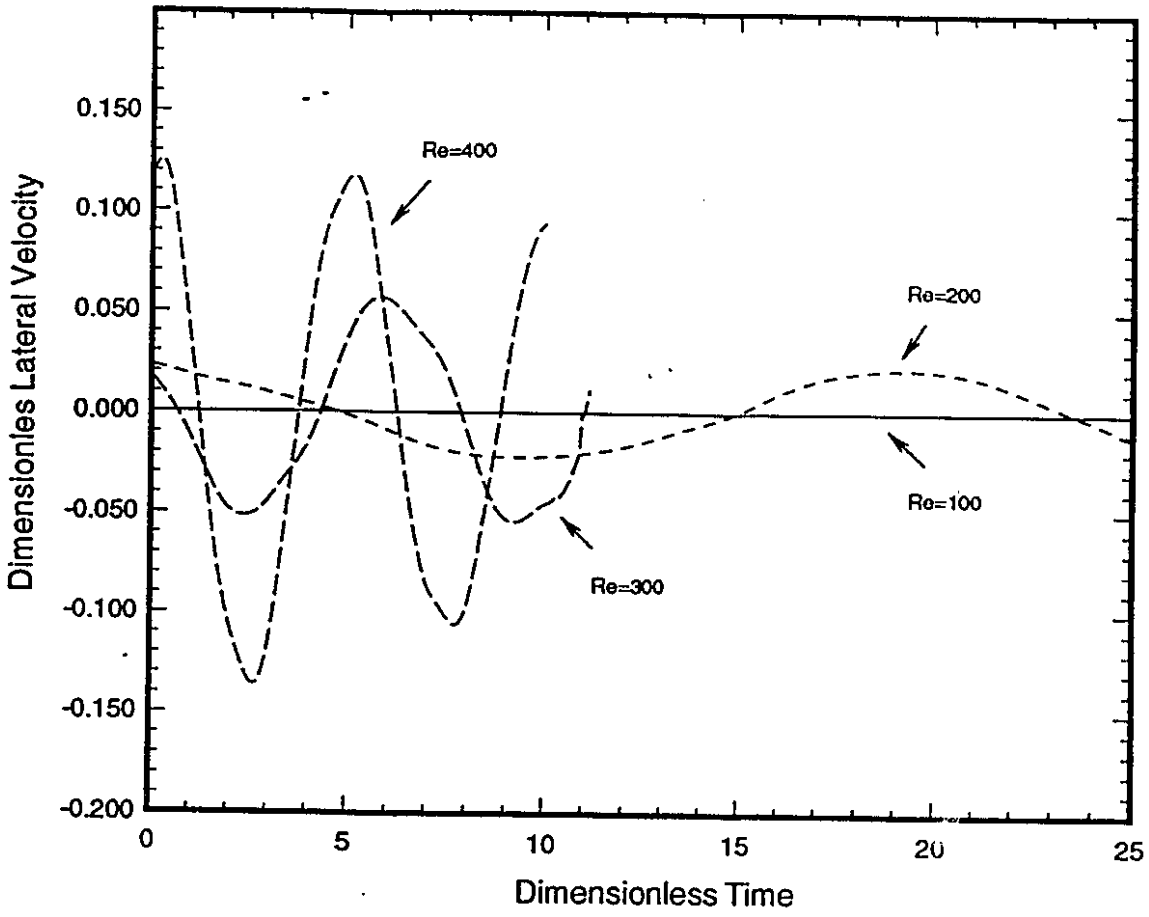

Fig. 6.01 : Time series at different Reynolds numbers

Piston at full chamber diameter away from jets

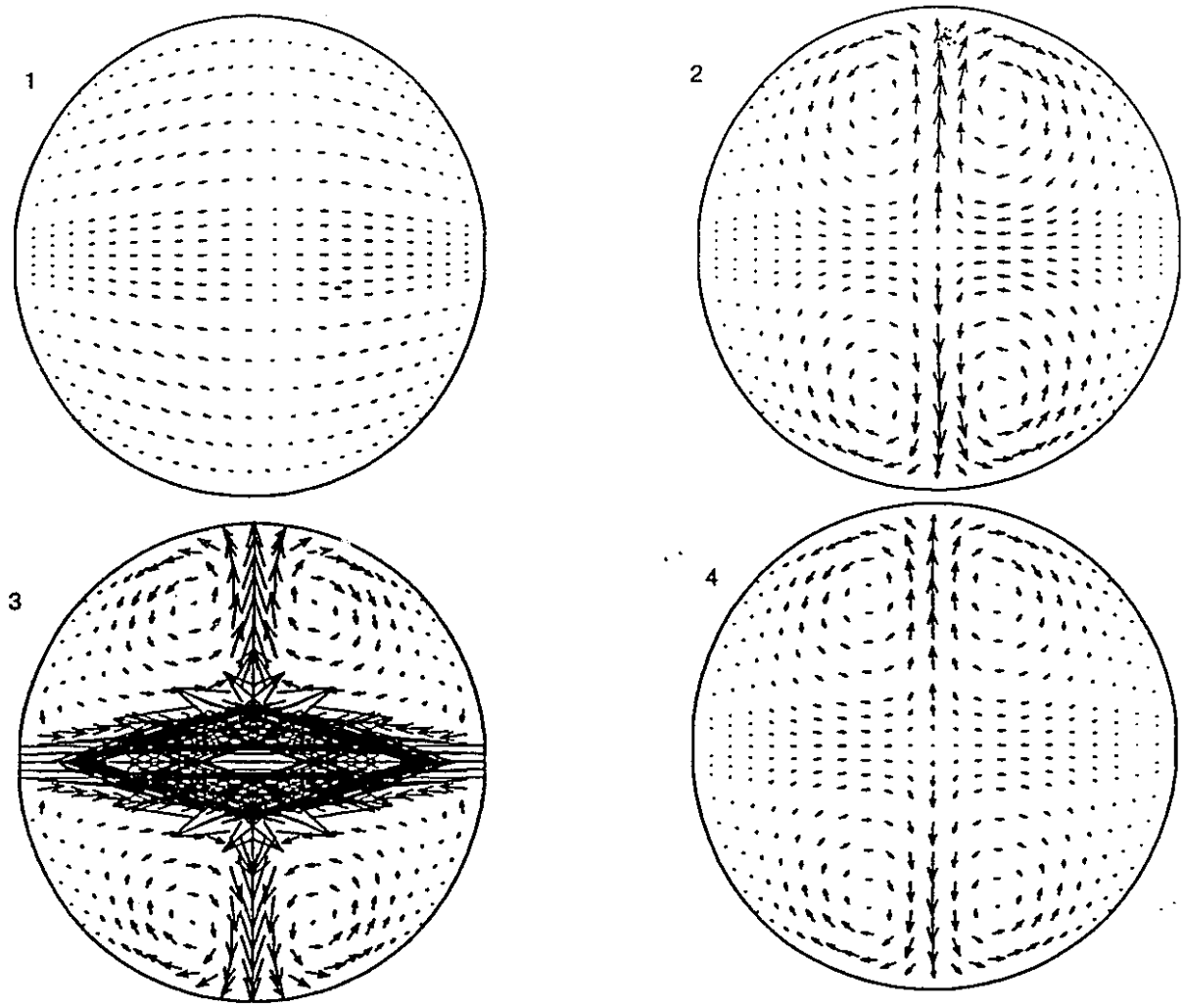

1. 0.1775D from bottom

2 . 0.6870D from bottom

3. 1.0000D from bottom

4. 1.4250D from bottom

Fig. 6.02 : Velocity vector plot horizontal planes, Re=100

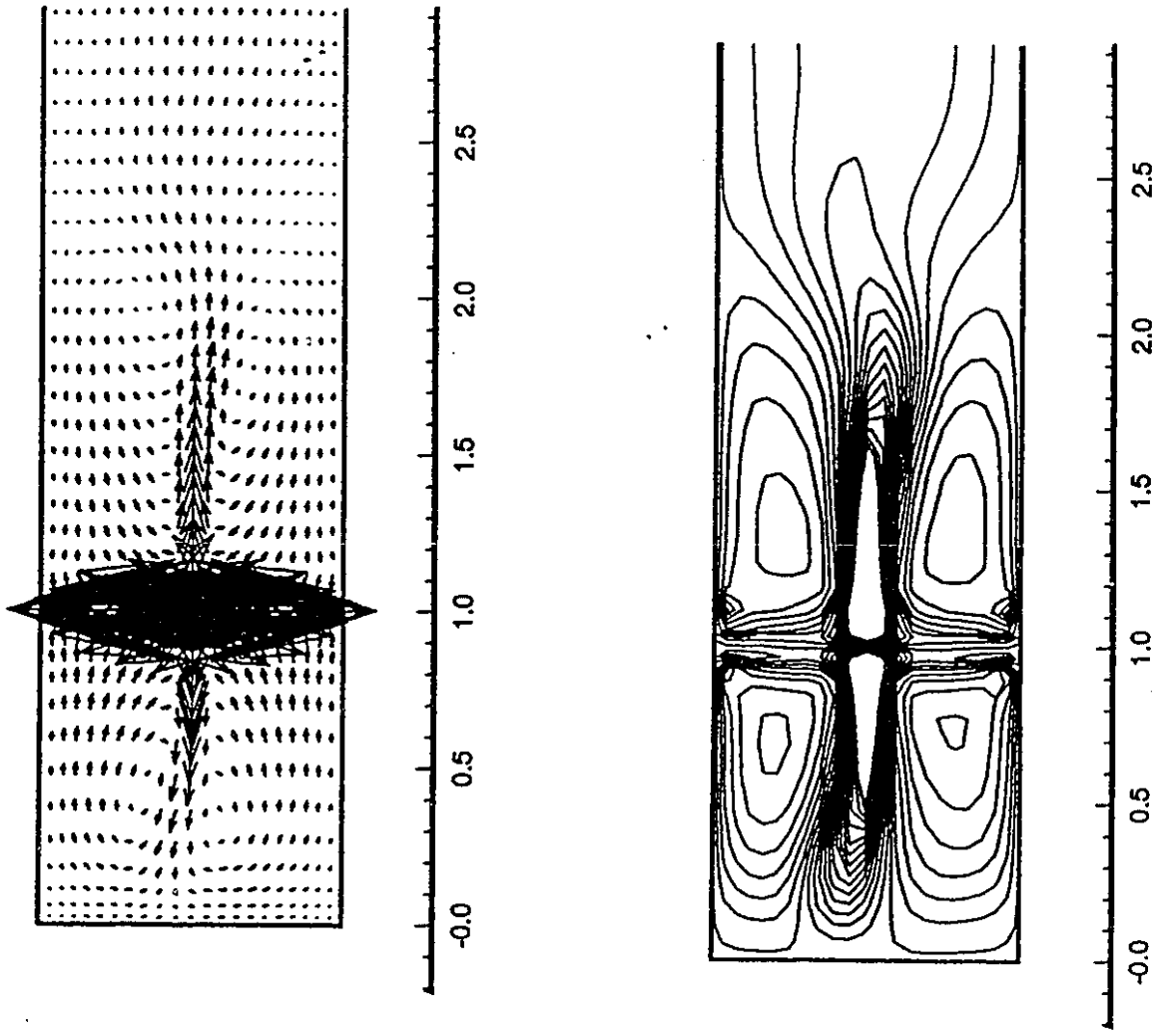

Fig. 6.03 : Velocity vector and u-velocity contour plot

vertical jet impingement plane, Re=100

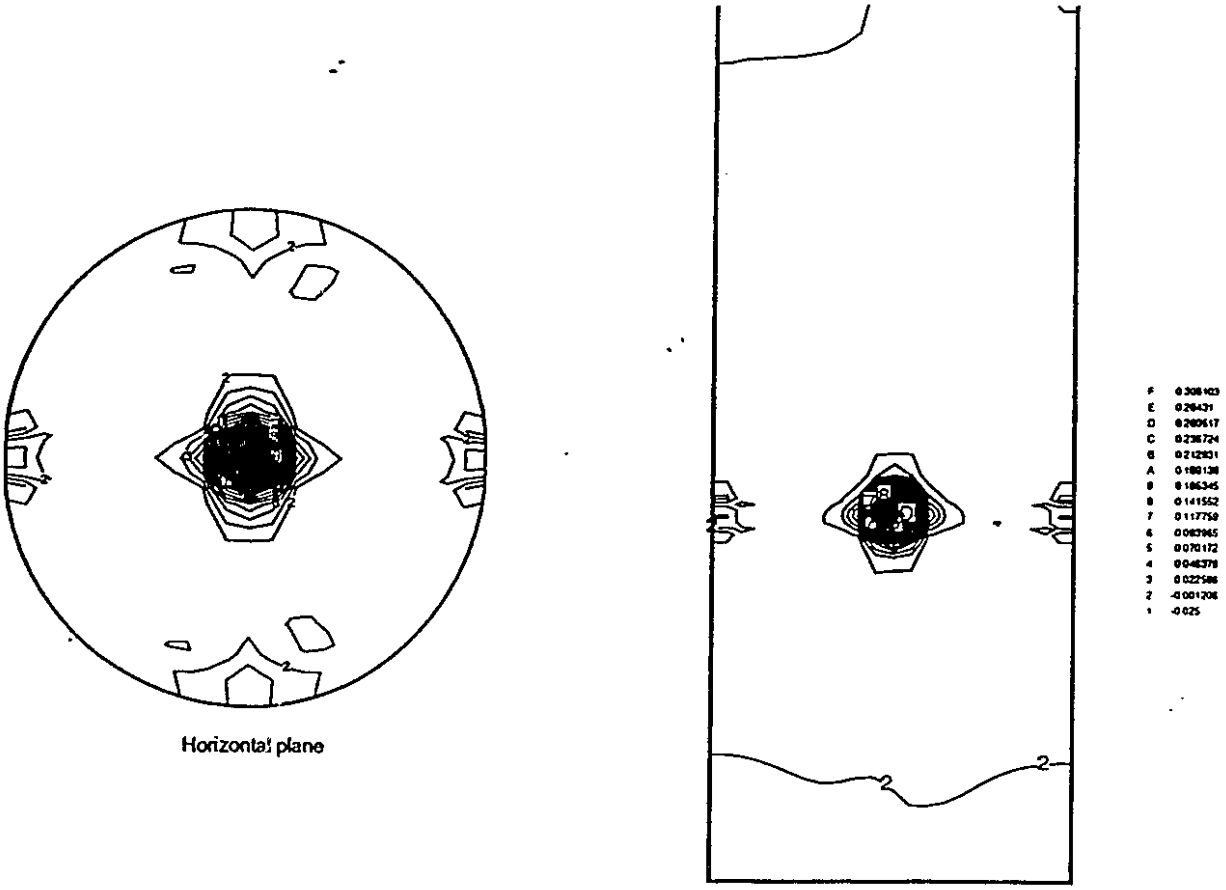

Fig. 6.04 : Pressure contour plots horizontal and vertical jet impingement planes, Re=100

result is plotted in Fig.6.01 for four different Reynolds numbers(100,200,300,400). At a Reynolds number of 100 the period is rather large and the magnitude of the oscillation less than 1.e-3. At higher Reynolds numbers the period decreases and the magnitude of oscillation increases. The results are expressed in Strouhal numbers and are plotted in Fig. 6.05. The instantaneous flow pattern at the Reynolds number of 100 is shown in Fig. 6.03 to Fig.6.04.

Several observations can be made. The dimensionless pressure at the impingement point reaches .32 which is close to the theoretical, maximum inviscid pressure of 0.5. The vector plots on the horizontal planes show that the oscillation is symmetrical with respect to the center plane that corresponds to the vertical jet impingement plane.

6.1.2 Piston head half chamber diameter away from jets(H=.5D)

Initial results were obtained with a 51x23x21 grid. The time series of the lateral velocity at the monitoring location were obtained and the results showed the same trend as the previous case with H=D. A sinusoidal oscillation was obtained at each Reynolds number. However, the flow field oscillates at a higher frequency for the same Reynolds number compared to the case of H=D. The results are expressed in the form of Strouhal numbers and plotted in Fig. 6.05. Also included in Fig.6.05 is the data of Sandell et. al(1985). They obtained the measurements in a model for which d/D=0.2 and the jets were directed back towards the piston face. The trend in the data is similar to that of

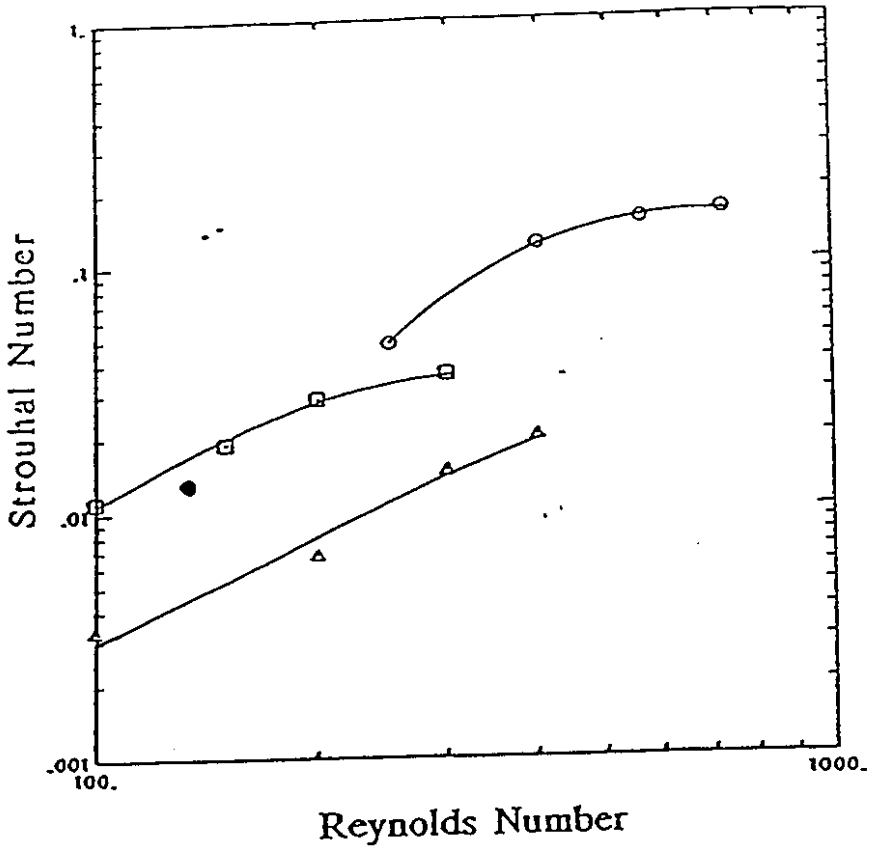

Strouhal number versus Reynolds number: O, Sandell's experimental data; △, H = 1.0 D numerical simulation; □, H = 0.5 D numerical simulation; ●, H = 0.5 D laser doppler anemometer time series measurement.

Fig. 6.05 : Strouhal number vs. Reynolds number

calculations. The dimensionless oscillation frequency increases monotonically for increasing Red but levels off beyond a critical value. Since the Strouhal number is not a function of the Reynolds number(viscosity) above the critical value, the oscillation is a phenomenon dominated by inviscid mechanisms[Panton, 1984] for large Reynolds numbers.

6.1.2.1 Results at higher grid density

The results obtained using the 51x23x21 grid density were obtained before detailed experimental results were available. A detailed flow visualization study and LDA measurements[Wood et. al(1991)] show that there are multiple frequencies in the velocities and the flow structure is more complicated than predicted by the 51x23x21 grid model at a jet Reynolds number of 125. The grid size was increased to 70x23x21 and the steady-state solution at the Reynolds number of 125 is used as the initial condition. More than 600 CPU hours on the Personal Iris workstation were used to do 4250 time steps. In the beginning Δt of .05 was used and reduced to .02 once the initial transients died out and a regular pattern emerged. The axial and lateral velocity components and pressure at 4 jet diameters above the impingement point are monitored and the results are shown in Fig.6.06 to Fig.6.12. The power spectra for these signal are determined using the maximum entropy method given in Press et al.(1989). The alternate method, Fast Fourier Transform(FFT) requires much more data to resolve the spectrum accurately. The time series for the axial velocity(Fig.6.06) shows that the frequency pattern is rather

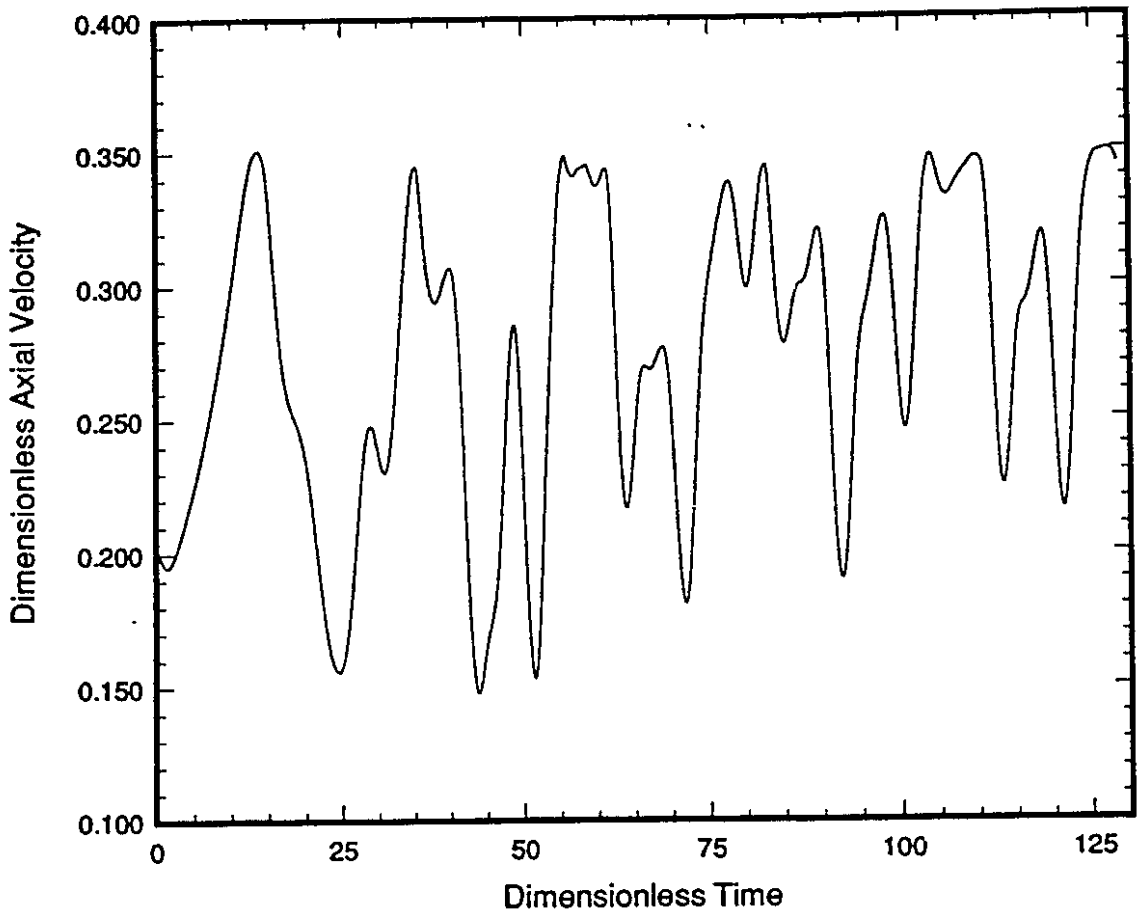

Fig. 6.06: Axial velocity time series

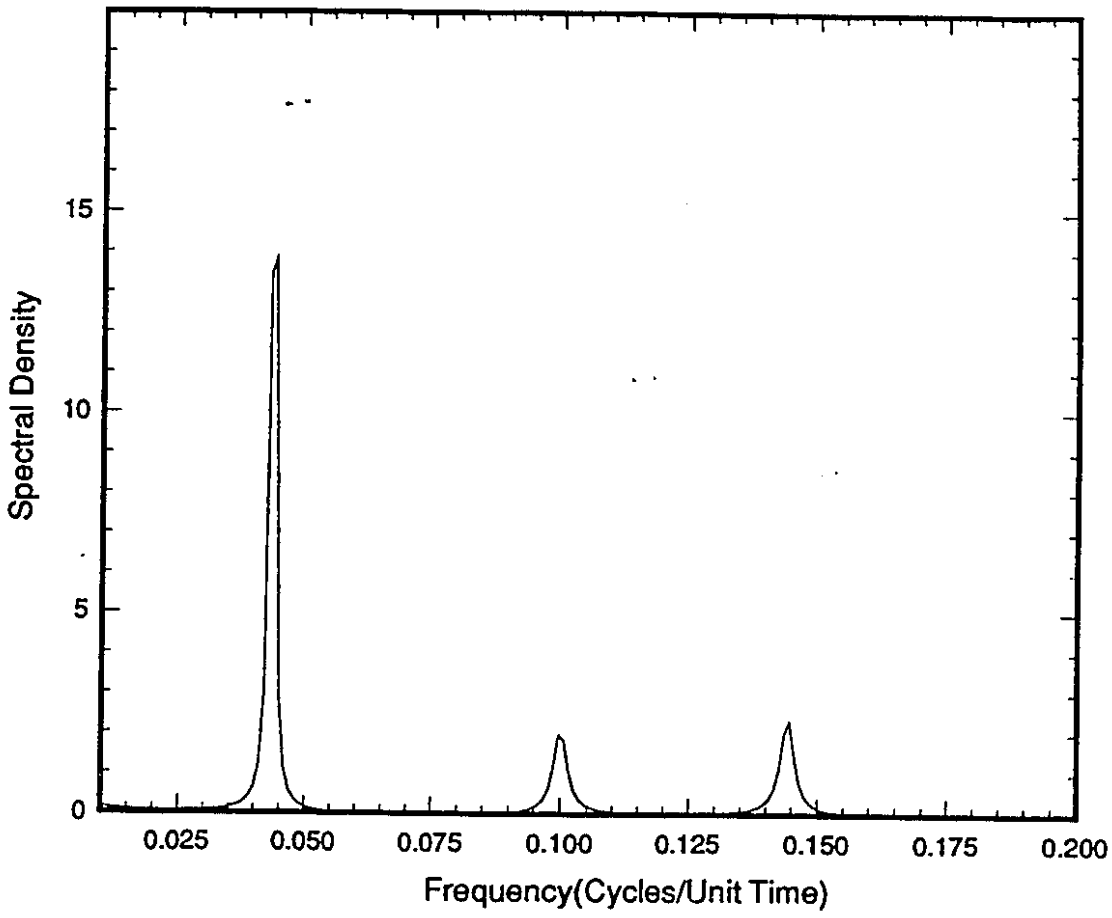

Fig. 6.07: Axial velocity power spectrum

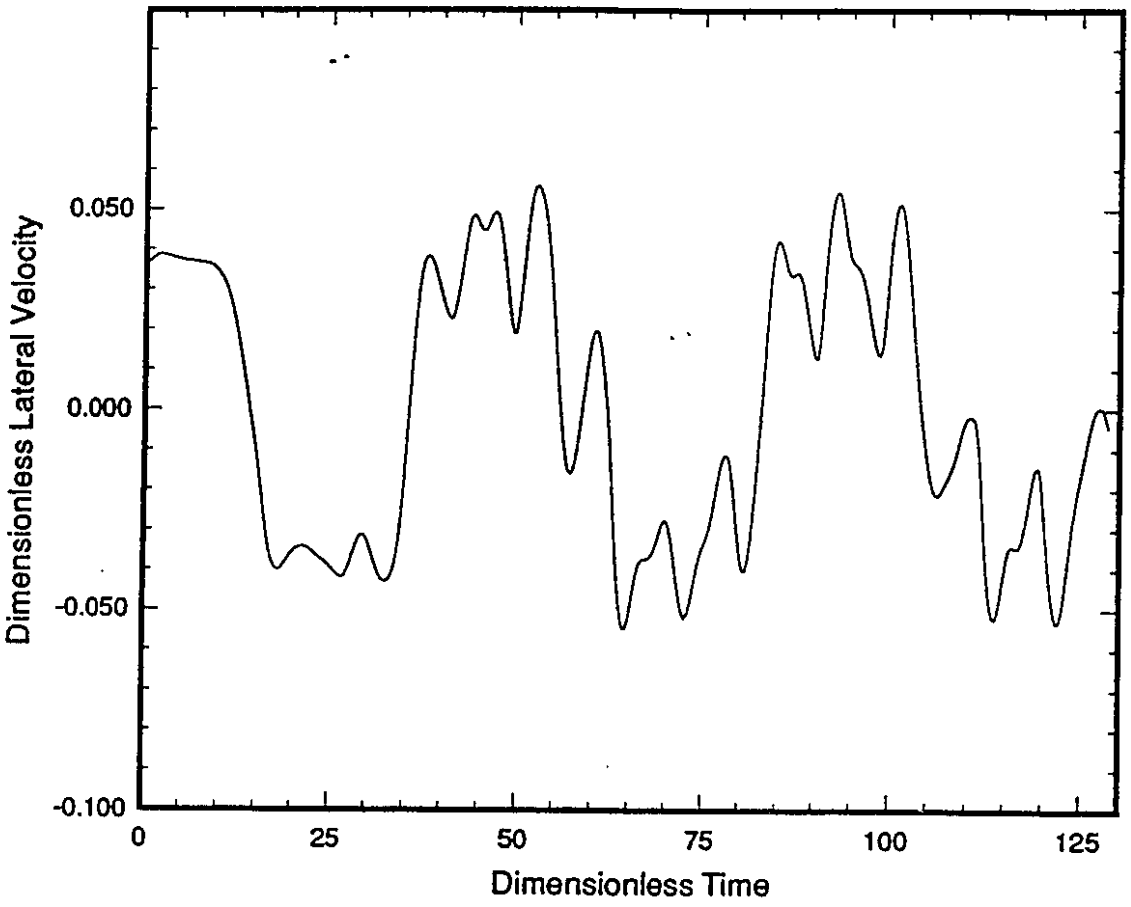

Fig. 6.08 :Lateral velocity time series

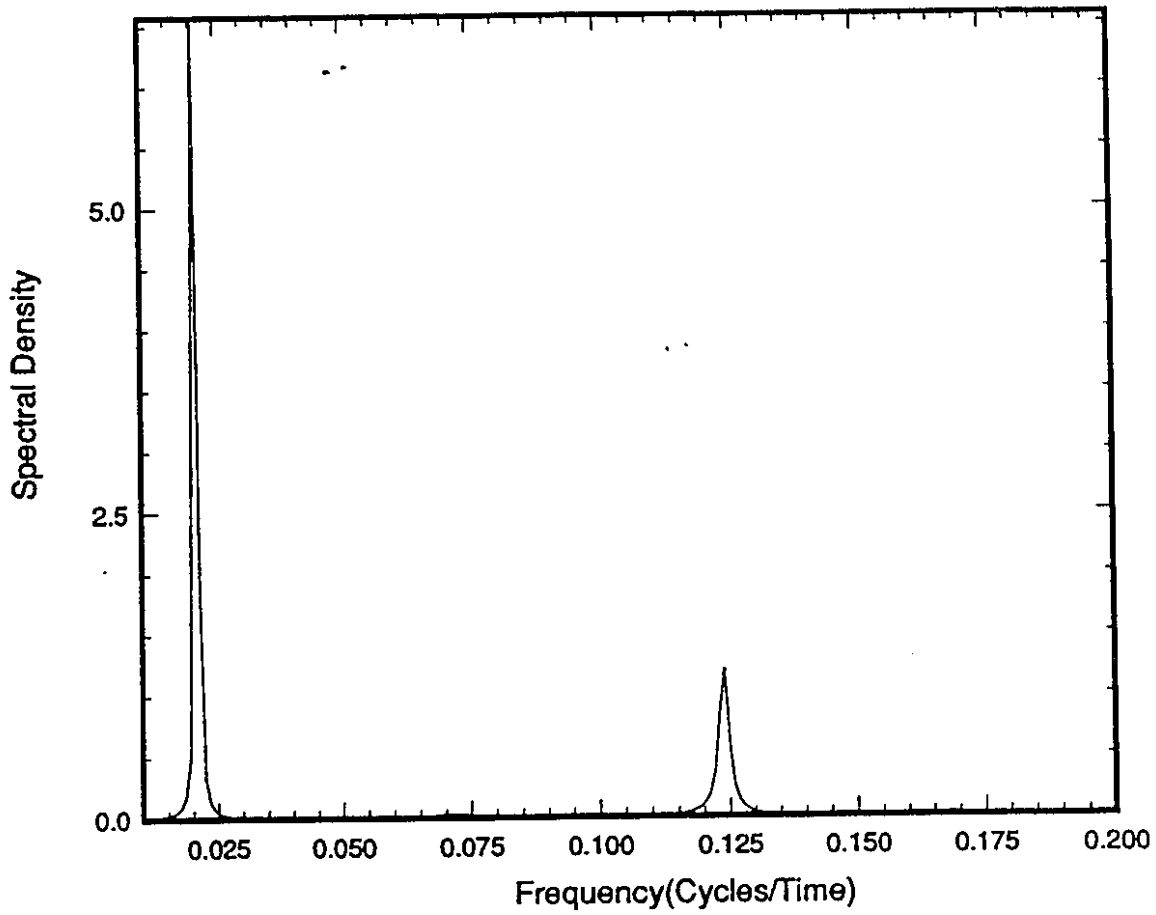

Fig. 6.09: Lateral velocity power spectrum

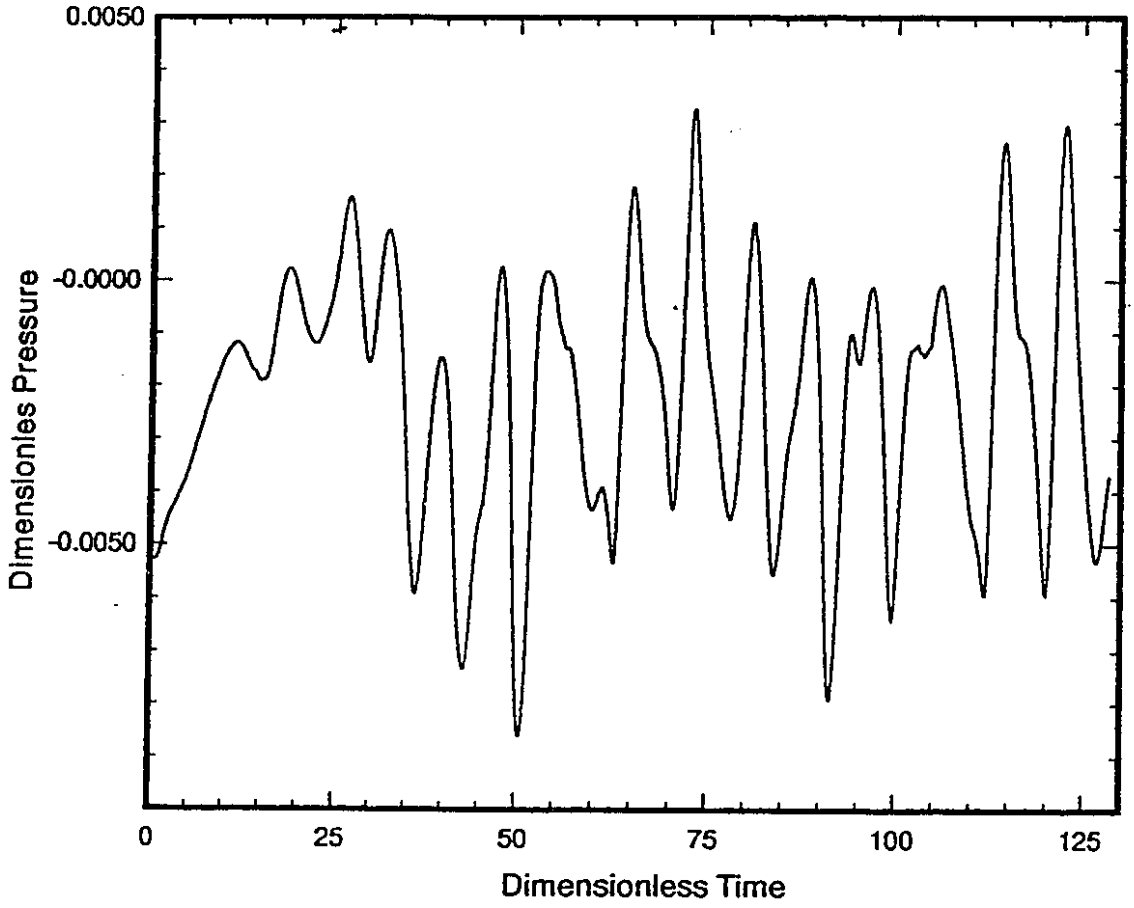

Fig. 6.10: Pressure time series

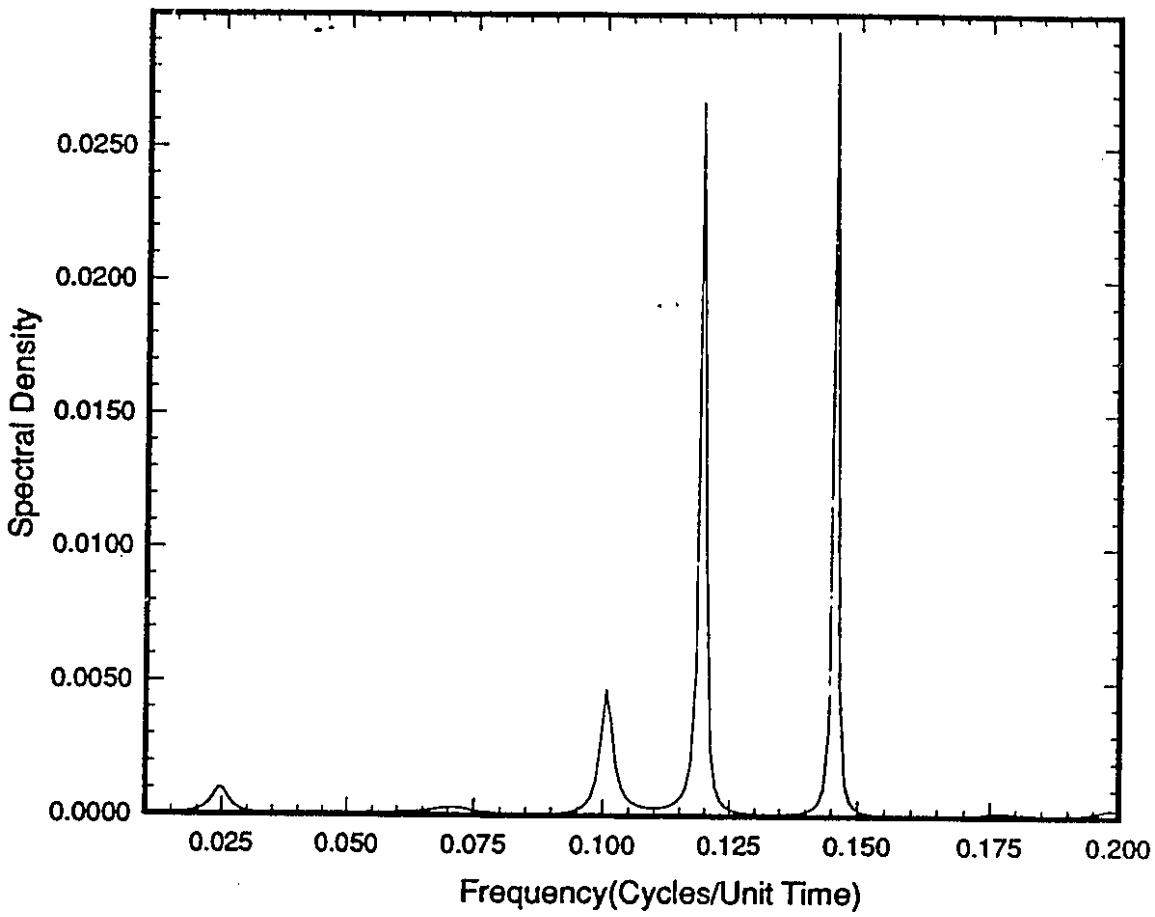

Fig. 6.11 : Pressure power spectrum

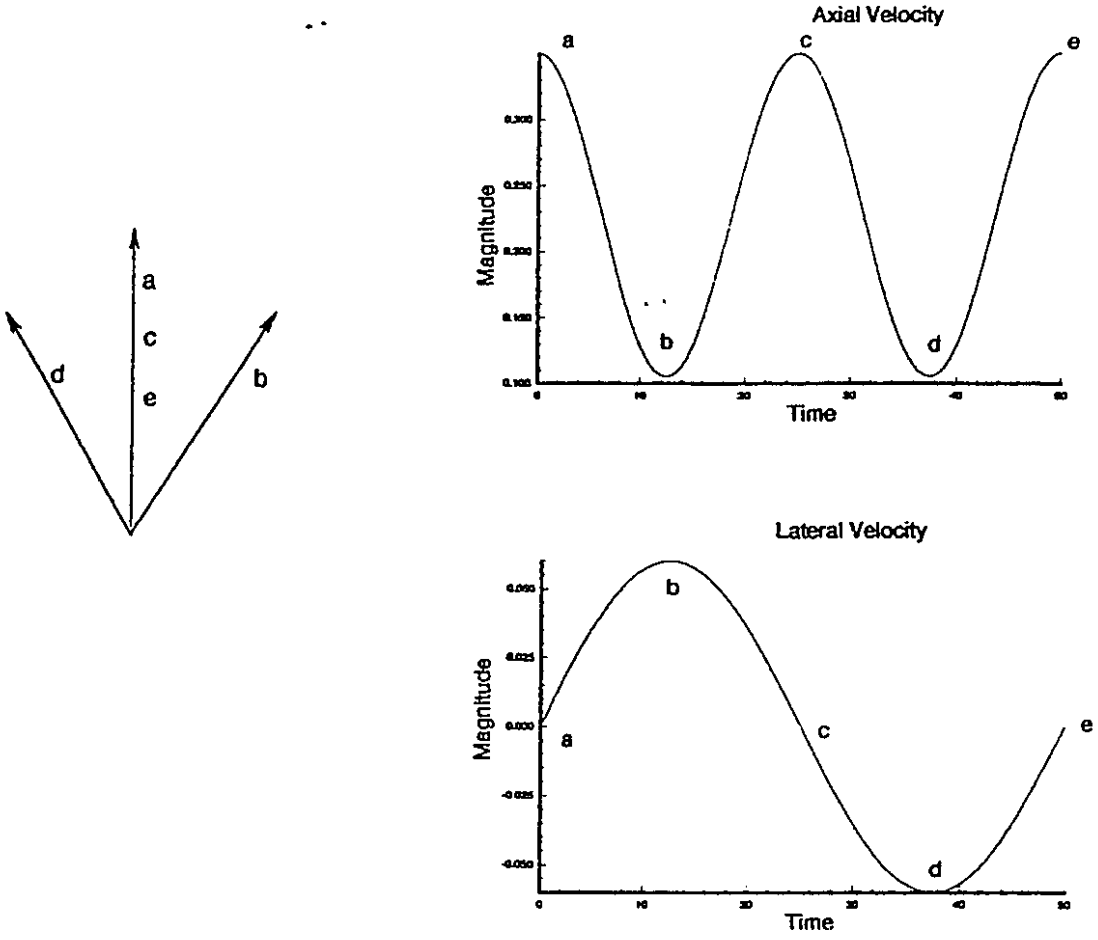

Fig. 6.12: Ideal lateral and axial velocity oscillation

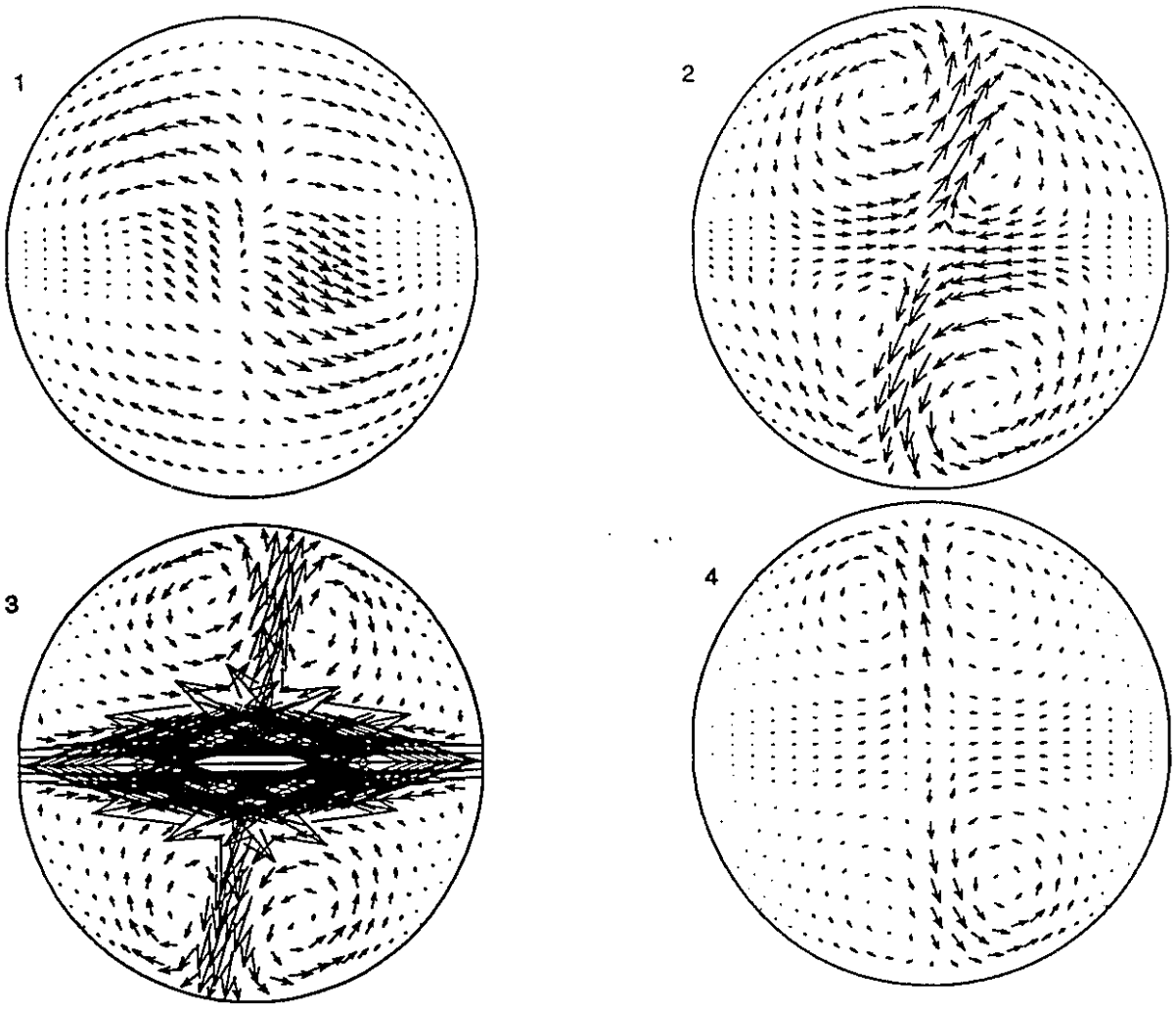

1. 0.0841D from bottom

2. 0.3250D from bottom

3. 0.5000D from bottom

4. 0.8479D from bottom

Fig. 6.13: Velocity vector plots horizontal planes, Re=125, t=112.5

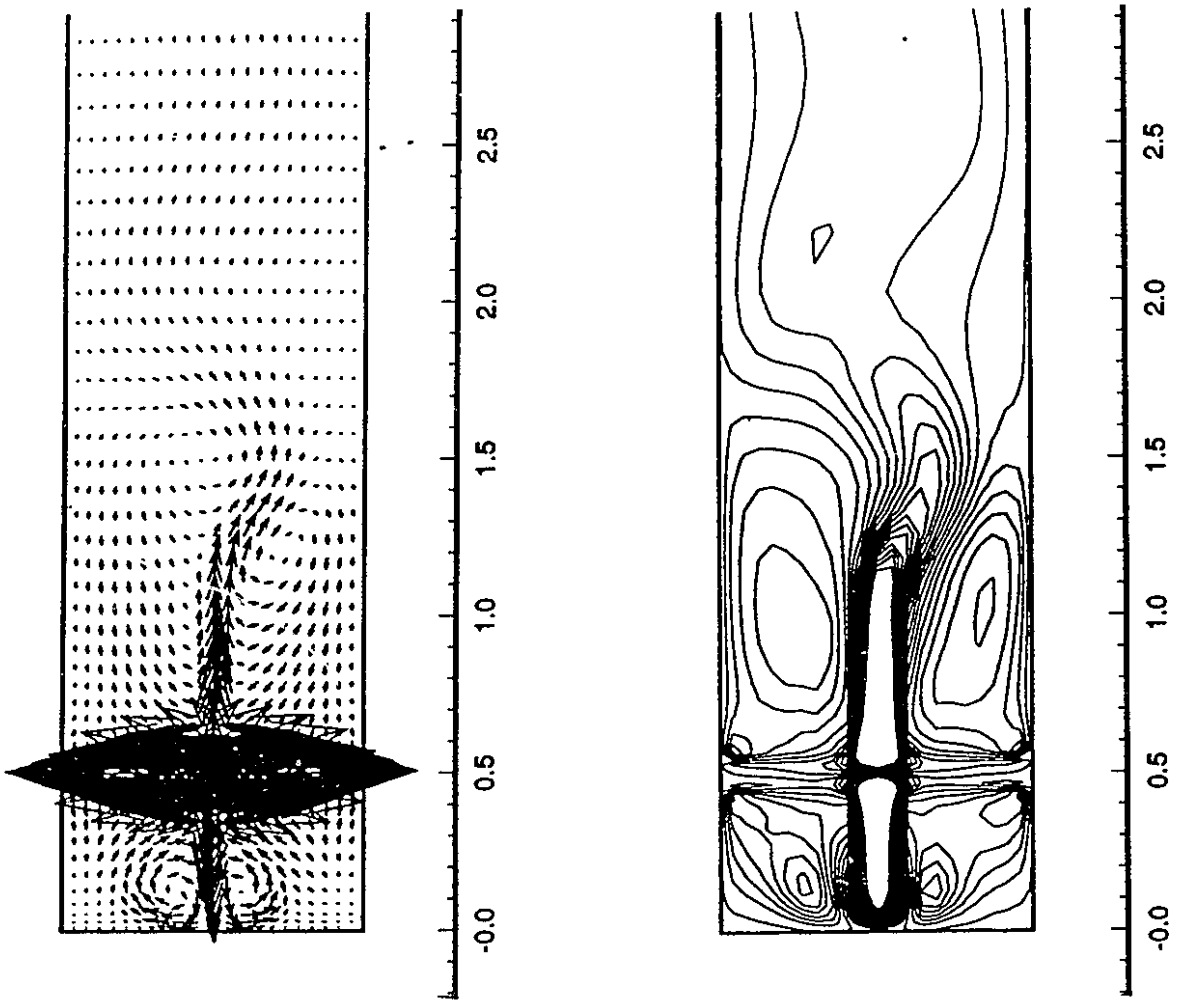

Fig. 6.14: Velocity vector and u-velocity contour plot

Vertical jet impingement plane, Re=125, t=112.5

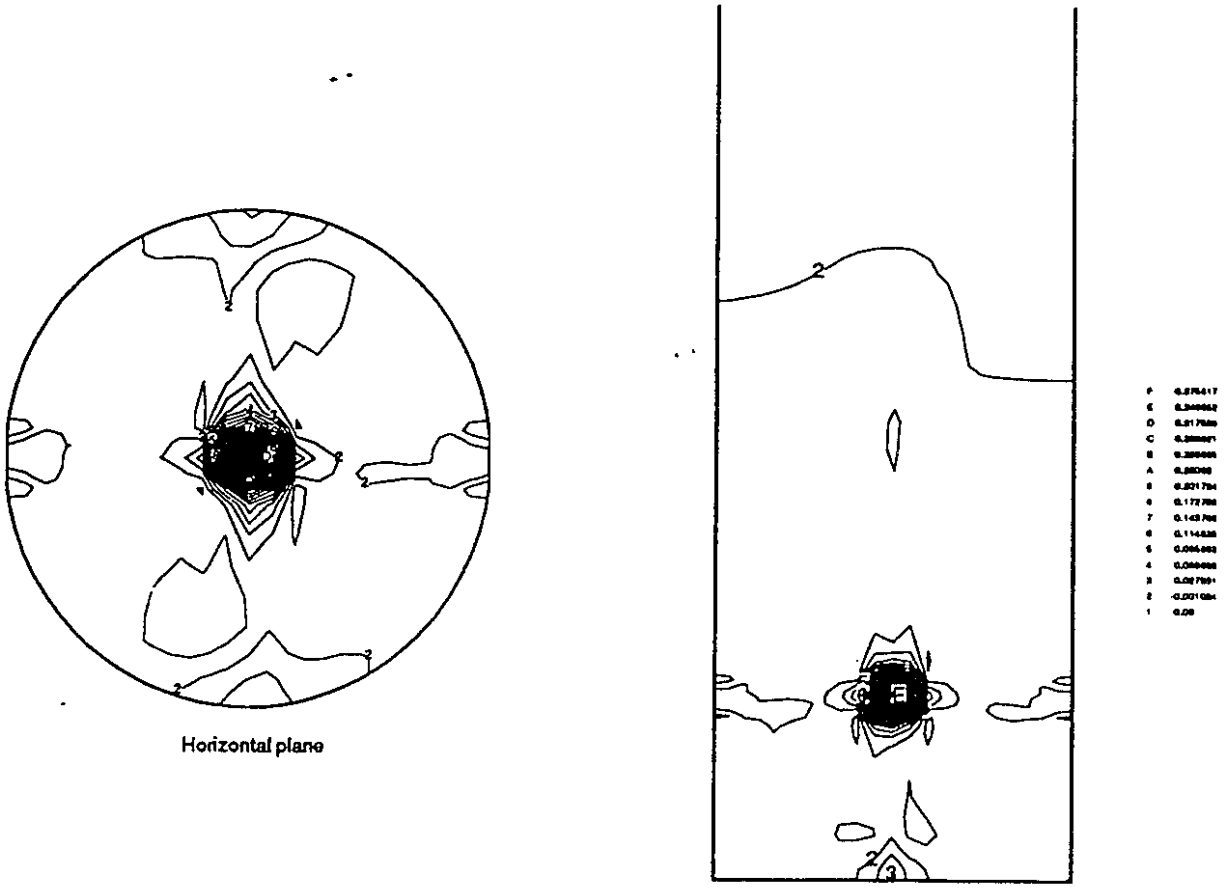

Fig. 6.15: Pressure contour plots, horizontal and vertical jet impingement plane, Re=125, t=112.5

analysis resolves three different frequencies: 0.04 , 0.1 and 0.14 cycles/unit time (Fig. 6.07). The lateral velocity shows that there are two dominant frequencies, 0.02 and 0.125 cycles/unit time(Fig. 6.09). The pressure spectrum(Fig. 6.11) shows a more complex pattern. Four distinct peaks are visible and the peaks which occur at 0.02, 0.1, 0.124 and 0.14 cycles/unit time correspond to the frequencies in the velocity spectra . The frequency of 0.04 for the axial component is due to the lateral oscillation of fluid which generates an oscillation frequency of 0.02 for the lateral component. The idealized illustration of this is given in Fig. 6.12. If the lateral velocity oscillates at a given frequency **f** the axial velocity should contain a frequency of **2f**.

A better understanding of the complex flow field can be gained by examining the flow field at different time steps. The flow field at t=112.5 is shown in Fig. 6.13 to 6.15. The velocity vector plots along the horizontal jet impingement plane is shown in Fig. 6.13 . The velocity vector plot along the vertical jet impingement plane is shown in Fig. 6.14 and the pressure contour plots along the vertical and horizontal jet impingement plane are presented in Fig. 6.15.

The flow field at t=116.5 is shown in Fig. 6.16 to Fig. 6.18. Several observations can be made. The symmetry plane which exists at a Reynolds number of 100 no longer exists at Re=125. The oscillation is a complex three dimensional motion that involves axial and lateral movement of the fluid.

For the opposed jet flow field, the transition from the steady symmetric flow field to oscillation occurs due to the creation of a sharp pressure peak at the point of impingement. As the Reynolds number increases, the impingement pressure also increases and a slight perturbation of the flow field creates a sustained perturbation which cannot be damped out by viscous force.

The grid refinement at the Reynolds number of 125 has a significant effect on the quality of the time dependent solution. This indicates that with the lower grid density the grid was not fine enough to capture the small sub-grid scale motions which exists at this Reynolds number, and the phenomenon captured with the lower density grid does not represent the actual physical phenomenon. This is clearly shown by the previous work of Freitas et al(1985). They studied the flow in a three-dimensional cavity at the Reynolds number of 3200 and with the hybrid-upwinding and lower grid density, the transient numerical method failed to resolve the experimentally observed Taylor-Gortler-like vortices. Only with grid-refinement and a higher-order upwinding scheme for convection, were they able to capture Taylor-Gortler like vortices.

The model results at the higher grid density agrees with the experimental results quite well. Johnson(1990) used an L.D.A. to obtain the time series of the axial velocity at the location 4-jet diameters above the jets. The time series is shown in Fig. 6.19 and the corresponding spectrum is shown in Fig. 6.20. The experimental spectrum is similar to the calculated spectrum shown in Fig. 6.07. A slow moving osillation with a Strouhal

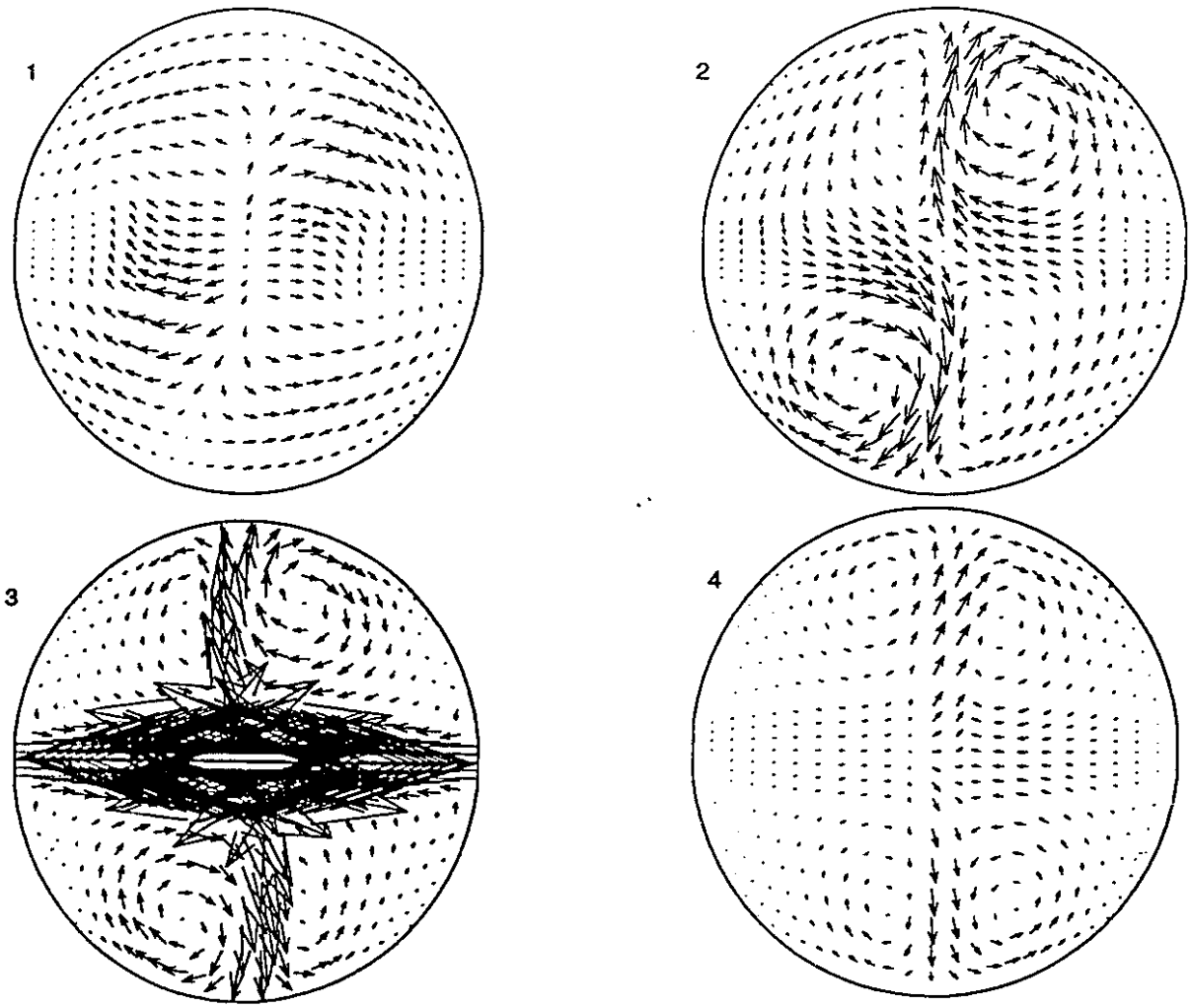

1. 0.0841D from bottom

2. 0.3250D from bottom

3. 0.5000D from bottom

4. 0.8479D from bottom

Fig.6.16: Velocity vector plots along horizontal planes, Re=125

t=116.5

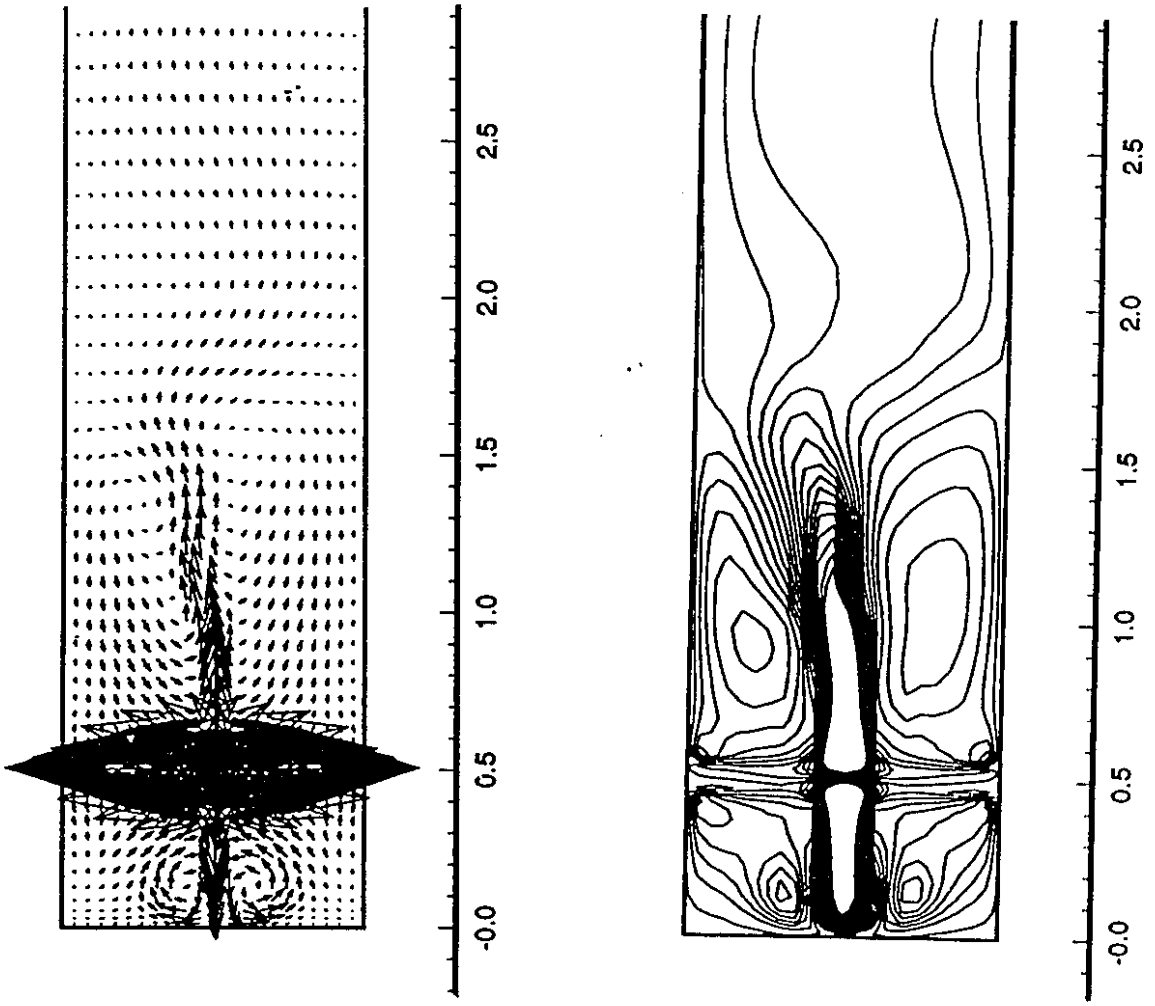

Fig. 6.17 : Velocity vector plot and u-velocity contour plot

vertical jet impingement plane, Re=125, t=116.5

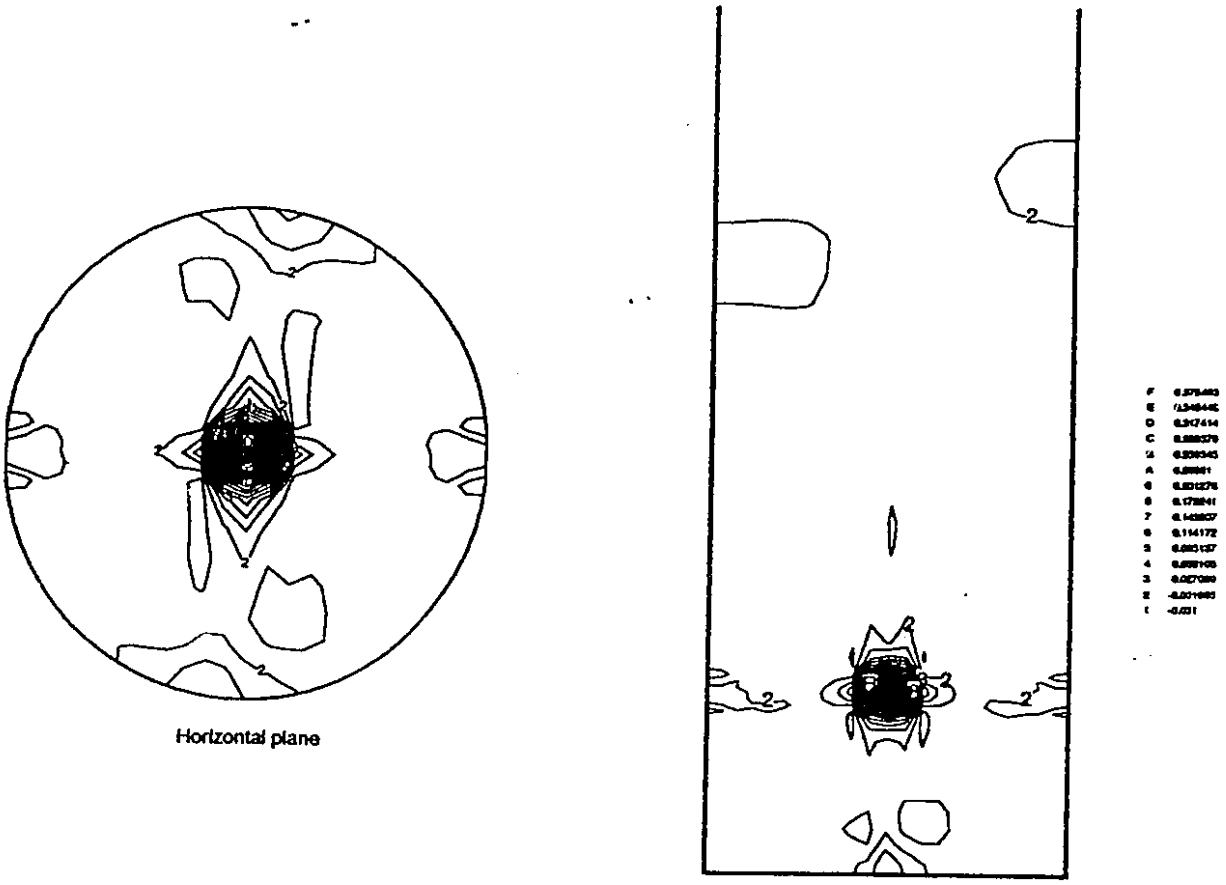

Fig. 6.18 : Pressure contour plots, horizontal and vertical jet impingement planes, Re=125, t=116.5

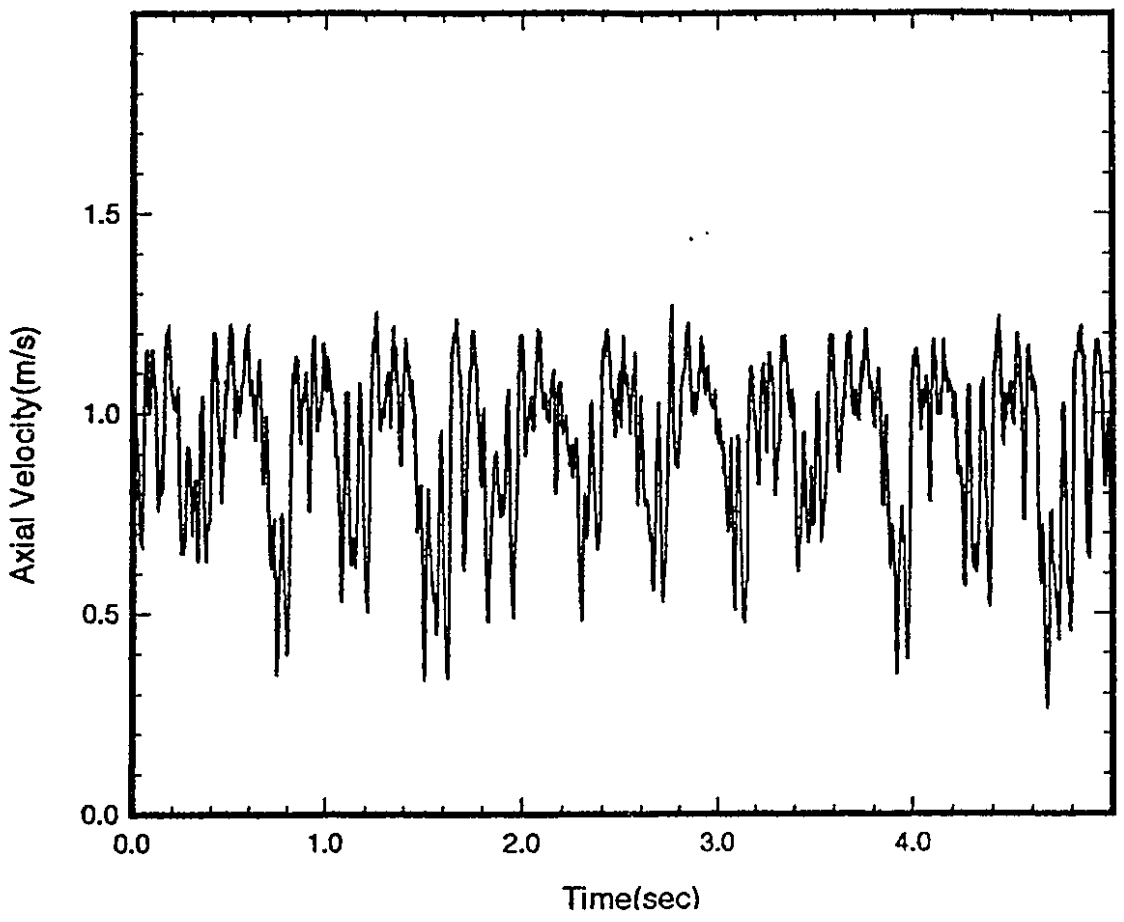

Fig.6.19 : Experimental Axial Velocity Time Series Taken at 4 jet diameters above the impingement point, Re=125

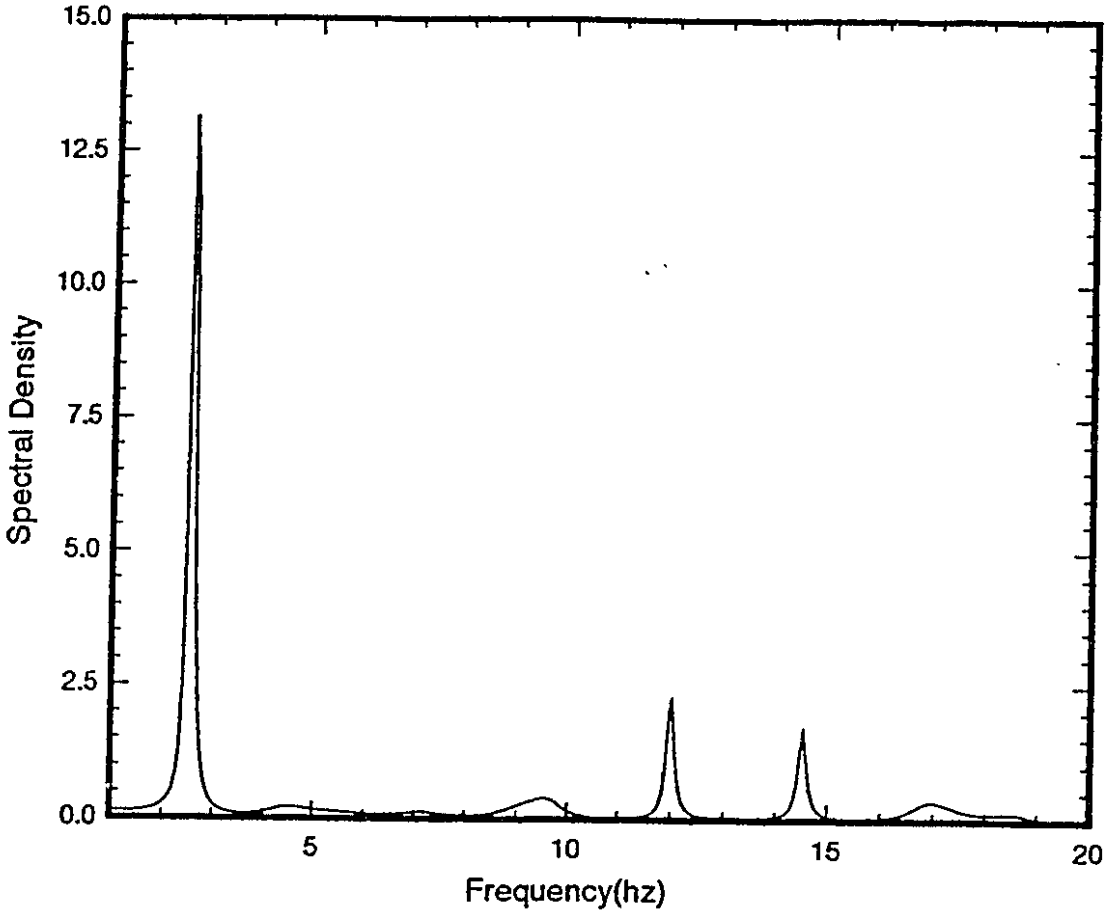

Fig.6.20: Experimental Axial Velocity Spectrum, Re=125

number of 0.0017 is present and two other frequencies with smaller amplitudes occur at a Strouhal number of 0.0083 and 0.01. The Strouhal numbers obtained from the simulated spectrum are 0.0045, 0.01 and 0.014 respectively.

7. Impingement Mixing

Since the main purpose of the opposed jet configuration in RIM is to mix pre-polymers, it is important to quantify mixing. The description of mixing involves both the fluid flow and the movement of interfaces as a function of space and time[Ottino(1989)]. The fluid velocity field can be obtained by solving the Navier-Stokes equations, and the motion of the interfaces is given by the following relationship:

$$\frac{d\vec{x}}{dt}=\vec{u} \quad . \qquad 7.01$$

where u is the solution to the Navier-Stokes equations. The solutions to the above equations seem to be simple once the fluid velocity field is known. However, the theory of dynamical systems indicates that the solution to Eq.7.01 may be complex. The work of Henon(1966) and Dombre et. al (1986) have shown that in 3-dimensional steady state flows, the particle paths may be chaotic if a hyperbolic point is present. They called this phenomenon "Lagrangian turbulence". In two-dimensional flows, chaotic particle paths may occur with time-periodic flows[Aref(1984), Khakhar et al.(1986)]. A detailed mathematical treatment of chaotic dynamical system is given in Guckenheimer and Holmes(1983).

7.1 Opposed Jet Flow as a Dynamical System

Once the velocity field is known, results from dynamical system theory can be

used to examine the nature of a system. Fixed points are defined as the points at which the velocity vanishes. Three different types of fixed points exist:

hyperbolic point - one eigenvalue of the system greater than one, other eigenvalues may be zero

elliptic point - the eigenvalues of the system are complex conjugates

parabolic point - the eigenvalues of the system are +1 or -1

In the oppsed jet flow field, the stagnation point is a fixed point since by definition velocity vanishes. Other fixed points are located within the centers of the recirculation zones. The nature of fixed points can be determined by linearizing about the fixed points[Dombre et. al(1986)]. The linearized form of Eq.7.01 near the fixed points(x_s) can be written as

$$\frac{d\vec{X}}{dt}=\nabla u_s \, \vec{X} \qquad 7.02$$

where $X=x-x_s$, ∇u_s , the velocity gradient matrix at the location x_s, is evaluated numerically using the velocity field information obtained from previous chapters and the eigenvalues of the velocity gradient matrix are calculated. At a Reynolds number of 50, the calculations show that the impingement point is hyperbolic since all three eigenvalues are real. The previous studies[Dombre et. al(1986), Aref(1984)] indicate that a region of "Lagrangian turbulence" would exist if hyperbolic fixed points exist and the flow lines connect hyperbolic points. In the opposed jet flow field the stagnation point is a hyberbolic point and the flow lines connect the hyperbolic point. These lines are called

homoclinic orbits and an infinite number of orbits can exist[Dombre et al(1986)]. The trajectories which are close together can separate exponentially in these orbits. The elliptic points and the orbits near them hinder mixing. These orbits are known as "KAM(Kolmogorov-Arnold-Moser) curves" and are invariant curves formed by quasi-periodic finite number of trajectories[Khakhar et al.(1986)]. Since particles always stay within these orbits poor mixing results

The tracking of particle paths using Eq.7.01 is difficult in chaotic systems since precision is lost at an exponential rate. Franjione and Ottino(1987) state that a numerical study of mixing through the particle paths would be nearly impossible for chaotic systems except simple two-dimensional cases.

7.2 Mixing as Stretching

Accrording to Ottino and co-workers, the essence of mixing lies in the ability of the flow to stretch and redistribute material lines and surfaces. λ is defined as the length stretch and the specific rate of stretching is given by[Ottino et al.,(1979)]

$$\frac{\lambda}{\lambda} = D : mm \qquad 7.03$$

D is the symmetric part of the velocity gradient tensor and $m = \frac{dx}{|dx|}$ is the orientation of the position vector. Since $|mm| = 1$, the Cauchy -Schwarz inequality provides,

$$D : mm \leq |D|\,|mm| = (D : D)^{1/2} \qquad 7.04$$

The specific stretch rate depends on the orientation of the fluid element and is difficult to evaluate for three-dimensional flows. One way to quantify the mixing potential of a flow field is to determine $(D:D)^{1/2}$, which is related to dissipation. Where $(D:D)^{1/2}$is higher, the flow field has a greater ability to stretch the fluid at a higher rate than when $(D:D)^{1/2}$ is low.

The $(D:D)^{1/2}$ field is determined numerically by evaluating the velocity gradient tensor using central differencing . The chain rule is used to determine the derivatives in generalized coordinates. The results are given in Fig. 7.01 for a Reynolds number 50 case with H/D=.5 , and Figs. 7.02 to Fig.7.05 for the Reynolds number of 125. Fig. 7.02 to 7 .04 are instantaneous plots of the $(D:D)^{1/2}$ field at the time steps 112.5 , 116.5 and 125.2 . Fig. 7.05 is the average $(D:D)^{1/2}$ field for 600 time steps with the time step size of 0.05. The $(D:D)^{1/2}$ field obtains the highest value at the impingement point; therefore the stretch rate is at its maximum at the impingement point. The results confirm that a hyperbolic point promotes mixing.

7.3 Approximation of Length Scales

When the jet streams mix in the mixing chamber the combination of stretching and periodic oscillations produce a mixture which contains length scales much finer than the unmixed pre-polymers. Several attempts were made to determine the length scales(striation thicknesses) of the mixture. Lee et al.(1980) used a two dimensional

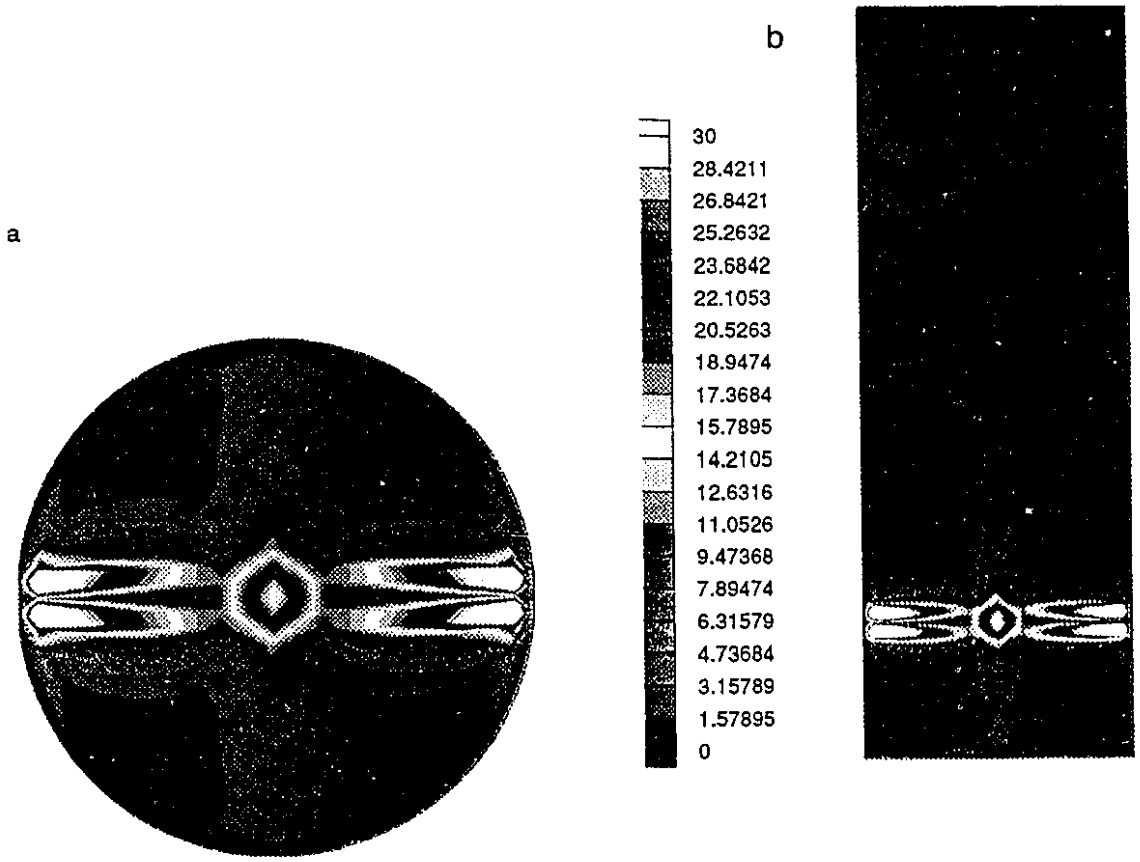

Fig.7.01: $(D:D)^{1/2}$ **Contour plots for Re=50**

a-horizontal jet impingement plane

b-vertical jet impingement plane

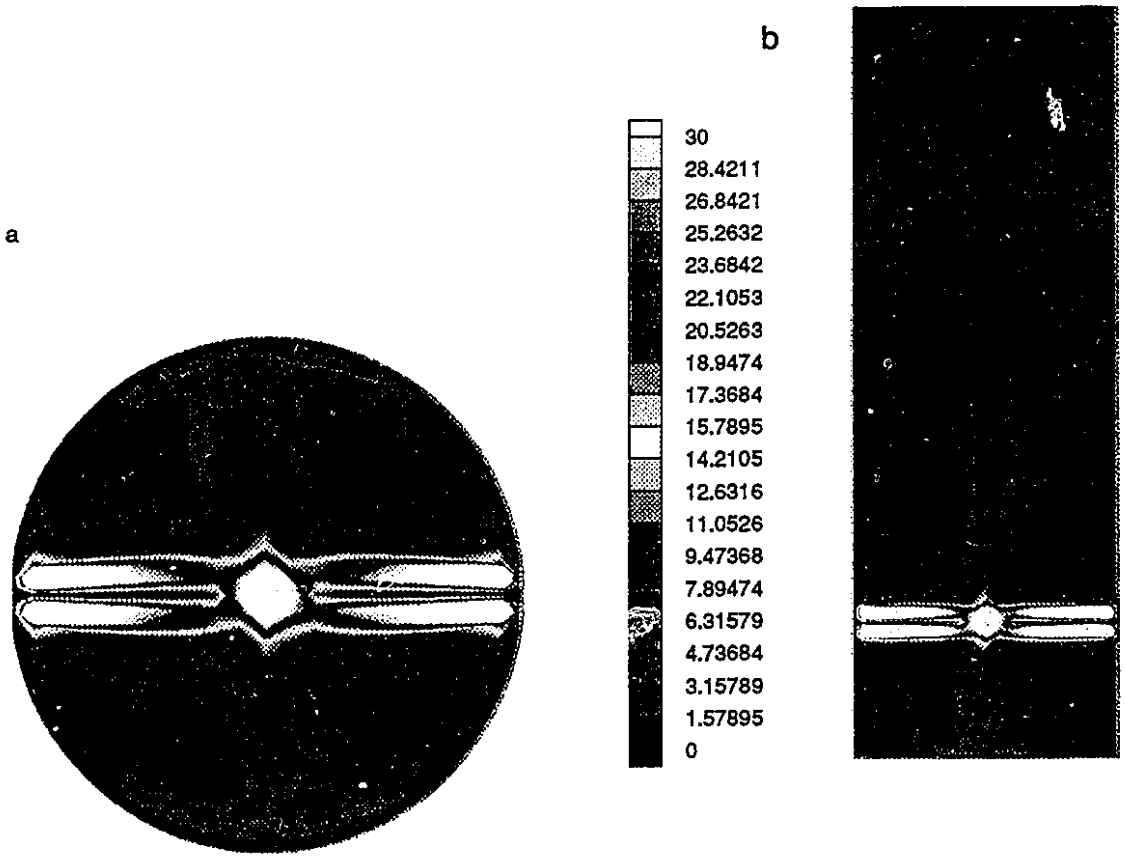

Fig.7.02: $(D:D)^{1/2}$ **Contour plots for Re=125, t=112.5**

a-horizontal jet impingement plane

b-vertical jet impingement plane

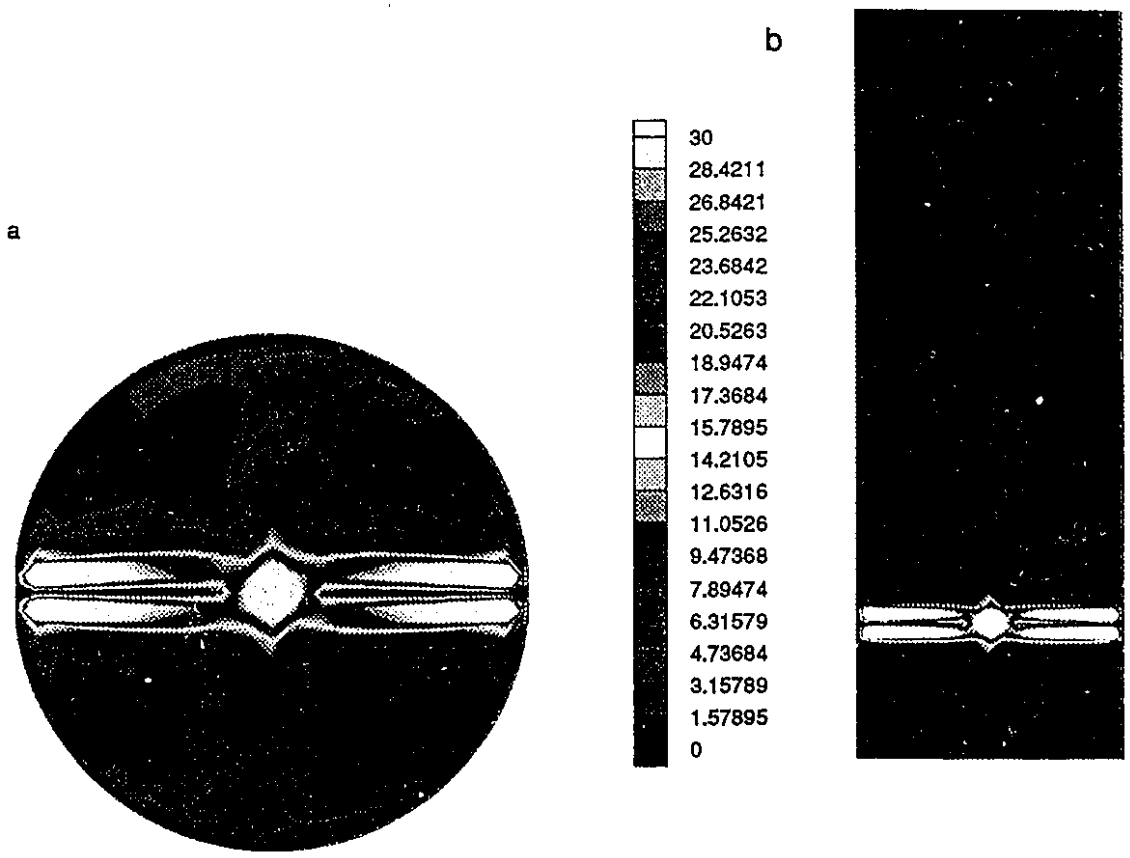

Fig.7.03: $(D:D)^{1/2}$ **Contour plots for Re=125, t=116.5**

a-horizontal jet impingement plane

b-vertical jet impingement plane

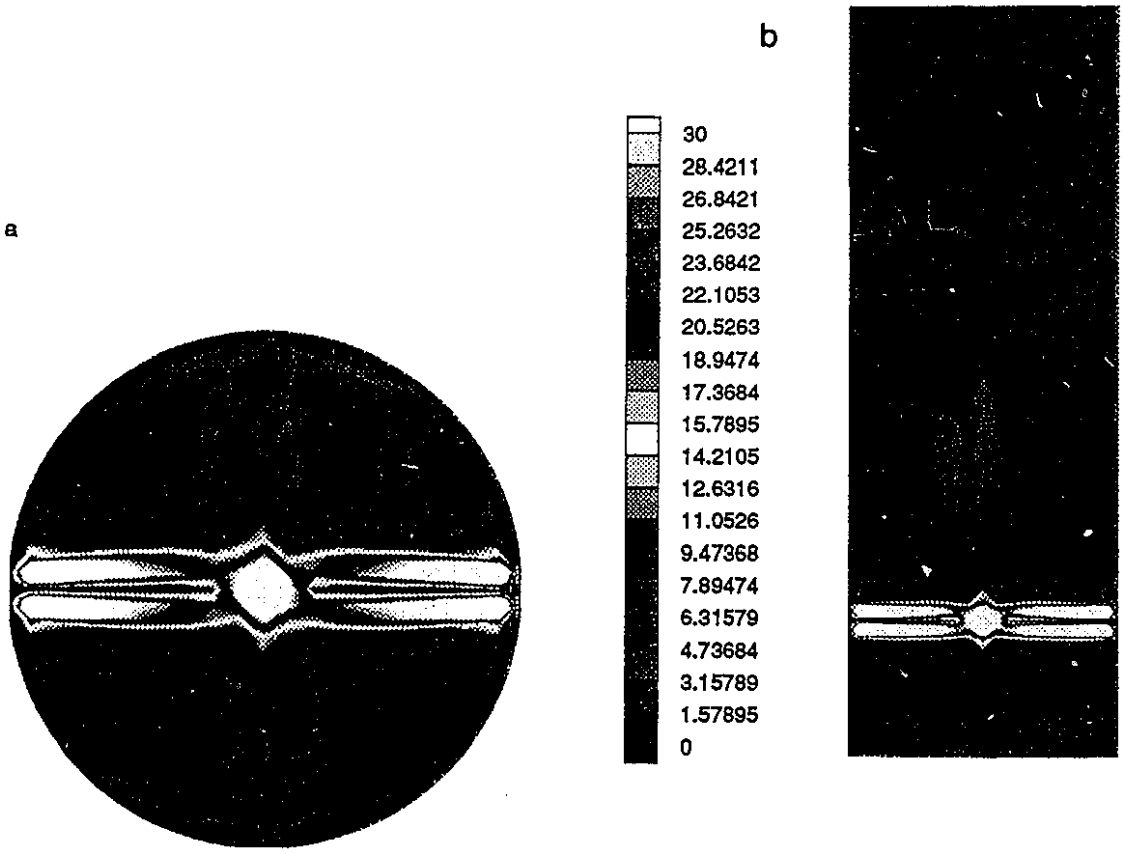

Fig.7.04: $(D:D)^{1/2}$ **Contour plots for Re=125, t=125.2**

a-horizontal jet impingement plane

b-vertical jet impingement plane

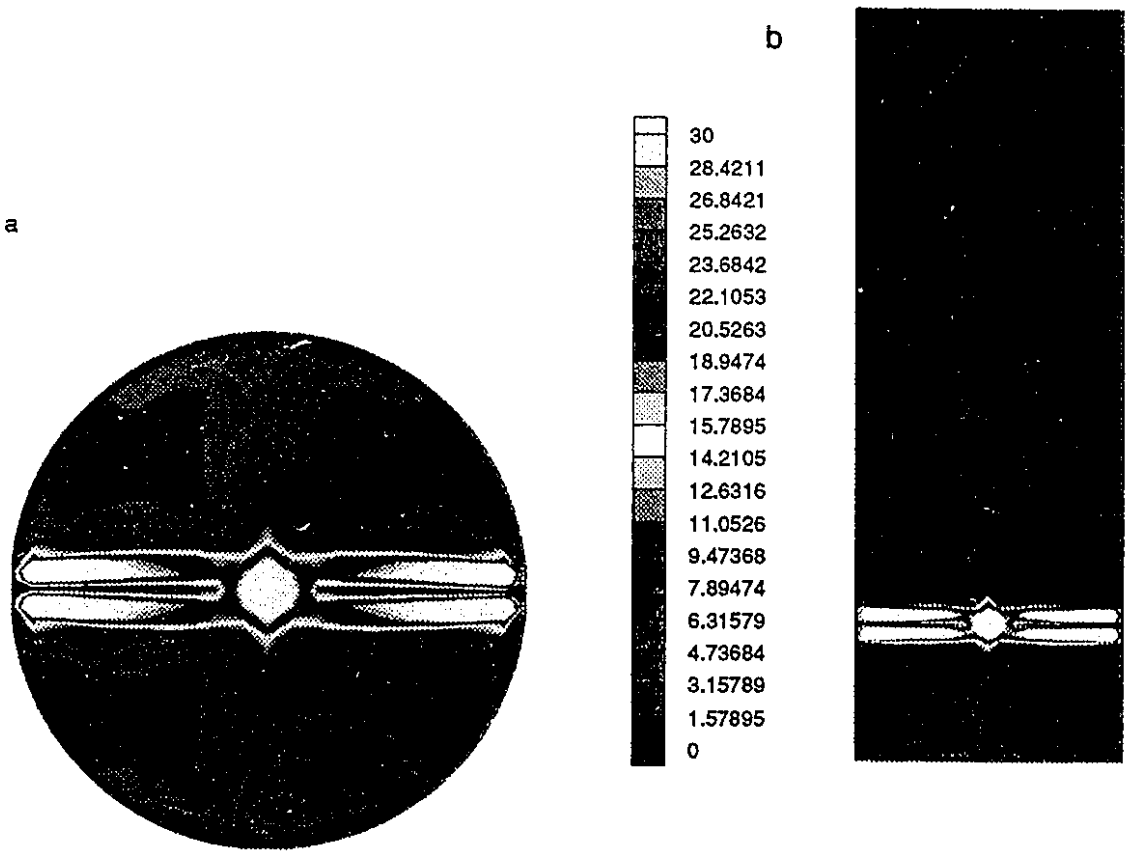

Fig.7.05: $(D:D)^{1/2}$ **Contour plots for Re=125, 600 time step average**

a-horizontal jet impingement plane

b-vertical jet impingement plane

stretching flow assumption to derive the following relationship for the mean striation thickness;

$$S_f = [\frac{2(1+1/r_s)d^5}{nD^3}]^{1/2}\frac{1}{Re^{1/2}} \qquad 7.05$$

where S_f is the striation thickness, d and D are the diameters of the feed nozzle and the mixing head respectively, n is the size of mixing zone in terms of the mixing head diameters, r_s is the ratio of the volumetric flow rates of the two streams and Re is the mixing nozzle Reynolds number.

In another formulation of striation thickness, Lee et al.(1980) used the Kolmogorov isotropic turbulence assumption first proposed by Tucker and Suh(1980) to obtain

$$S_f = (\frac{ndD^3}{1+1/r_s})^{1/4}\frac{1}{Re^{3/4}} \qquad 7.06$$

The experimental data of Kolodziej et al(1982) showed that a distribution of thicknesses exist and Baldyga and Bourne(1983) used the statistical theory of turbulence to derive a formulation for the distribution of striation thickness which matched the data of Kolodziej et al(1982) closely. The difficulty in applying the Baldyga and Bourne(1983) formulation is that the residence time distribution function is required. The residence time distribution for the RIM mixing head is not known and the assumption of perfect macro mixing used by Baldyga and Bourne(1983) is questionable since the RIM mixing head is a distributed parameter continuous flow system.

In this work a dimensional argument is used to determine the range of length scales which exist in the mixing chamber. Dissipation, ε, is defined as

$$\epsilon = 2\mu D : D \qquad 7.07$$

Dissipation can be related to the local velocity, U and length scale, l as follows

$$\epsilon \sim \nu (U/\delta)^2 \qquad 7.08$$

where ν is the kinematic viscosity. The kinematic viscosity can also be related to the local velocity and length scales

$$\nu \sim U\delta \qquad 7.09$$

The approximate length scale relationship can be obtained by combining Eq.7.08 and 7.09.

$$\delta = (\nu^3/\epsilon)^{1/4} \qquad 7.10$$

Dissipation can be easily calculated since D:D field is known. The result for the Reynolds number 125 is given in Fig. 7.06 using the time average value of dissipation for 600 time steps.

The actual length scales(δ) are normalized with respect to the chamber diameter(D). If an actual chamber diameter is 1 cm, Fig. 7.06 indicates that the smallest length scale is about 30 μm and the largest is about 300 μm. Small length scales occur

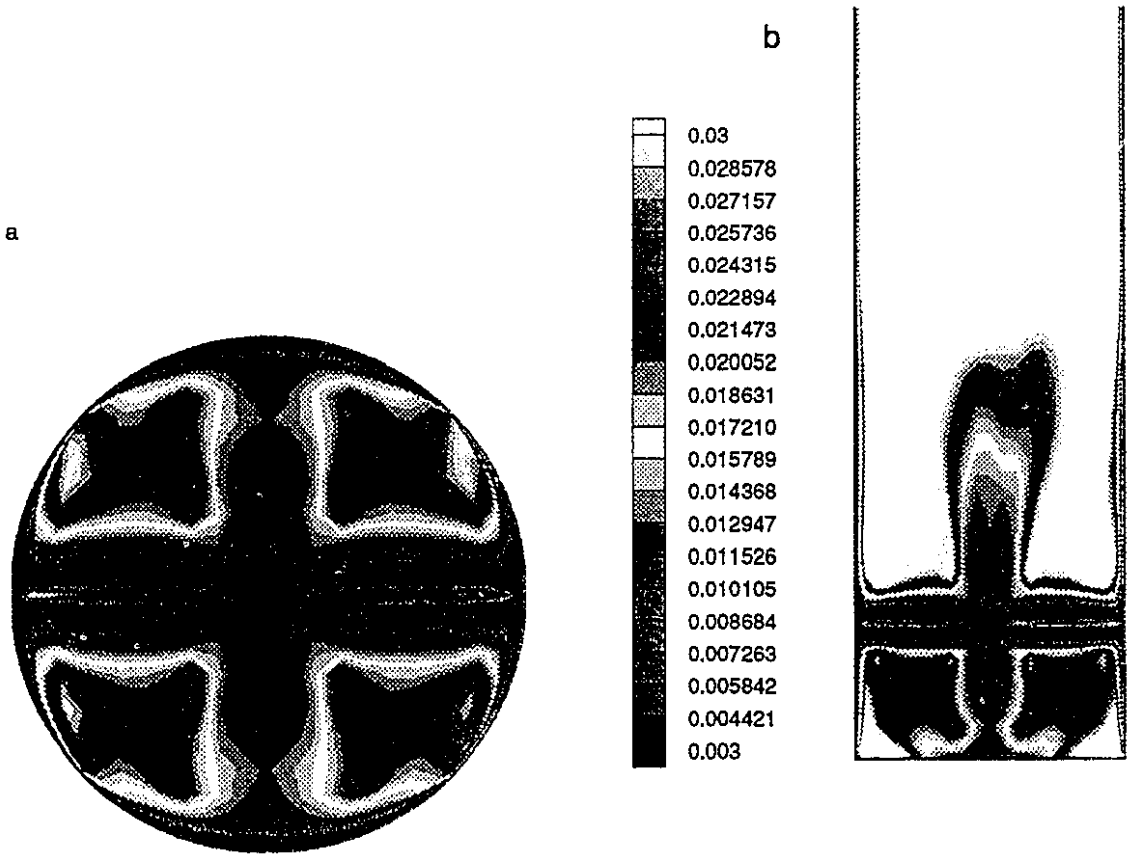

Fig.7.06: Dimensionless length scales(δ/D) in Impingement Mixer

in the region near the impingement point where dissipation is large. The model of Lee et al(1980) which assumes two dimensional stretching gives the average striation thickness of 4 μm for the Reynolds number of 125 with the assumption that mixing occurs within 2 chamber diameters. The other model of Lee et al(1980) which assumes isotropic turbulence gives the average striation thickness of 150 μm for the same Reynolds number and mixing zone length. The stretching model of Lee et al gives a result much smaller than other model indicating that the assumption of 2-dimensional stretching flow for the mixing head is not a realistic assumption. The Baldyga and Bourne(1983) model gives the equation of dimensionless thickness as a funtion of the dimensionless time, θ. For the mixing chamber with the inlet jet diameter to the chamber diamter ratio of 1 to 10, the equation for the dimensionless thickness with the assumption that mixing occurs within 2 chamber diameters is

$$\frac{\delta}{d}=0.76\,(1+21400.3\theta^2)^{-0.25} \qquad 7.11$$

d is the inlet jet diameter. The residence time distribution is required to determine the distribution of the striation thicknesses. Since an experimental residence time distribution is not available , a perfect macroscopic mixing of fluid is assumed. The resulting distribution curve is given in Fig.7.07. The thicknesses range from 25 μm to 350 μm.

7.4 Recommendations

The results of this section suggest a way to improve mixing. In the current RIM

mixhead design two jet streams are impinged head-on, creating only one hyperbolic point(Fig. 7.08a) . The previous studies have shown that a distribution of striation thickness exists and mixing is not uniform. With the aid of dynamcal theory, the reasons for inadequate mixing in RIM mixhead can be explained. The contour plots show that mixing is confined only to a region surrounding the hyperbolic points and the existence of elliptic points hinders mixing. A flow field with multiple hyperbolic points would be more effective in mixing the pre-polymers. A RIM mixhead design with four jet streams can be conceived(Fig. 7.08b). Three hyperbolic points would exit and the ability to mix would be improved significantly. A computer simulation of this flow field should be carried out and $(D:D)^{1/2}$ should be calculated.

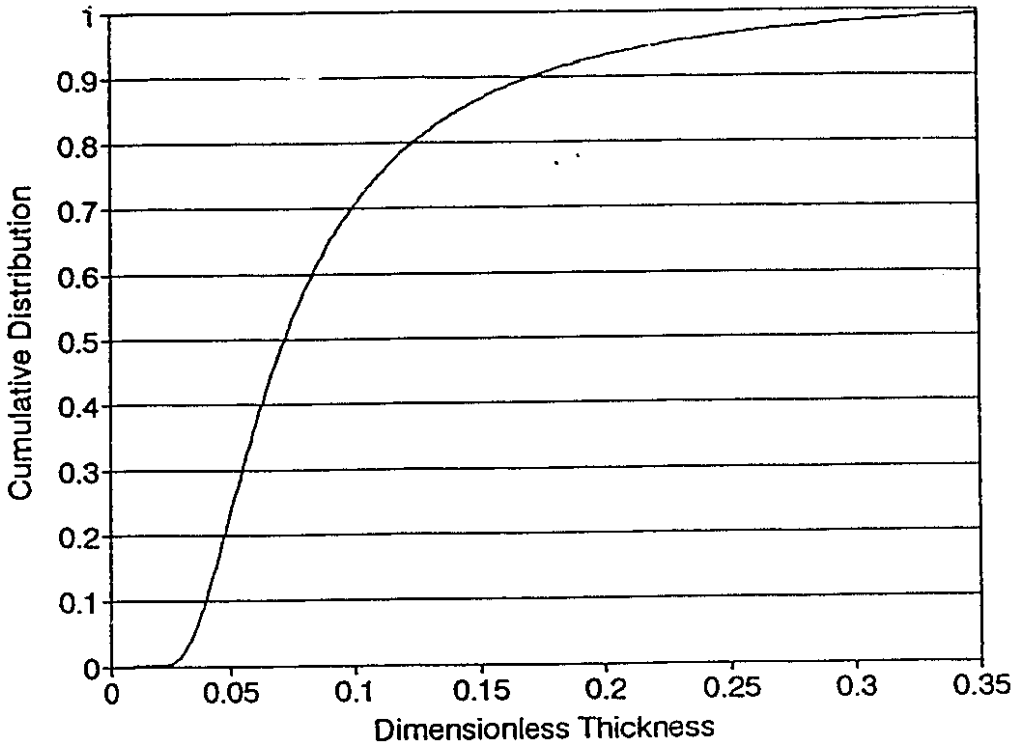

Fig. 7.07: Thickness(δ/d) distribution predicted by Baldyga and Bourne model

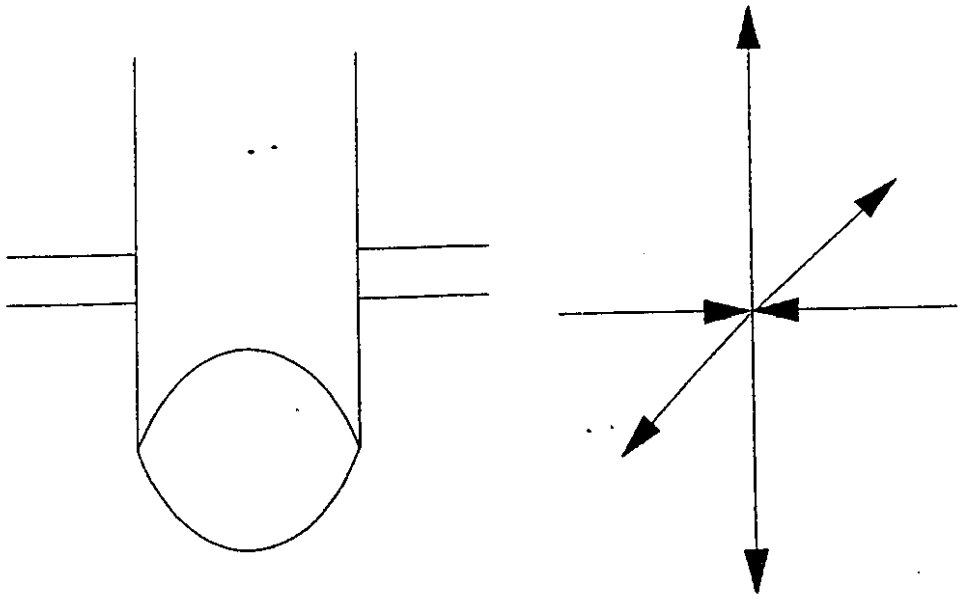

a: RIM mixhead design with one stagnation point

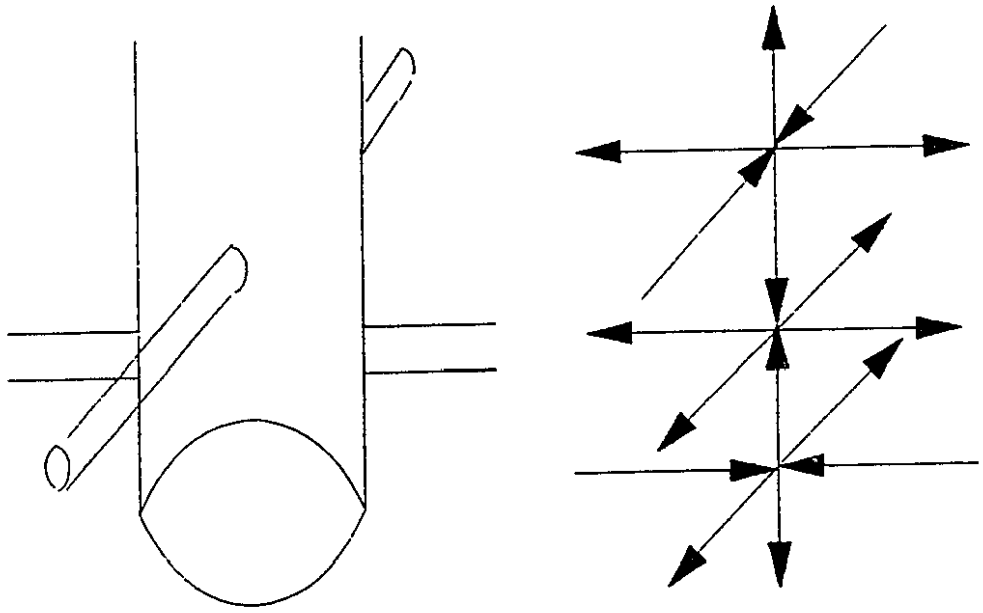

b: RIM mixhead design with multiple stagnation points

Fig. 7.08: Rim mixhead design

8. Conclusions

In this thesis the flow field created by two cylindrical laminar jets impinging head-on near the closed end of a cylidrical mixing chamber is studied numerically. This thesis is divided into two major parts. The first part is devoted to the development and testing of a numerical method powerful enough to solve the jet-to-jet impingement problem. In the second part, the method developed is used to study the steady state and unsteady state fluid flow in the mixing head and mixing and length-scales in the mixing head are also examined.

The numerical method developed consists of the discretization of the Navier-Stokes equation in generalized non-orthogonal curviliear coordinates using the finite-volume method. A stable method for discretizing the higher-order upwinding methods for the convection terms is developed. The method is tested using several two dimensional and three dimensional convection dominated flow fields with known experimental data and the numerical results agree with the experimental data closely indicating that the method is accurate.

The steady-state jet-to-jet impingement has been simulated and the quantitave and qualitative aspects of the flow field explored. Two recirculation zones form above and below the jets and the strength of the recirculation zones depend on the jet Reynolds number. The highest pressure occurs at the impingement point and the pressure at the

impingement point increases as the Reynolds number increases. The centerline axial velocity at a Reynolds number of 50 is compared with the LDA data and the two results match closely.

The unsteady state jet-to-jet impingement is explored using the time-integration. The results obtained with the grid density of 51x23x21 showed sinusoidal oscillation for the Reynolds number range of 100 to 400. A detailed study at a Reynolds number of 125 using higher grid density of 70x23x21 showed that the fluid motion is much more complicated with multiple frequencies present. The experimental LDA data confirms the results at the higher grid density. The discrepancy between the results at two different grid densities is due to the fact that at the lower grid density, the scale motion that is smaller than the grid size is not captured by the numerical method.

The mixing in the jet-to-jet flow field is examined using the dynamical system theory and evaluating the $(D:D)^{1/2}$ field. The dynamical system theory indicates that the impingement point is a hyperbolic point and may promote mixing by creating chaotic particle paths. The $(D:D)^{1/2}$ field show that the highest value occurs at the impingement point indicating that the ability to stretch the fluid element is highest at the impingement point. Length scales are determined using a dimensional argument. A range of length scale from 30 μm to 300 μm exists in a mixing head of 1 cm diameter and the jet Reynolds number of 125 and agrees closely with other correlations reported in the literature. Since hyperbolic points promote mixing, a mixing head with multiple

impingement points is proposed as an alternate design.

References

Acharya, S. and Moukalled, F. H., 'Improvements to incompressible flow calculation on a nonstaggered curvilinear grid', Numer. Heat Transfer, Part B, Vol. 15, pp. 131-152, 1989

Aref, H., 'Stirring by chaotic advection', J. Fluid Mech., Vol. 43, pp. 1-21, 1984

Aris, R., Vectors, Tensors and the Basic Equations of Fluid Mechanics , Dover Publications, 1989

Baldyga, J. and Bourne, J. R. ,'Distribution of striation thickness from impingement mixers in reaction injection molding', Polym. Eng. and Science, Vol. 23, No 10,pp 556-560, 1983

Braaten, M.E. and Shyy, W, 'Study of pressure correction methods with multigrid for viscous flow calculations in nonorthogonal curvilinear coordinates',Numer. Heat Transfer, Vol.11,pp417-442, 1987

Burggraf, O. R., 'Analytical and numerical studies of the structure of steady separated flows', J. Fluid Mech., Vol. 24, pp. 113-151, 1966

Cheng, K. C., Nakayama, J. and Akiyama, M., 'Effect of finite and infinite aspect ratios of flow patterns in curved rectangular channels', Proc. Int. Symp. on Flow Visualization, Tokyo, Japan, pp. 109-114, 1977

Davis, R. W. and Moore, E. F., 'A numerical study of vortex shedding from rectangles', J. Fluid Mech., Vol. 116, pp. 475-506, 1982

De Vahl Davis, G. and Mallison, G. D., 'An evaluation of upwind and central difference approximations by a study of recirculation flow', Computers and Fluids, Vol. 4, pp. 29-43, 1976

Dean, W. R., 'Note on the motion of fluid in a curved pipe', Philosophical Magazine, Vol. 4, pp. 208-223, 1927

Denschechikov, V. A., Kondrat'ev, V. N., Romashov, A. N. and Chubarov, V. M., 'Interaction between two opposed jets', Fluid Dyn., Vol3 ,1983 pp460-463

Dombre, T. , Frisch, U. , Greene, J. M. , Henon, M., Mehr, A. and Soward, A. M , ' Chaotic streamlines in the ABC flows', J. Fluid Mech. , Vol 167, 1986, pp353-391

Drazin, P.G. and Reid., W.H. ,_Hydrodynamic Stability_ Cambridge University Press , 1983

Fromm, J. E. and Harlow, F. H., 'Numerical solution of the problem of vortex street development', Vol. 6, Phys. Fluids, pp 975-982, 1963

Freitas, C. J. , Street, R. L., Findikakis, A. N. and Koseff, J.R , ' Numerical simulation of three-dimensional flow in a cavity', Inter. Jour. for Numerical Methods in Fluids, Vol. 5, pp561-575 ,1985

Fuchs, L. 'Computation of viscous laminar flows in cavities', Proceedings of the Fourth International Conference on Numerical Methods in Laminar and Turbulent Flow, pp468-480, 1985

Fuchs, L. and Tillmark, N. ,'Numerical and experimental study of driven flow in a polar cavity', Inter. Jour. for Numerical Methods in Fluids, Vol. 5, pp. 311-329, 1985

Gosman, A.D., Pun, W. M., Runchal, A. K., Spalding, D. B., and Wolfshtein, M. _Heat and mass transfer in recirculating flows,_ Academic , New York, 1972

Guckenheimer, J., and Holmes, P. , _Nonlinear oscillations, dynamical systems and bifurcations of vector field_, Springer-Verlag, 1983

Hama, F. R., 'Streaklines in perturbed shear flow', Phys. Fluid, Vol. 5, pp. 644-650, 1962

Han, T., Humphrey, J. A. C. and Launder, B. E., 'A comparison of hybrid and quadratic upstream differencing in high Reynolds number elliptin flow', Comput. Methods in Applied Mechanics and Engineering, Vol. 29, pp. 81-95, 1981

Huang, P. G., Launder, B. E. and Leschziner, M. A., 'discretization of nonlinear convection precesses : a broad-range comparison of four schemes', Comput. Meths. App. Mech. Engrg., Vol. 48, pp. 1-24, 1985

Humphrey, J. A. C., Taylor, A. M. K. and Whitelaw, J. H., 'Laminar flow in a square duct of strong curvature', Journal of Fluid Mechanics, Vol. 83, pp. 509-527, 1977

Jensen, K. F. , 'Micro-reaction engineering applications of reaction engineering to processing of electronic and photonic matericals', Chemical Engineering Science, Vol. 42, No. 5, pp. 923-958, 1987

Johnson, D. Personal communication, McMaster University, 1990

Joseph, D. D., 'Hydrodynamic stability and bifurcation', in _Topics in Applied Physics_ , Springer-Verlag, 1985

Joshi, D.S. and Vanka, S.P., 'Multigrid calculation procesure for internal flows in complex geometries', Numer. Heat Transfer, Part B, Vol. 20, pp61-80,1991.

Karki, K.C.,'A calculation procedure for viscous flows at all speeds in complex geometries', Ph.D. thesis, Dept of Mech. Eng., University of Minnesota, Minneapolis, 1986

Kharkar, D. V. and Ottino, J. M ,'Fluid mixing(stretching) by time-periodic sequences of weak flows', Phys. Fluids, Vol 29, pp 3503-3505

Kim, S. W. , 'A fine grid finite element computation of two-dimensional high Reynolds number flows', Computers and fluids, Vol. 16, No. 4, pp 429-444, 1988

Khosla, P. K. and Rubin, S. C., 'A diagonally dominant second-order accruate implicit scheme', comput. Fluids, Vol. 2, pp. 207-209, 1974

Kolodziej, P., Macosko, C. W. and Ranz, W. E., 'The influence of impingement mixing on striation thickness distribution and properties in fast polyurethane polymerization', Polym. Eng. Sci., Vol. 22, pp. 388-392, 1982

Lee, L. J., Ottino, J. M., Ranz, W. and Macosko, C. 'Impingement mixing in reaction injection Molding', Polym. Eng. Sci., Vol. 20, pp. 868-874, 1980

Leonard, B. P., 'A stable and accurate convective modelling procedure based on quadratic upstream interpolation method', Comput. Methods Appl. Mech. Eng., Vol. 19, pp. 59-98, 1979

Macosko, C. W. , RIM: Fundamentals of Reaction Injection Molding, Hanser, New York, 1989

Malguarnera, S. C. and suh, N. P, 'Liquid injection molding : an investigation of impingement mixing', Polym. Eng. Sci., Vol. 17, pp. 111-115, 1977

Maliska, C. R. and Raithby, G. D., 'A method for computing three dimensional flows using non-orthogonal boundary-fitted coordinate', Int. Jour. Numer. Methods in Fluids, Vol. 4, pp. 519-537, 1984

Meakin, R. L. and Street, R. L., 'Simulation of environmental flow problems in geometrically complex domains. Part 1 : A general coordinate transformation', Computer Methods in Applied Mechanics and Engineering, Vol. 68, pp. 151-175, 1988

Melaaen, M.C. ,'Calculation of fluid flows with staggered and nonstaggered curvilinear nonorthogonal grids-the theory', Numerical Heat Transfer, Part B, Vol 21, pp. 1-19, 1992

Meyer, C., Hrymak, A. and Wood, P. E., Introduction to RIM , McMaster University, 1988

Majumdar, S., 'Role of underrelaxation in momentum interpolation for calculation of flow with nonstaggered grids', Numerical Heat Transfer, Vol. 13, pp. 125-132, 1988

Nandakumar, K. and Masiliyah, J. H., 'Swirling flow and heat transfer in coiled and twisted pipes', in Advances in Transport Processes , pp. 49-112, Wiley, 1987

Nosseir, N. and Behar, S,'Characteristics of jet impingement in a side dump combustor', AIAA J. **24**, 1752-1760,1986

Ottino, J. M., The kinematics of mixing : stretching, chaos, and transport , Cambridge University Press, 1989

Patankar, S. V. and Spalding, 'A calculation procedure for heat, mass and momentum transfer in three-dimensional parabolic flows', Int. J. Heat Mass Transfer, Vol. 15, pp. 1787-1806, 1972

Patankar, S. V., 'A calculation procedure for two-dimensional elliptic situations', Numer. Heat Transfer, Vol. 4, pp. 409-425, 1981

Patankar, S. V., Numerical Heat Transfer and Fluid Flow , Hemisphere publishing company, 1982

Peric, M., 'Analysis of pressure-velocity coupling on non-orthogonal grids', Numerical Heat transfer, Part B, Vol. 17, No. 1, pp. 63-81, 1990

Peric, M., Kessler, R. and Scheuer, G., 'Comparison of finite-volume numerical method with staggered and colocated grids', Computers and Fluids, Vol. 16, No. 4, pp. 389-403, 1988

Peyret, R. and Taylor, T. D. Computational Method for Fluid FLow, Springer-Verlag, 1983

Pollard, A. and Siu, A. L. W., 'the calculation of some laminar flows using various discretization schemes', Comput. Meths. App. Mech. Engrg., Vol. 35, pp. 293-313, 1982

Press, W. H., Flannery, B. P., Teukolsky, S.A., and Vetterling, W. ,Numerical Recipes, Cambridge University Press, New York, 1989

Ramanathan, S. and Kumar, S., 'Comparison of boundary-fitted coordinates with finite-element approach for solution of conduction problems', Numr. Heat Transfer, Vol. 14, pp. 187-211, 1988

Reggio, M. and Camarero, R., 'A calculation scheme for three-dimensional viscous imcompressible flows', Journal of Fluids Engineering, Vol. 109, pp. 345-352, 1987

Reggio, M. and Camarero, R., 'Numerical solution procedure for viscous incompressible flows', Numr. Heat Transfer, Vol. 10, pp. 131-146, 1986

Rhie, C. M., 'A numerical study of the flow past an isolated airfoil with separation', Ph. D.thesis, University of Illinoise at Urbana Champaign, 1981

Rhie, C. M., 'A three-dimensional passage flow analysis method aimed at centrifugal impellers', Computers and Fluids, Vol. 3, pp. 443-460, 1985

Roache, P. J. Computational Fluid Dynamics, Hermosa Publishers, 1982

Rodi, W., Majumdar, S. and Schonung, B., 'Finite volume methods for two-dimensional incompressible flows with complex boundaries', Computer Methods in Applied Mechanics and Engineering, Vol. 75, pp. 369-392, 1989

Rosenfeld, M. , Kwak, D. and Marcel, V., 'A fractional step solution method for the unsteady incompressible Navier-Stokes equations in generalized coordinate system', Jour. Comput. Physics, Vol 94, pp 102-137 ,1991

Sandell, D. J., Experimental Methods for Studying Impingement Mixing , S. M. Thesis, University of Minnesota, 1983

Shyy, W., 'A study of finite difference approximations to steady-state, convection dominated flow problems', Journal of Computational Physics, Vol. 57, pp. 415-438, 1985

Shyy, W., Tong, S. S. and Correa, S. M., 'Numerical recirculating flow calculation using a body-fitted coordinate system', Numerical Heat Transfer, Vol. 8, pp. 99-113, 1985

Shyy, W. and Vu, T. C., 'On the adoption of velocity variable and grid system for fluid flow computation in curvilinear coordinates', Journal of Computational Physics, Vol. 92. pp. 82-105, 1991

Sobey, I. J. and Drazin, P. G., 'Bifurctation of two-dimensional channel flows', J. Fluid Mech., Vol. 171, pp. 263-287, 1980

Taylor, A. M. K. P., Whitelaw, J. H. and Yianneskis, M. J., 'Curved ducts with strong secondary motion : velocity measurements of developing laminar and turbulent flow', Journal of Fluids Engineering, Vol. 104, pp. 350-359, 1982

Taylor, C. and Hughes, T. G., Finite Element Programming of the Navier-Stokes Equations , Pineridge Press Ltd., Swansea, 1981

Thiart, G. D., 'Finite difference scheme for the numerical solution of fluid flow and heat transfer problems on nonstaggered grids', Numr. Heat Transfer, Part B., Vol. 17, pp. 43-62, 1990

Thompson, J. F., Warsi, Z. U. A. and Mastin, C. W., Numerical Grid Generation-Foundations and Applications , North-Holland, 1985

Torrance, K. E., 'Comparison of fini te-difference computations of natural convection', J. of Research of the National Bureau of Standards, Vol. 72B, No. 4, pp. 281-301, 1968

Tucker, C. L. and Suh, N. P., 'Mixing for reaction injection molding : 1. impingement mixing of liquids', Polym. Eng. Sci., Vol. 20, pp. 875-886, 1980

Vanka, S.P., Chen, C.J. and Sha, W.T.,'A semi-impilicit calculation procedure for flows described in body coordinate system', Numer. Heat Transfer, Vol. 3,pp. 99-113,1985

Vlachopoulos, J. , Mitsoulis, E., and Mirza, F.A. 'Finite-element analysis of polymeric liquid flows', Proc. 9th international congress on rheology(E. Mena et al., Eds.) Vol. 1, 655-662, Acapulco, Mexico(1984)

Wood, P., Hrymak, A., Yeo, R., Johnson, D. and Tyagi A., 'Experimental and computational studies of the fluid mechanics in an opposed jet mixing head', Phys. Fluid A, Vol. 3(5), pp. 1362-1368, May 1991

Yeo, R. W., Wood, P. E. and Hrymak, A. N., 'A numerical study of laminar 90-degree bend duct flow with different discretization schemes', Journal of Fluids Engineering, Vol. 113, pp 563-568